Lehigh University
Lehigh Preserve

Theses and Dissertations

2017

Microstructural Evolution and Mechanical Property Development of Selective Laser Melted Copper Alloys

Anthony Patrick Ventura
Lehigh University

Follow this and additional works at: http://preserve.lehigh.edu/etd

Part of the Materials Science and Engineering Commons

Recommended Citation
Ventura, Anthony Patrick, "Microstructural Evolution and Mechanical Property Development of Selective Laser Melted Copper Alloys" (2017). *Theses and Dissertations*. 2857.
http://preserve.lehigh.edu/etd/2857

This Dissertation is brought to you for free and open access by Lehigh Preserve. It has been accepted for inclusion in Theses and Dissertations by an authorized administrator of Lehigh Preserve. For more information, please contact preserve@lehigh.edu.

Microstructural Evolution and Mechanical Property Development of Selective Laser Melted Copper Alloys

by

Anthony Patrick Ventura

Presented to the Graduate and Research Committee
of Lehigh University
in Candidacy for the Degree of
Doctor of Philosophy

in

Materials Science and Engineering

Lehigh University
May 2017

© Copyright Anthony P. Ventura

May 2017

All Rights Reserved

Approved and recommended for acceptance as a dissertation in partial fulfillment of the requirements for the degree of Doctor of Philosophy.

____
Date

____
Prof. Wojciech Misiolek, Advisor

____
Accepted Date

____
Prof. Wojciech Misiolek, Chair

____
Prof. Masashi Watanabe

____
Prof. Richard Vinci

____
Dr. Gregory Pawlikowski

____
Dr. Ahmad Chamanfar

ACKNOWLEDGEMENTS

I would like to thank my advisor, Dr. Wojciech Misiolek. His insistence for graduate students to take charge of their own research allows them to find their own path to success and develop into confident engineers. He has always encouraged me to take on just a bit more responsibility than I was aware I could handle, and the trust he has placed in me has always been the catalyst for my progress. It has been a pleasure to study metallurgy under your guidance, you have been a great mentor in my life.

Two organizations have enabled me to conduct this research. I have been financially supported by the Loewy Family Foundation for many years. Mrs. Linz and the foundation have shaped my career, and their stewardship of research and education has left a lasting impression on me. TE Connectivity has funded a significant portion of this research. Greg Pawlikowski and Martin Bayes have always been supportive of my research efforts and this work would not have been possible without them.

To all members of the Materials Science & Engineering Department family and the Loewy Institute, thank you for your support. The fellowship of graduate students, past and present, that I have learned alongside; you have all been wonderful colleagues and friends. Special thanks go to Mike Rex, Arlan Benscoter, Lisa Arechiga, and Katrina Kraft for tolerating all of us in our time at Lehigh.

To my friends, Marc, Andrew, Amelia, Matt, Rosey and many others: thank you for helping bring balance to my life and all the fun times we have together. Mario Epler, thank you for your friendship and guidance at many LVASM meetings.

I am grateful to all my professors at Lehigh University, and especially those that are serving on my doctoral committee: Dr. Masashi Watanabe and Dr. Richard Vinci. They have been overwhelmingly helpful and positive in every regard. I could not possibly ask for better guidance in my academic life.

Very special thanks go to Janie Carlin and Rus Van Westervelt. Janie's warm smile and welcome conversation made every day in Whitaker brighter; I can't imagine my time at Lehigh without her. Rus Van Westervelt, thank you for encouraging me to live deliberately, and learn all that life has to teach. You have both had a positive impact on every aspect of my life.

Without the love and support of my family, I would not have made it here today. To my mom, dad, and older brother: thank you for raising me and always being there for me, even in times when I was miserable company. You have helped me every step of the way and I love you. To the Couillards, I could not have imagined a more loving family to become a part of.

Finally, I must thank my wonderful wife, Beth. She never fails to be my better half. I love you, and our life together will always be the most important thing to me.

For my grandfather

Hector C. Ventura

Thank you for the compliment

TABLE OF CONTENTS

ACKNOWLEDGEMENTS iv
TABLE OF CONTENTS vii
LIST OF TABLES x
LIST OF FIGURES xi
ABSTRACT 1
CHAPTER 1
INTRODUCTION 3
1.1 Additive Manufacturing 3
1.2 Metal AM Technologies 6
1.3 Motivation and Research Objective 10
1.4 Dissertation Structure 12
CHAPTER 2
BACKGROUND 13
2.1 Description of the Selective Laser Melting Process 13
2.2 Characteristics of Metal Alloys Fabricated via SLM 17
2.3 The Physical Metallurgy of Copper Alloys 26
2.3.1 Overview of Copper Alloys 26
2.3.2 Introduction to the Conductivity of Copper Alloys 28
2.3.3 Principle Strengthening Mechanisms of Copper Alloys 29
2.3.3.1 Work (Strain) Hardening 29
2.3.3.2 Hall-Petch Strengthening (Grain Boundary Strengthening) 33
2.3.3.3 Solid Solution Strengthening 36
2.3.3.4 Precipitation Hardening (Strengthening) 41
2.3.3.5 Dispersion Strengthening 47
2.3.4 The Cu-Sn System 49
2.3.5 The Cu-Ni-Si System 53
CHAPTER 3
MECHANICAL PROPERTIES AND MICROSTRUCTURAL CHARACTERIZATION OF Cu-4.3%Sn FABRICATED BY SELECTIVE LASER MELTING 64
3.1 Abstract 64
3.2 Introduction 64

3.3 Experimental Methods ... 67
3.4 Results ... 70
3.5 Discussion ... 77
3.5.1 Grain Morphology ... 77
3.5.2 Effect of Geometry on Tensile Properties ... 79
3.5.3 Effect of Heat Treatment on Tensile Properties ... 82
3.5.4 High Magnification STEM and EDS ... 86
3.6 Conclusions ... 93
3.7 Acknowledgements ... 94
CHAPTER 4
THE EFFECT OF AGING ON THE MICROSTRUCTURE OF SELECTIVE LASER MELTED Cu-Ni-Si ... 96
4.1 Abstract ... 96
4.2 Introduction ... 97
4.3 Experimental Methods ... 99
4.4 Results ... 103
4.5 Discussion ... 111
4.5.1 As-Printed Microstructural Features ... 111
4.5.2 Aging and Precipitation Contributions to Strengthening ... 117
4.5.3 Other Contributions to Mechanical Property Development ... 125
4.6 Conclusions ... 131
4.7 Acknowledgements ... 132
CHAPTER 5
SUMMARY ... 133
5.1 Significance of Findings ... 133
5.2 Future Work ... 134
5.2.1 Fabrication Parameters ... 134
5.2.2 Post-Processing and Other Mechanical Property Metrics ... 135
5.2.3 Copper Alloy Development For SLM ... 137
REFERENCES ... 139
APPENDIX A
EXPANDED METHODS ... 147
A.1 Expanded Methods Introduction ... 147

A.2 SLM Process Parameters 148
A.3 Heat Treatment 149
A.4 Tensile Testing 155
A.5 Metallographic Preparation 158
A.6 Microhardness 165
A.7 Standard Operating Procedure for Phase ID by XRD 166
A.8 Electron Backscatter Diffraction 169
A.9 Focused Ion Beam Milling and TEM Sample Preparation 171
A.10 Transmission Electron Microscopy 174
VITA 175

LIST OF TABLES

Table 1. UNS C70250 alloy composition specifications.[67]........................... 53

Table 2. Physical Properties of SLM Cu-4.3%Sn in the As-Printed and Post-Process Heat Treated Conditions 73

Table 3. C70250 powder composition from ECKA Granules specifications. 100

LIST OF FIGURES

Figure 1. Schematic diagram of the SLM process.[19] 14

Figure 2. Effective absorptance of a deep powder bed vs dense material absorptance for various pure metals. Symbols are experimental data and lines are models.[20] 16

Figure 3. Change in solidification substructure moving away from the weld line in SLM AlSi10Mg.The build direction is vertical. [24] 20

Figure 4. Variation in solidification substructure under different G and R conditions.[33] 21

Figure 5. Epitaxial growth observed in the weld pools of SLM AlSi10Mg.[24] 23

Figure 6. Conductivity vs. ultimate tensile strength for various annealed copper alloys. [16] 28

Figure 7. Work hardening rate (Θ) versus stress (σ) for different strain rates (a and b) with the Voce parameters specified on the axes.[47] 32

Figure 8. Approximate effect of solute content on the critical resolved shear stress at room temperature.[16] 38

Figure 9. The effect of small additions of solute atoms on the resistivity of copper.[58] 40

Figure 10. Schematic diagram of the major strengthening mechanisms active during a precipitation hardening aging heat treatment.[45] 43

Figure 11. Copper-Tin equilibrium phase diagram. [16] 52

Figure 12. Dark-field micrograph of a CuNiSi alloy aged at 450°C for 750 hours with the beam direction parallel to the <001> of the copper matrix using the $(020)_{ppt}$ diffraction spot for imaging.[68] 55

Figure 13. (a) Simulations of the 6 δ-Ni_2Si diffraction patterns that are present when viewing along the $<111>_{Cu}$ (b) the copper and δ-Ni_2Si patterns superimposed and (c) secondary diffraction effects added to (b) next to (d) an experimental pattern.[70] 57

Figure 14. Variation in precipitate thickness (▪) and diameter (▫) during aging at 450°C for CuNiSi.[68] 58

Figure 15. Schematic free energy curve at sub-critical aging temperatures for CuNiSi alloys proposed by Zhao et al. [73] 61

Figure 16. Prototypical uniaxial tensile test results of SLM Cu-4.3%Sn in the as-printed condition as well as post-process heat treated at 873 K (600 °C) and 1173 K (900 °C). 71

Figure 17. Light optical micrograph of the build direction of as-printed Cu-4.3%Sn etched in Klemm's I reagent. 74
Figure 18. IPF Maps of SLM Cu-4.3%Sn in the (a) as-printed condition, and after heat treatment at (b) 873 K (600 °C) and (c) 1173 K (900 °C). 75
Figure 19. ABF STEM microstructural comparison between SLM Cu4.3%Sn in the (a) as-printed condition as well as printed and heat treated at (b) 873 K (600 °C) and (c) 1173 K (900 °C). 76
Figure 20. Inverse pole figures taken from the transverse direction (parallel to the build direction) of SLM Cu-4.3%Sn in the (a) as-printed condition as well as heat treatment at (b) 873 K (600 °C) and (c) 1173 K (900 °C). 79
Figure 21. Prototypical uniaxial tensile test results of SLM Cu-4.3%Sn in the as-printed condition 3mm thick, 1mm thick and a sample that was machined from a rectangular prism to 3mm thick. 80
Figure 22. Differential interference contrast light optical micrograph of the build direction of SLM Cu-4.3%Sn heat treated at 873 K (600 °C) etched in Klemm's I reagent. 85
Figure 23. ABF STEM image along the build direction of as-printed SLM Cu-4.3%Sn showing an individual weld line (dashed line) and solidification sub-structure.......... 87
Figure 24. BF- STEM and accompanying XEDS intensity maps of typical small particles observed in the intercellular regions of the as-printed Cu-4.3%Sn. 88
Figure 25. XRD pattern obtained from as printed SLM Cu-4.3%Sn. 89
Figure 26. ABF-STEM image of oxide particles (dark spots) observed in SLM Cu-4.3%Sn heat treated at 873 K (600 °C). 91
Figure 27. BF-STEM image of oxide particles observed in SLM Cu-4.3%Sn heat treated at 1173 K (900 °C). 92
Figure 28. Physical property evolution of SLM C70250 during aging at 723 K (450 °C) from the as-printed condition. 105
Figure 29. Polarized light optical micrographs of as-printed SLM C70250 in the (a) build direction and (b) transverse direction. 106
Figure 30. Bright-field TEM micrograph of dislocations in the solidification substructure at the melt pool boundary in as-printed SLM C70250. 107
Figure 31. XRD patterns of SLM C70250 at various stages of aging. 108

Figure 32. (a) Dark-field TEM micrograph of the δ-Ni_2Si strengthening precipitates in the peak age condition and (b) the corresponding SAD pattern of the $[111]_{Cu}$ matrix projection. 110
Figure 33. (a) Dark-field TEM micrograph of the δ-Ni_2Si strengthening precipitates in the over age condition and (b) the corresponding SAD pattern of the $[111]_{Cu}$ matrix projection. 110
Figure 34. Bright-field LOM micrograph of as-printed SLM C70250 showing the change in solidification substructure scale throughout the weld pools. Dashed lines mark the fusion line of two melt pools. 114
Figure 35. Bright-field STEM and XEDS intensity maps (normalized to the Cu intensity) of the solidification substructure at the weld line in as-printed SLM C70250. 115
Figure 36. Microhardness and electrical conductivity comparison between SLM C70250 aged directly after printing (P+A) and samples that had an intermediate homogenization/solution heat treatment (P+ST+A). 119
Figure 37. (a) Secondary electron micrograph of a DP zone in over aged SLM C70250 (aged for 128 hours). (b) Bright-field TEM micrograph of a precipitate in the DP zone, (c) accompanying SAD pattern along the $[110]_{Cu} \| [010]_{\delta}$ and (d) the corresponding simulated diffraction pattern. 121
Figure 38. Work hardening rate versus the normalized flow stress for SLM C70250 at various stages of aging. 128
Figure 39. (a) LOM observation and (b) EBSD analysis of deformation twinning observed in a peak aged SLM C70250 sample deformed in a uniaxial tensile test to failure. The black lines in (b) outline FCC twin boundaries. 129
Figure 40. Density vs linear laser energy curve at various beam spot sizes. This data was utilized to select the ideal processing parameters for samples used in this study. 149
Figure 41. Temperature vs time plot showing the maximum ramp rate of the tube furnace used in this investigation during cross flow of argon gas. 152
Figure 42. Oxygen incorporation near the surface of copper samples heat treated at 900°C in a tube furnace with an additional leak from thermocouple wire insertion. 154
Figure 43. Micrograph of a copper sample heat treated in a furnace without a thermocouple wire inserted, no significant oxide formation is present. 154

Figure 44. The two types of speckle patterns used for DIC strain mapping for (top) as-printed samples and (bottom) machined samples. 157

Figure 45. Comparison of LOM contrast after etching with Klemm's I for 2 minutes 15 seconds in (top) bright-field and (bottom) cross-polarized light. Alloy C70250, build direction, as-printed condition. 163

Figure 46. LOM micrograph of contrast after etching with ferric nitrate solution. Alloy C70250, peak age, strained to failure to show twinning. 164

Figure 47. Comparison of microhardness measurements taken with different indentation loads. Alloy C70250, solution treated and aged. 166

Figure 48. IPF map obtained from EBSD showing scratches and drifting. Image quality is overlaid in greyscale. Alloy C70250, as-printed. 170

Figure 49. Examples of FIB damage observed during Ga ion milling of copper. Damaged regions were exposed to (a) 30 keV 50 pA Ga ions and (b) 5keV 100 pA Ga ions.[105] 172

Figure 50. Example TEM micrograph showing FIB damage observed in this research. Alloy C70250, over aged. 173

ABSTRACT

Selective Laser Melting (SLM) is an additive manufacturing technology that utilizes a high-power laser to melt metal powder and form a part layer-by-layer. Over the last 25 years, the technology has progressed from prototyping polymer parts to full scale production of metal component. SLM offers several advantages over traditional manufacturing techniques; however, the current alloy systems that are researched and utilized for SLM do not address applications requiring high electrical and thermal conductivity. This work presents a characterization of the microstructural evolution and mechanical property development of two copper alloys fabricated via SLM and post-process heat treated to address this gap in knowledge. Tensile testing, conductivity measurement, and detailed microstructural characterization was carried out on samples in the as-printed and heat treated conditions.

A single phase solid solution strengthened binary alloy, Cu-4.3Sn, was the first alloy studied. Components were selectively laser melted from pre-alloyed Cu-4.3Sn powder and heat treated at 873 K (600 °C) and 1173 K (900 °C) for 1 hour. As-printed samples were around 97 percent dense with a yield strength of 274 MPa, an electrical conductivity of 24.1 %IACS, and an elongation of 5.6%. Heat treatment resulted in lower yield strength with significant increases in ductility due to recrystallization and a decrease in dislocation density. Tensile sample geometry and surface finish also showed a significant effect on measured yield strength but a negligible change in

measured ductility. Microstructural characterization indicated that grains primarily grow epitaxially with a sub-micron cellular solidification sub-structure. Nanometer scale tin dioxide particles identified via XRD were found throughout the structure in the tin-rich intercellular regions.

The second alloy studied was a high-performance precipitation hardening Cu-Ni-Si alloy, C70250. Pre-alloyed powder was selectively laser melted to produce components around 98 percent dense with high mechanical strength and electrical conductivity. Aging heat treatments were carried out at 723 K (450 °C) directly on as-printed samples up to 128 hours. A peak yield strength of around 590 MPa could be attained with an electrical conductivity of 34.2 %IACS after 8 hours of aging. Conductivity continues to increase with further aging while the peak strength appears to be less sensitive to aging time exhibiting a broad range of time where near-peak properties exist. Nanometer-scale silicon-rich oxide particles exist throughout the material and persist during aging. Deformation twinning is observed in the peak age condition after tensile testing and several strengthening mechanisms appear to be active to varying degrees throughout aging, which accounts for the broad range of aging time where nearly the peak mechanical properties exist. The findings of this research are integral to understanding SLM copper alloys and serve as a foundation for future development of new copper alloys tailored to the SLM process.

CHAPTER 1

INTRODUCTION

1.1 Additive Manufacturing

Additive manufacturing (AM) refers to a group of technologies that build up a shape layer-by-layer from a three-dimensional computer model. Although the origins of the concept were being explored in the 1950s and 1960s, the first widely used AM technology, stereolithography, was developed by Charles Hull in 1984 to produce polymer prototypes and streamline the design process. Hull described the process as "A system for generating three-dimensional objects by creating a cross-sectional pattern of the object to be… automatically formed and integrated together to provide a step-wise laminar buildup of the desired object".[1] The fundamental principles Hull outlines are present in all modern variations of AM technology. Parts are created from computer aided design (CAD) files that have been "sliced" into individual build layers. Each layer is successively fabricated on top of the previous layer until the part is finished.

The concept of building a part layer-by-layer contrasts with traditional subtractive processes such as machining or multi-step forming processes and fundamentally shapes the design methodology of AM. Originally, AM technologies were primarily used for prototyping and design purposes explicitly (hence the initial nomenclature of "Rapid Prototyping"). As developments are continually made, AM has increasingly been discussed as a

potential paradigm shift in manufacturing where, extrapolated to the extreme, direct digital manufacturing of customized parts on an as-needed basis is standard practice.[2] In their current form, the various AM technologies serve as powerful prototyping and design tools building upon their original intent with a growing set of applications for manufacturing finished parts. The current state-of-the-art AM technologies produce components of high enough quality to be utilized as finished products and research continues to address the need for improvements in AM part quality.

AM has several advantages over traditional manufacturing techniques. Although there are more intricate sets of advantages and disadvantages for each individual technology, there are many benefits that apply generally to AM as compared to traditional manufacturing. One of the most fundamental and unique advantages is the concept that adding complexity to a component (primarily in the form of more intricate geometries) does not pose a significant challenge or increase in resources. CAD is integral to the design process in modern manufacturing. In AM, the move from CAD to fabrication is essentially seamless. Therefore, a great deal of freedom is introduced to the design process because the capabilities of traditional manufacturing techniques no longer require consideration (i.e. features that are difficult to produce or add prohibitive cost in traditional manufacturing can be included where they are the optimum solution). This results in the ability to create customized components, easily change designs on a short time scale with no additional cost, and

streamline the overall design process.[2] “Free complexity” is also the root cause of the low material waste and reduction in number of processing steps required to make a finished component in AM. In nearly all AM technologies, excess material that is not directly utilized to fabricate the component can be recycled. As a result, AM does not waste a significant amount of raw material and falls under the categorization of a near-net shape process.[3] All features of the finished component are formed during a single-step process which eliminates processing steps. The more complex a part is, the more significant these advantages can become. As a result, AM is a particularly attractive option for biomedical and aerospace industries where increased complexity can have significant effects on performance.[4]

AM struggles to compete with traditional manufacturing techniques due to several key disadvantages. One issue is the cost and low production rate for large quantities of components. Although the batch nature of AM technologies allows for some degree of flexibility, the process generally has poor economies of scale and does not become significantly more cost effective for large production runs of the same component. Additionally, there is a fixed amount of set up before each production batch, so producing more parts does not result in increased production efficiency.[5] Another significant disadvantage of AM is the low mechanical performance compared to traditionally manufactured materials. There are often imperfections such as porosity, surface roughness, and contamination which degrade the bulk

physical properties of the material.[2] Increasing the reliability and diversity of all types of materials fabricated by AM is one of the current primary research objectives in the field.

1.2 Metal AM Technologies

Polymers were traditionally the materials of choice for AM due to their ease of processing, particularly in the common commercial technology stereolithography where photopolymerization is the mechanism for fabrication. However, as the field progressed, several technologies were developed that could process metal alloys. The ability to process metals drastically expanded the attainable properties and applications of AM.[2] The most common AM technologies that are applicable to metal systems can be divided broadly into binder jetting, direct energy deposition (beam deposition) and powder bed fusion. Note that although other technologies exist for metal AM, only the most prolific methods are briefly introduced here.

Binder jetting is closely related conceptually to the established powder metallurgy process of metal injection molding that employs a polymer binder and metal powder to eventually produce a metal part.[6] A print head sprays a polymer binder into a powder bed in a layer-by-layer fashion. The part that emerges is known as a “green body” as the metal powder is primarily held together by the binder phase and has not been fully densified. Extensive post processing is required to remove the binding phase and produce high density metal component. The post processing consists of either a traditional furnace

sintering (sometimes hot isostatic pressing is employed where high pressure aids in consolidation) or infiltration with a lower melting temperature alloy. Sintering involves a substantial amount of shrinkage and distortion that must be designed for which in practice is quite difficult given the low initial density of the green body. In the case of infiltration, the component is typically composed of 60% of the build powder and 35% of the infiltrant (the remaining 5% is indicative of typically porosity levels) so the attainable properties are limited substantially by the infiltrant (the most common implementation of this technique is bronze used to infiltrate stainless steel parts). The extensive amount of post-processing distinguishes binder jetting as an indirect metal AM technology and the potential for novel implementations limited compared to direct energy deposition and powder bed fusion which can directly produce high density metal components.[2,7]

Direct energy deposition (DED) is in many ways similar to established welding technology but is distinguishable by CAD input data and machines designed to create complex 3D shapes. In DED a focused beam of energy, for example an arc, electron beam, or laser, is used to melt feed material that is directly laid onto the fabrication bed/part. The most common feed material is metal powder because it allows for greater geometrical control, however wire fed systems also exist with higher deposition rates at the expense of feature resolution. Fully dense metal components can be produced via this technique, and functionally graded material composition is possible. However, the feature

resolution and surface finish of DED processes is poor and in order to achieve better accuracies the deposition rate must be decreased to low levels. Additionally the geometrical complexity in DED is limited due to the lack of a support structure which limits the types of fully functional parts the technology can produce. Nevertheless, the precise composition control and ease of implementation is a substantial benefit of DED technologies. The processes see limited use for fully finished components, but they are well established for use in coatings, repair, and feature addition when combined with CNC machining.[2,7]

Powder bed fusion (PBF) technologies are currently the AM technology of choice for fabrication of high density, geometrically complex, and fully functional metal components. The process is schematically similar to binder jetting in that the raw material is supplied in the form of a bed of powder metal. The key difference is the implementation of a high-energy beam to fully melt the powder bed rather than a jet of polymer binder that requires post-fabrication densification. The resulting parts are fully functional, high density components that can be implemented directly after fabrication. There are two primary forms of PBF for metals; electron beam melting (EBM) that, as the name implies, utilizes an electron beam to melt the powder and Selective Laser Melting (SLM) which utilizes a laser as the energy source. An introduction to the main differences between the two technologies is presented

here, but a detailed description of the SLM process, the primary focus of this work, is presented in Chapter 2.

The two main types of PBF in the form of EBM and SLM are very similar, but EBM has several characteristics that are disadvantageous from a commercial standpoint. Electrons used to heat the powder bed must be carried away from the initial focal point, so EBM processing is limited by the conductivity of the build material. The process therefore works almost exclusively on metals, which are good conductors, and there are some processing limitations on relatively low conductivity alloys (e.g. steels). The use of an electron beam also necessitates a vacuum to operate which increases machine cost and maintenance. The recyclability of powder metal feed stock in EBM can also be an issue. The powder bed is maintained at a higher temperature during fabrication compared to SLM due to the nature of heating with an electron beam. The beam is typically used to broadly heat the powder bed and minimize the necessity for high electron beam density which causes a highly localized negative charge. The negative charge can repel the incoming electron beam or cause neighboring powder particles to repel each other; both of these phenomena cause significant build defects and can cause a build to fail. However, the high powder bed temperature typically leads to some degree of solid state sintering in the lower powder layers during fabrication. A significant amount of agglomeration can then occur which affects the flow characteristics of the powder and limits the number of runs a

particular batch of powder may be used. This also results in a poor surface finish and feature resolution compared to SLM. Although EBM is still employed in industry and has potential for further development, the disadvantages when compared to SLM have generally resulted in the most successful metal PBF companies commercializing the SLM approach.[2] SLM has seen a significant number of developments in recent years including higher power lasers and more sophisticated process modelling. However, there are still shortcomings that must be addressed to improve the process and meet emerging industrial demands. The limited number of alloy systems employed in SLM in particular limits growth of the technology into new markets. Developing new material systems with desirable physical properties is one of the primary goals of modern SLM research.[4]

1.3 Motivation and Research Objective

A significant amount of work exists on SLM of structural alloys with the primary goal of characterizing alloys adapted from traditional manufacturing techniques with high as-printed density as the primary metric of success. Various types of steel, stainless steel, titanium, nickel, and aluminum alloys have been the focus in literature.[5,8-15] Currently, there are no commercially available electrical-grade copper alloys for SLM nor does a significant amount of literature on additively manufactured copper alloys exist. Thus, the possibility of using SLM for applications requiring high electrical or thermal conductivity is drastically limited. Potential applications for SLM copper alloys

include prototyping and full production of electrical connectors, lead frames and metal contacts for integrated circuits, novel thermal dissipation and heat exchanger geometries, as well as self-lubricated bushings.[16]

The objective of this work is to characterize the microstructural evolution and mechanical property development of copper alloys fabricated via SLM. From a practical standpoint, this research will provide immediate characterization of two different copper alloys which can be used to create functional components with a wide range of physical properties. This will immediately meet demand for conductive alloys in SLM and allow the technology to be employed in new applications. Perhaps more importantly, this work will address the gap in literature to understand how the microstructure, properties, and post-processing response of common copper alloys is affected when they are fabricated via SLM. The investigation will include individual analysis of two separate alloys. A simple binary alloy will be characterized to understand fundamental SLM microstructural features and post-processing heat treatment on solid solution strengthened single phase copper alloys. This will to develop a baseline processing window and set of attainable properties. The second alloy is a high-performance precipitation hardened alloy commonly used in electrical connectors in the wrought form. This alloy will provide important insight into the property development of traditional alloys when they are fabricated via SLM. The results from both alloys will establish an understanding of some of the unique microstructural features SLM

introduces into copper alloys and how they interact with the strengthening mechanisms present in common copper alloys.

1.4 Dissertation Structure

The research performed in this investigation is divided into two distinct sections based on the foundation of selective laser melting as the common fabrication technique for two different copper alloys: binary alloy Cu-4.3Sn and alloy C70250. Chapter 2 presents a detailed background on the fundamental concepts of SLM and general copper alloy physical metallurgy that are relevant to both investigations, as well as sections specifically tailored to the particular alloys studied.

The two investigations are presented in Chapters 3 and 4 in the form of manuscripts suitable for individual publication. The first investigation in Chapter 3 is on the Cu-4.3Sn binary alloy.[17] The second investigation in Chapter 4 is on the precipitation hardened Cu-Ni-Si alloy C70250. Since the investigations are presented as publication-style manuscripts, they appear as full standalone documents with separate abstract, introduction, methods, results, discussion and conclusions sections. The introduction and methods sections are condensed versions of Chapter 2 and Appendix A tailored to each study and as a result, there is some overlap in the topics covered and the references utilized. Chapter 5 serves to summarize the broader implications of the findings, including discussion about the relationship of the findings and their implications with regards to future work on SLM of copper alloys.

CHAPTER 2

BACKGROUND

2.1 Description of the Selective Laser Melting Process

Selective Laser Melting (SLM) is a powder bed fusion based additive manufacturing technology that utilizes a high-power laser to melt metal powder. SLM is the nomenclature for modern systems intended to fully melt metal powder during fabrication. These systems were developed from the original selective laser sintering (SLS) machines used for polymers patented in 1990.[18] The technology progressed from exclusively polymer applications to indirect metal processing with a binder. Direct metal components were eventually fabricated with relatively poor properties that utilized low melting temperature metal alloys as liquid phase sintering aids. The state-of-the-art metal SLM currently utilizes full melting of powders for direct metal fabrication. The SLM designation was generally adopted in literature when direct metal fabrication became possible in the machines, and it distinguishes the machines from SLS machines intended only for polymer processing.[2]

Figure 1 shows a schematic diagram of the SLM process. A laser is generated and passes through a micro-mirror device to scan the powder bed per instructions from the build file. An f-θ lens is employed to minimize distortion and ensure the laser focal plane is flat on the powder bed. The first build layer is completed on top of a build platform, and typically a support structure is fabricated before the actual bulk of the part. After a build layer is

completed, the build platform is lowered by a piston around 20-100 µm and powder is spread over the build container for the next layer. Numerous powder spreading techniques are employed by commercial systems. The most typical systems utilize either a feed container or gravity-based dosing system in combination with a powder blade or roller. Figure 1 depicts a feed container and roller setup, but regardless the result is a new layer of powder that will be used to fabricate the next build layer of the component. The process is repeated until the part is finished. Any powder that was not melted by the laser and integrated into the component is typically vacuumed, sieved, and recycled for future builds. The part is finally removed from the baseplate by machining and any post-processing required is completed. Typical post-processing steps include heat treatment, surface finishing, and secondary machining.

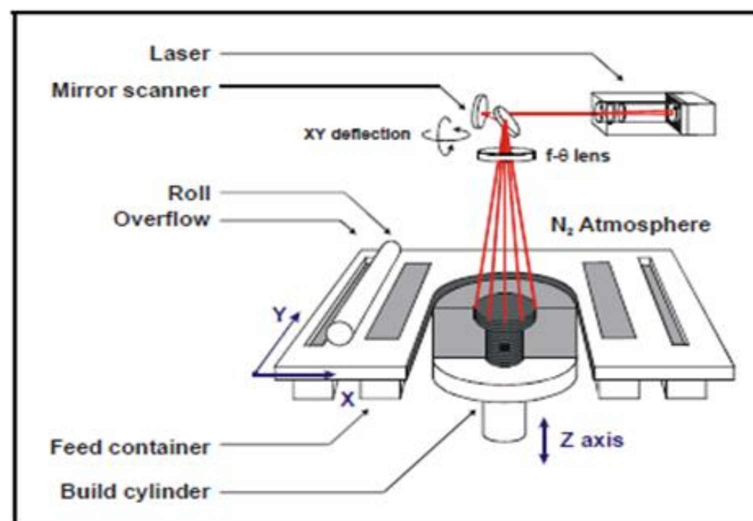

Figure 1. Schematic diagram of the SLM process.[19]

Similar to the function of shielding gas during welding, the build chamber must be an inert atmosphere to avoid incorporation of impurities in

the melt pool. The chamber is evacuated and backfilled with nitrogen or argon. Argon is more common as a shielding gas because it can be used in the processing of titanium alloys where nitrogen would react with the molten titanium. During the process, there is an additional cross flow of inert gas to carry away any ablated material or fine particulate matter that has been ejected from the powder bed by the laser. [2]

Modern metal SLM systems utilize Nd:YAG or fiber lasers with a wavelength around 1 μm in contrast to the original CO_2 lasers from SLS development with a larger wavelength (~10 μm). Figure 2 shows the effective absorptance of a powder bed compared to a dense material for various pure metals.[20] The smaller wavelength is better absorbed by metal powders, and there is an added benefit that fiber lasers are more cost effective and require less maintenance than CO_2 lasers.[4] Generally, metal alloy absorption of laser energy is poor, but the powder bed serves to redirect a significant amount of the reflected energy back to other particles and dramatically enhance effective absorptance. Most alloy systems utilized in SLM benefit from smaller wavelength radiation, but the change for copper systems is quite dramatic. For 10.6 μm wavelength radiation (CO_2 laser), pure copper has an absorptance of around 3% compared to 10% for 1.06 μm wavelength radiation (Nd:YAG laser). Considering a powder bed instead of a dense material (e.g. a copper plate), the effective absorptance of Nd:YAG and fiber laser wavelengths increases to approximately 60% for pure copper powder.[20, 21] Additional

changes in the maximum laser power available in commercial machines that provides a much greater effective heat input occurred simultaneously.

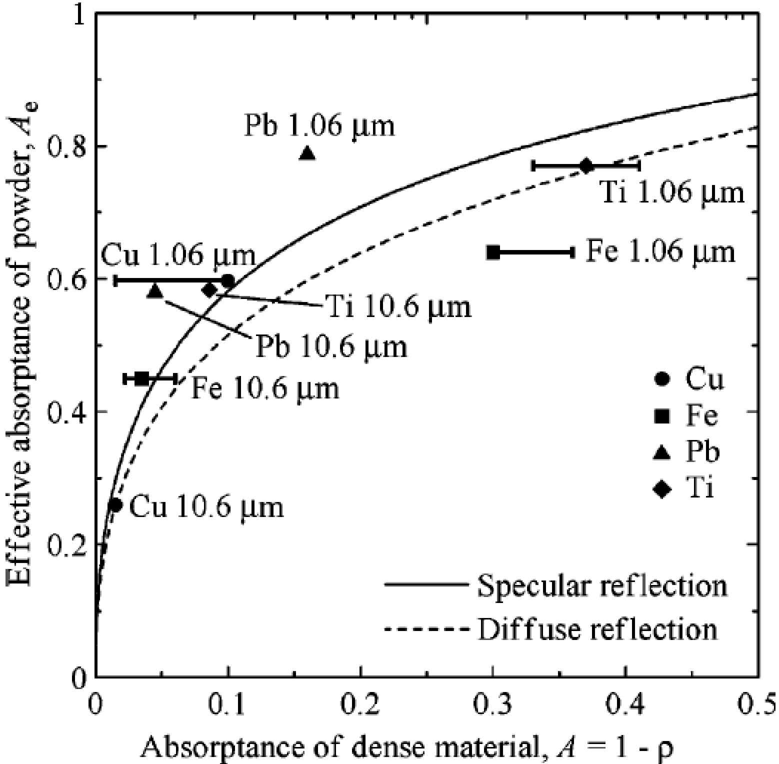

Figure 2. Effective absorptance of a deep powder bed vs dense material absorptance for various pure metals. Symbols are experimental data and lines are models.[20]

There are several processing parameters that can be altered in SLM. The most important parameters with regards to performance of SLM components fundamentally alter the applied energy density (alternatively, energy input). These parameters control the degree of melting/heating and ultimately determine the microstructure of the finished part. The primary parameters that can be manipulated are the laser power, spot size, scan speed, scan spacing and scan strategy. A large body of research exists on the

optimization of these parameters to create functional components.[2,7,9,12] Density generally takes precedence in determining successful build parameters due to the significant effect of porosity on mechanical properties, regardless of the underlying microstructure. As a result, machine parameters are typically evaluated to produce high density components. However, within the processing window of acceptably high density values, changes in laser parameters can create vastly different microstructures which affect bulk properties.[22–24] These studies highlight the importance of investigating the unique microstructural features present in different alloys fabricated by SLM.

2.2 Characteristics of Metal Alloys Fabricated via SLM

The objective of this research is to characterize copper alloys fabricated via SLM, however the utilization of copper alloys in SLM, and indeed even in most metal AM technologies, is lacking. Pure copper and high copper alloys have seen some use in electron beam melting (EBM) because high conductivity powders lend themselves well to the EBM process. Although the EBM process is in many ways similar to SLM, it is less flexible in material choice, often has a poorer surface finish compared to SLM, and is less production robust.[4] Still, the microstructures in EBM and SLM components do have some similarities. Fine cellular substructures with segregation of second phase particles from the source powder is observed in EBM copper, but the investigations are generally limited to commercially pure copper with poor mechanical properties.[25, 26] Copper phosphorous powder was used in

early SLM metal components because of its low melting temperature and good wetting properties. CuP facilitated liquid phase sintering and densification of primarily steel based powders but the copper was not utilized for its high conductivity.[19] EOS previously offered a bronze alloy (DirectMetal 20) in their range of products, with a maximum density of ~92% but it was not an electrical grade bronze and they have since stopped selling the alloy.[27] Modern Nd:YAG and fiber lasers lend themselves very well to processing of copper alloys. The absorption of copper powders is on par with other alloys that have seen significant commercial use such as 17-4 SS and Ti-6Al-4V.[21] Regardless, current utilization and research of copper alloys in SLM remains low. Numerous studies have been conducted on other metal alloys and the microstructural features present in SLM components. The findings of these studies are inherently focused on the particular physical metallurgy of the alloy being investigated, but they give crucial insight into the processing of copper alloy components via SLM.

Perhaps the most dramatic aspect of the SLM process and the source for many unique characteristics is the extremely high cooling rate of the melt pools. Investigations on aluminum alloys in SLM and accompanying models show cooling rates ranging from 10^6-10^7 K/s.[22, 28] As a result, there is a high chance of formation of metastable phases. For example, in Ti-6Al-4V, the resulting SLM microstructure is fine acicular martensitic.[29] Argon is by far the most common cover gas used in SLM, but using a cover gas with different

properties can affect the resulting microstructure. Murr et al. found that using nitrogen as a cover gas during SLM of 17-4 PH steel austenitic structures could be produced as opposed to the fine martensitic structure of argon covered components.[30] Austenitic stainless steels such as 316L retain their austenitic structure, exhibiting solidification sub-structures with cell spacing on the order of 1 μm or less.[31] Additionally, intermetallic phases and non-metallic particles have been found at the melt pool boundary, occasionally serving as initiation sites for cracking and failure. These particles include those that normally occur in the alloy as well as defects from the SLM processing atmosphere (e.g. oxygen content).[29, 32]

Figure 3 shows the solidification substructure of SLM AlSi10Mg. Cellular solidification substructures dominate in alloys fabricated by SLM. In some cases, as in Figure 3, a very small heat affected zone can be observed that affects the substructure near the weld line. The substructure tends to get finer moving away from the weld line, but the morphology does not change.

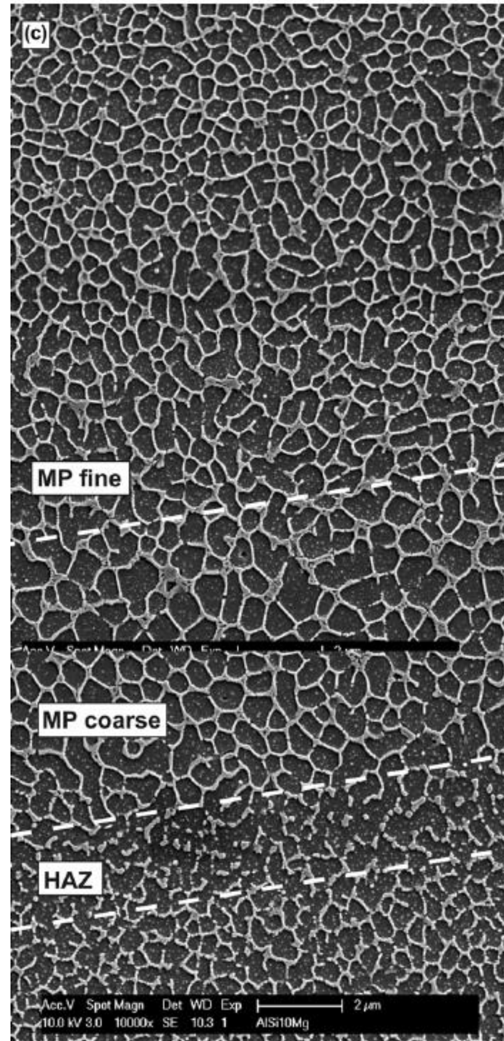

Figure 3. Change in solidification substructure moving away from the weld line in SLM AlSi10Mg.The build direction is vertical. [24]

Solidification substructures arise from solute rejection and constitutional supercooling during solidification. The substructure scale changes moving away from the weld line due to the changing thermal gradient(G) and solidification rate(R) in the weld pool and is a well understood phenomenon from welding metallurgy.[33] In casting the substructure tends to predictably change as G changes. In welding and SLM where there is a moving heat

source, the situation becomes somewhat more complicated as R is related to the heat source travel speed and varies with the location in the weld pool. Figure 4 shows a diagram of the predicted substructure features at different G and R conditions. The ratio of G/R dictates the type of solidification substructure, while the product of GxR (the cooling rate) defines the scale of the substructure. At the weld centerline GxR is minimum at the centerline of the melt pool and maximum at the fusion line. Therefore, further away from the fusion line the substructure is predicted to become finer.[33] This occurs in SLM aluminum alloys as shown in Figure 3. In welding processes, G/R ratio typically changes enough to cause changes in the solidification substructure throughout the weld pool but this does not appear to be the case in standard SLM of aluminum and ferrous alloys.[24, 30]

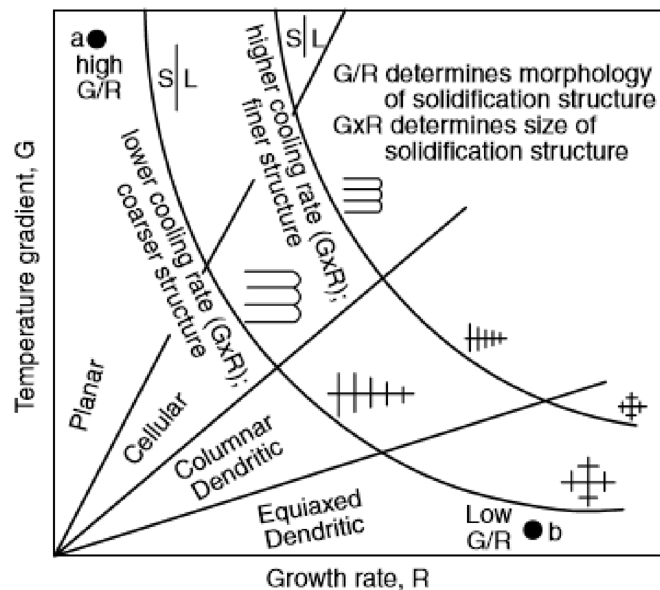

Figure 4. Variation in solidification substructure under different G and R conditions.[33]

Nearly all metallic alloys currently utilized in SLM exhibit epitaxial growth from the previous build layer resulting in elongated grains in the build direction. Titanium alloys in particular exhibit very large columnar prior β grain boundaries.[29, 34] Texture resulting from directional solidification can be tailored with scanning strategy as shown in aluminum alloy systems. Unidirectional scanning with no rotation between build layers produces a fairly strong <100> texture in the scan direction and a weaker <110> texture in the build direction. Small increases in complexity of the scan strategy nearly eliminate this texture; bidirectional scanning with rotation between layers only produces a weak <100> texture in the build direction. In parts fabricated using an island scanning strategy, preferred texture is negligible.

In titanium alloys, research has shown that the preferred growth direction of the columnar grains can change when moving from the interior of the component to the edge of the component. Near the edge of the component grains are nucleated epitaxially from loose powder particles. Although this mechanism can occur in the center of the bulk part, the grains are typically re-melted and are indistinguishable from grains that epitaxially grow from underlying bulk material. Near the edge however, the grain structure can remain resulting in a distinct change in texture in near surface layers. [34] For very deep melt pools, competitive growth could occur along the melt pool wall, but epitaxial growth still dominated near the weld centerline.[24] Similar results were later found in 316L stainless steel.[23]

Several grain nucleation mechanisms exist in the weld pool and their effect is pronounced in single-track experiments, which are conceptually very similar to traditional welding metallurgy.[33] In bulk SLM materials, the dominant grain formation mechanism is nearly always epitaxial growth due to the significant re-melting of previously solidified material. The effect is clearly shown by electron backscatter diffraction in the build direction as shown in Figure 5.

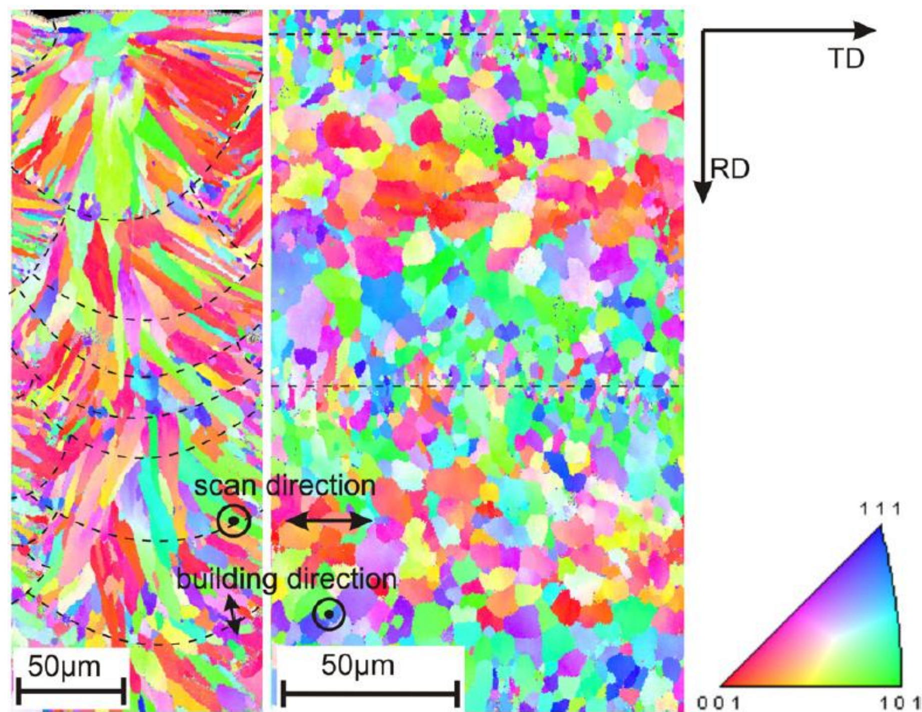

Figure 5. Epitaxial growth observed in the weld pools of SLM AlSi10Mg.[24]

In many cases, an isotropic material is desired so the scan strategy is adjusted to attain as close to this condition as possible. This is accomplished most readily by changing the laser scan direction which causes subtle changes in the solidification direction that minimize texture. However, recent findings suggest that with careful control of the shape of the laser spot,

different grain growth mechanisms can be activated. In particular, it was found that in stainless steel the solidification mode can be shifted from columnar dendritic to equiaxed dendritic to achieve some degree of an equiaxed grain structure. The study was limited to single track melt pools and further research is needed to fully develop the technique for bulk components.[22] Alternatively, there is some interest in utilizing this observation to create engineered texture in components.[32] SLM investigations of NiTi alloys have found that texture, grain size, and to some degree grain shape can be controlled by changing the weld pool characteristics via laser parameters. Multiple scanning of a single build layer can lead to further tuning of texture, but grain growth is typically observed due to reheating. [35]

Mechanical property differences between SLM and wrought materials are fairly well understood for the most popular alloys. General trends will be described here, but the presence of defects in SLM parts remains an issue in reproducibility and reliability of measured properties. Yield strength and hardness are typically higher than wrought counterparts as a result of the high cooling rate. In contrast, ductility is consistently lower than wrought counterparts due to the presence of porosity and cracking from processing.[36, 37] Vrancken et al. also demonstrated that in the case of Ti-6Al-4V conventional mill heat treatments do not produce optimum mechanical properties when applied to SLM components.[38, 39] This is particularly important in alloys that are strengthened via post-processing heat treatments

which is common in SLM since no cold deformation is imparted in the traditional sense during fabrication. Precipitation hardening SLM nickel alloys also have unique response to heat treatment compared to their wrought counterparts. SLM Inconel 718 requires a higher solution treatment temperature after processing because the high cooling rate during processing leads significant microsegregation and metastable phase formation. Longer solution treatments at higher temperatures are required to return the material to a desirable homogeneous supersaturated solid solution prior to aging. Additionally, heavy elements in nickel alloys like molybdenum can segregate strongly, leading to high concentrations of defects in the interdendritic regions. The defects in the interdendritic region lead to a microsegregation of precipitates if solution treatment was not conducted at a high enough temperature. [40]

Anisotropy of mechanical properties is present to varying degrees depending on material texture and residual stresses, and typically manifests as different properties in the build direction as compared to the X-Y plane. As expected, fatigue performance of SLM components is generally worse than wrought counterparts as a result of microstructural defects and residual stresses at the surface of SLM components.[41]

Residual stresses resulting during SLM are highly complex and depend on the processing parameters, part geometry, and the material properties. Current work from the University of Leuven on SLM components focuses on

type I residual stresses (macro-stresses). Due to the significant effect of process parameters on residual stress, it is very difficult to isolate material property effects because different parameters are needed to produce a fully dense part. In terms of geometry, the larger the part is in the build direction, the higher the maximum residual stress in the component. Along the build direction, the general trend of the residual stress is a small zone of tensile stress at the top and bottom of the part, with a broad zone of compressive stress in the center of the build. In the X-Y plane, tensile stress is generally present on the outside surfaces and internally stresses are larger in the direction of the scan. Thus, residual stresses in the X-Y plane can be significantly reduced by shortening the maximum scan vector length and scanning in different directions between layers/islands. In general, parts removed from the baseplate or built on a support structure to allow for some relaxation during fabrication have much lower residual stress in the build direction than parts still affixed directly to the base plate. Therefore, type I residual stresses can be somewhat mitigated by scan strategy and the presence of a support structure.[39, 41]

2.3 The Physical Metallurgy of Copper Alloys

2.3.1 Overview of Copper Alloys

Copper has the highest electrical conductivity of any commercial metal; it is surpassed only by silver which is prohibitively expensive for use in commercial applications. Worldwide, up to 75% of copper and its alloys

produced are destined for electrical or heat transfer applications. These applications include electrical connectors, electrical wiring and heat exchanger assemblies. For applications that do not require high strength, oxygen-free and “tough pitch” coppers are used. Although these alloys have a conductivity around 100% International Annealed Copper Standard (IACS), they are limited by their mechanical strength, with a maximum ultimate tensile stress of ~395 MPa. In practice, many applications necessitate the use of copper alloys with higher strength so understanding the mechanical properties of copper alloys destined for electrical applications is vitally important. However, the main strengthening mechanisms in metals have a detrimental effect on conductivity. Figure 6 shows the conductivity vs ultimate tensile strength for some common commercial copper alloys demonstrating this trade off. [16] This chapter will briefly discuss the main strengthening mechanisms in common copper alloys, their effect on conductivity, and their relevance to the SLM process. Following these sections the two alloys investigated in this research, Cu-4.3Sn and C70250, will be introduced. The binary tin bronze alloy is not a commonly studied composition commercially nor in literature and thus a general introduction to single phase tin bronze alloys is presented rather than a literature review. In the case of C70250, a review of current literature on the alloy in wrought form is presented. Chapters 3 and 4 will individually address metallurgy concepts as they relate to the performance of the SLM fabricated alloys characterized in this investigation.

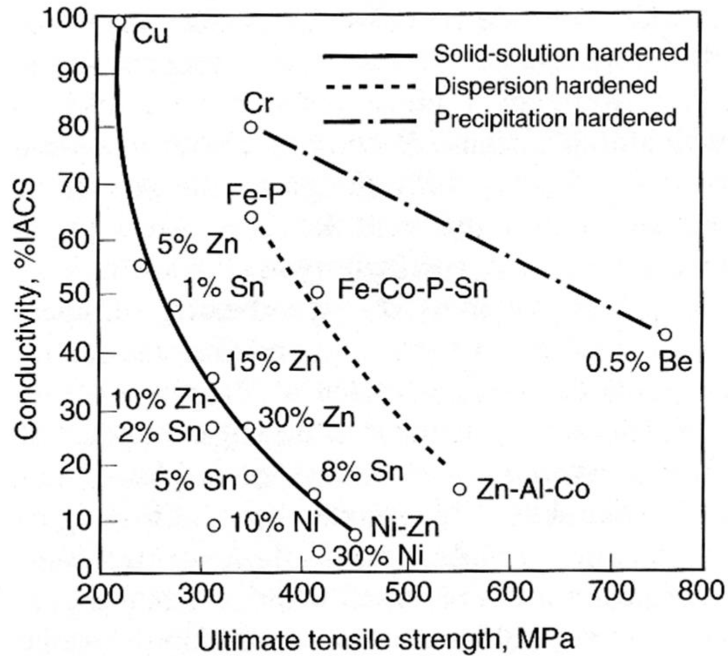

Figure 6. Conductivity vs. ultimate tensile strength for various annealed copper alloys. [16]

2.3.2 Introduction to the Conductivity of Copper Alloys

Conduction in metals results from the movement of free electrons through the crystal structure. Electrical conductivity (σ) is therefore proportional to the mobility of free electrons. Defects and impurities in alloys that scatter electrons moving through the lattice decrease the conductivity by decreasing the mean free path of electrons. Often, the electrical behavior of metals is discussed in terms of their resistivity (ρ), the geometry-independent form of electrical resistance, measured in Ωm. Electrical resistivity is related to the conductivity through a simple inverse relationship (σ=1/ρ). Matthiessen's Rule (Equation 1$\rho = \rho_r + \rho_t$) states that the total resistance of a metal is the

sum of a residual component due to defects, and a thermal component due to thermal vibrations.

$$\rho = \rho_r + \rho_t \quad \textit{Equation 1}$$

For most metals, the resistivity is proportional to temperature related by the temperature coefficient of resistivity (TCR). The TCR of metals is a positive value, leading to an increase in resistivity with increasing temperature due to increased electron scattering from thermal lattice vibrations.[43] Since copper has an inherently low resistivity, contributions to the residual resistivity from defects and impurities will have a significant effect on the total resistivity of copper alloys.[44] Throughout the next section where the major strengthening mechanisms of copper alloys are discussed, their effect on total resistivity (via the residual resistivity term) will also be mentioned.

2.3.3 Principle Strengthening Mechanisms of Copper Alloys

2.3.3.1 Work (Strain) Hardening

Deforming a metal/alloy plastically causes an increase in the number of dislocations in the material. The number of dislocation-dislocation interactions then also increases and the dislocation mobility is reduced, which in turn causes the required stress for continued deformation to rise. The accumulation and storage of dislocations is thus the basis for work hardening an alloy (note the terms work hardening, strain hardening, and cold working all refer to the same phenomenon). Applying a higher strain to the same material, and thus increasing the number of dislocations introduced and stored in the material,

increases the flow stress (i.e. the new yield stress after unloading) so that the degree of work hardening is related to the amount of increase in yield strength. This process strengthens alloys when deformation is done at temperatures below a critical value of around $0.3T_m$. Above this critical temperature, the microstructure is unstable and recovery, recrystallization, and grain growth processes can occur leading to nucleation of low dislocation density grains counteracting the work hardening effect.[45]

The way an alloy responds during work hardening can be characterized by analyzing the plastic regime of a stress strain curve. On the microstructural scale, work hardening is divided into several stages corresponding to different dislocation behavior that occur as deformation progresses. The stages are characterized by the slope of the true flow stress vs. plastic strain plot after yielding which is the work hardening rate (Θ). In single crystal samples, all stages are generally observed; however, in polycrystalline samples it is common for the material to only exhibit Stage III hardening after an initial large hardening rate at small strains that is independent of strain rate (Stage II). Stage II is athermal occurs near the yield point, but the extent of observation of Stage II work hardening in polycrystalline samples depends on the test temperature and stacking fault energy of the material (i.e. Stage III begins and affects observation of Stage II).For this reason, it is difficult to precisely define the transition from Stage II to Stage III and Stage II is currently considered more of an asymptotic work hardening rate at low strain values.[46] Stage III is

characterized by dynamic recovery processes and the work hardening rate during this stage varies with temperature and strain rate. From a practical standpoint, Stage III describes most of the regime where materials are being work hardened (with the near yield Stage II that is transient describing the initial low strain portion). The simplest differential strain-hardening law, the Voce relation, is fairly accurate for polycrystals and an improvement over simple power law relations. The Voce relation describes a linearly decreasing work hardening rate with an increasing stress. The differential version of the Voce relation is shown in Equation 2.

$$\Theta = \frac{\partial \sigma}{\partial \epsilon_p} = \Theta_0 \cdot \left(1 - \frac{\sigma - \sigma_Y}{\sigma_s - \sigma_Y}\right) \qquad \textit{Equation 2}$$

Where σ is the true stress, ϵ_p is the plastic strain, Θ_0 is the initial work hardening rate, σ_Y is the yield strength and σ_s is the saturation stress. Figure 7 shows a schematic diagram of the work hardening rate versus stress with the Voce equation parameters indicated on the axes. Curves a and b are for different strain rates and serve to indicate that tests at different strain rates will produce different relations even if the material has the same yield strength.[47] Note that the bottom of the curves do not actually reach the saturation stress due to the activation of higher order work hardening stages that are not fully understood. The linear approximation works very well for FCC metals that are either pure or solid solution strengthened (discussed later in this chapter) because the dislocation accumulation mechanisms are the same. However, in multiphase systems, there is deviation from the linear nature of the curve due

to dislocation interactions with the second phase and this can be utilized to infer some information about the morphology of the second phase.[47, 48]

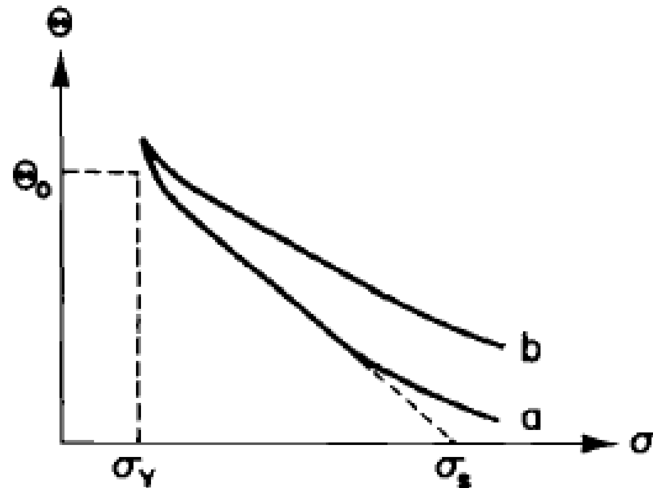

Figure 7. Work hardening rate (Θ) versus stress (σ) for different strain rates (a and b) with the Voce parameters specified on the axes.[47]

Copper and its alloys have good work hardening behavior and are readily cold worked in excess of 90% reduction in area as a finishing step to improve properties for commercial applications.[16, 44] Work hardening is especially utilized in pure copper where the low recrystallization temperature limits the applicability of Hall-Petch strengthening due to grain growth at moderate temperatures. Work hardening only decreases the conductivity of copper alloys by at 1-3% IACS, however it can improve their strength substantially. The dislocations introduced from deformation shorten the mean free path of electrons, but the effect is minimal.[43]

Work hardening is not available as a strengthening mechanism directly in the SLM process. Similar to casting, SLM is a near-net-shape solidification

process; there is no inherent deformation involved that would provide work hardening without the addition of a post-processing step. However, there is a significant amount of residual stress generated during solidification in SLM that can lead to a high dislocation density structure providing a somewhat similar strengthening effect.[42] Additionally, work hardening behavior can be utilized to understand the mechanical response of alloys produced via SLM, particularly in the case of understanding the morphology of second phase precipitates.[49]

2.3.3.2 Hall-Petch Strengthening (Grain Boundary Strengthening)

Just as adding barriers to dislocation motion in the form of more dislocations increases the yield strength in work hardening, grain boundaries serve as an effective barrier for dislocation motion and increase strength. Dislocations cannot easily slip across a grain boundary because the crystal structure is different in the second grain and the grain boundary results in a discontinuity of the slip planes in each grain. The relationship between yield strength (σ_y) and grain size (d) is described by the Hall-Petch equation (Equation 3).

$$\sigma_y = \sigma_0 + \frac{k_y}{\sqrt{d}} \quad \textit{Equation 3}$$

Where σ_0 and k_y are constants that vary based on the alloy and are generally related to the lattice resistance to dislocation movement and the relative hardening of grain boundaries, respectively. Although some alloys do not follow the Hall-Petch equation to very small grain sizes, copper alloys have

been found to adhere to Equation 3 down to around 10 nm.[50] Traditionally manufactured wrought copper alloys, particularly high strength copper alloys, are regularly hot worked to refine the grain structure and increase strength per the Hall-Petch relationship.

Andrews *et al.* was able to measure the contribution of grain boundaries to resistivity in polycrystalline copper and aluminum. They found that the specific grain boundary resistivity was independent of impurity content, and had a small dependence on temperature. They determined that the increase in resistivity attributed to grain boundaries ($\Delta\rho_{gb}$) could be described by Equation 4.[51]

$$\Delta\rho_{gb} = \frac{2}{3}\,\rho_{sgb}\left(\frac{S}{V}\right) \quad \textit{Equation 4}$$

Where the specific grain boundary resistivity, ρ_{sgb}, is equal to $3.12\times10^{-16}\ \Omega\ m^2$. S/V is the grain boundary surface area to volume ratio for a grain with diameter, d. S/V~ 2.37/d using the assumption that the grains are tetradecahedral.[50] Using Equation 2 and the S/V approximation, an estimation of the contribution to resistivity can be determined for a range of grain diameters. The grain boundary contribution to resistivity is negligible for grain sizes above around 1 μm. Although some unique processing methods exist to produce nano-grained copper alloys, common grain sizes are far above this threshold and thus contributions from grain boundary resistivity is usually ignored.

Current SLM research indicates that there is some degree of control over grain nucleation and growth which affects the final grain size. Laser parameters and intensity profiles have been altered for aluminum, nickel-titanium, and stainless steel alloys to control the grain size and texture with some degree of success.[22, 24, 35]. Additionally, changes in alloy composition have the capability to introduce inoculants that promote heterogeneous nucleation and limit the amount of epitaxial growth that occurs during solidification. In particular, this phenomenon has been proven effective in scandium modified aluminum alloys. This mechanism was proven with pre-alloyed powder, although in principle the amount of inoculant could be varied by mixing two different powders to vary the composition during each production run.[51, 52] In practice, however, the grain size of alloys produced via SLM is essentially fixed. Commercial applications utilize a set of ideal parameters based on density experiments performed either internally or by the machine manufacturer. In the latter case, the "optimum" parameters are supplied to owners of the machine but in both scenarios the parameters are normally held constant after optimization. Therefore, the contribution to strengthening from grain size is fixed in the as-printed condition. Post-processing heat treatments could potentially alter the grain size via recrystallization directly from the as-printed structure. Studies on post-SLM heat treating and hot isostatic pressing (HIP) generally indicate that grain refinement directly from the as-printed condition is not possible and in fact

grain growth occurs that decreases strength per Equation 3. Investigated alloys include Ti-6Al-4V, steel, and Al-12Si; these studies demonstrate significant coarsening of microstructural features during post-processing heat treatment.[53-55]

2.3.3.3 Solid Solution Strengthening

Work hardening and grain refinement can strengthen pure metals and alloys alike. However, adding solute atoms to a pure metal while retaining a single phase results in an alloy that is solid solution strengthened. Solute atoms with a different atomic radius than the matrix produce distortion in the surrounding lattice. These distortion fields interact with dislocations making it more difficult for dislocations to move through the lattice thereby increasing strength. The amount of strengthening depends primarily on the relative size difference of the solute/matrix atoms, the stress field associated with the solute in the lattice, and the amount (concentration) of solute atoms in the matrix.[45] Many of the most ubiquitous copper alloys utilize solid solution strengthening. Figure 8 shows the approximate strengthening effect of various solute atoms in an FCC copper matrix at room temperature.[16] Two of the most common solid solution strengthened alloys are phosphor bronze, Cu-Sn alloys, and brass, Cu-Zn alloys. A note on copper alloy nomenclature: technically a bronze is copper plus any other alloying element; for example “aluminum bronzes” are Cu-Al alloys, but the use of bronze without an elemental descriptor was traditionally used to refer to Cu-Sn alloys. In

contemporary usage, “phosphor bronze” refers to modern Cu-Sn alloys that have been phosphor de-oxidized, despite the fact that Sn is the principal alloying element. Brass, however, is still used to exclusively refer to copper alloys where Zn is the primary alloying element (even if other elements are present in smaller amounts). Sn and Zn have relative atomic diameter differences compared to copper of -15% and -4%, respectively. Examining Figure 8, the difference in strengthening potential as a result of the size effect is evident. The strengthening effect has influences outside atomic radius difference, but Sn and Zn are both substitutional lattice impurities so in this case the atomic size difference is dominant. Sn has a much higher strengthening potential than Zn, despite the fact that much more Zn (around 35%) can be dissolved in the copper matrix compared to Sn (around 10% solubility in practice). However, Zn has a very good combination of solubility and strengthening effect and brass alloys are the most commonly used copper alloys. Cu-Sn alloys are more commonly utilized when high strength and good wear resistance is required.[16]

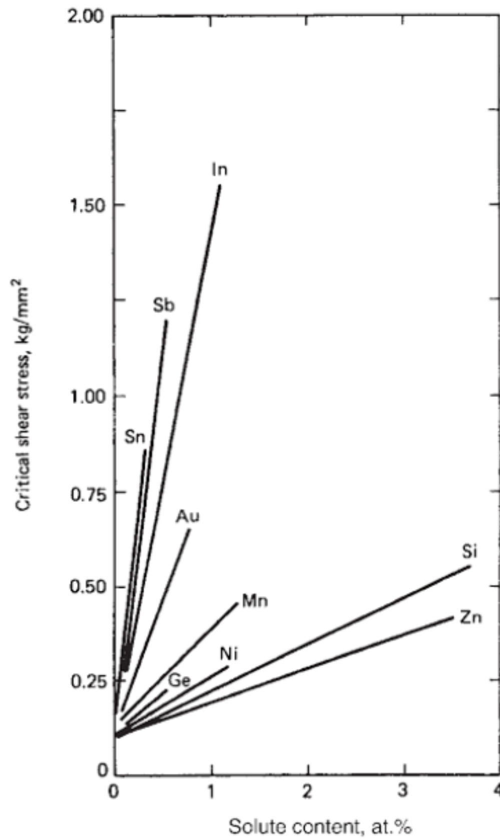

Figure 8. Approximate effect of solute content on the critical resolved shear stress at room temperature.[16]

In simplified/colloquial language, one may say that how well a solute atom “fits” in the native copper matrix determines the degree of the solid solution strengthening effect of that atom. Unfortunately, the same is true for how detrimental a solute atom will be to the conductivity of copper by scattering free electrons. In other words, elements that are good solid solution strengtheners in copper also increase the resistivity significantly. The amount of resistivity increase is controlled by similar variables as solid solution strengthening: amount, atomic radius, crystal structure and electronegativity among other factors.[43] Amongst the strengthening methods utilized in

copper alloys, solid solution strengthening by adding solute atoms (i.e. impurities) to the copper matrix has the most deleterious effect on conductivity.

The mechanism for increases resistivity when adding solute atoms to the copper matrix is enhanced electron scattering. Nordheim's Rule (Equation 5) describes the increase in the residual component of resistivity due to impurities with respect to the concentration, X, of an impurity solute.

$$\rho_I(X) = CX(1 - X) \quad \textit{Equation 5}$$

Where C is a constant called the solution resistivity coefficient or the Nordheim coefficient. The value of C depends on the base metal and impurity atom characteristics such as atomic radius, crystal structure and electronegativity. Although it is a simplification and does not account for additional conduction electrons due to alloying or enhanced scattering effects of some impurities, it is a reasonable estimation for most solute atoms at low concentrations. An adjusted coefficient that varies with composition, C_{eff}, must be used in the case of alloying additions greater than a few percent.[57] Figure 9 shows the effect of small additions of various elements on the resistivity of copper at room temperature (the Nordheim coefficient for each element can be approximated as the slope in Figure 9).[58] The effects are quite different for various elements, and additions under just 0.1 weight% can dramatically increase the resistivity of a copper alloy. There is an obvious tradeoff of lower conductivity for increased strength in copper alloys, reiterating the trend observed in Figure 6.

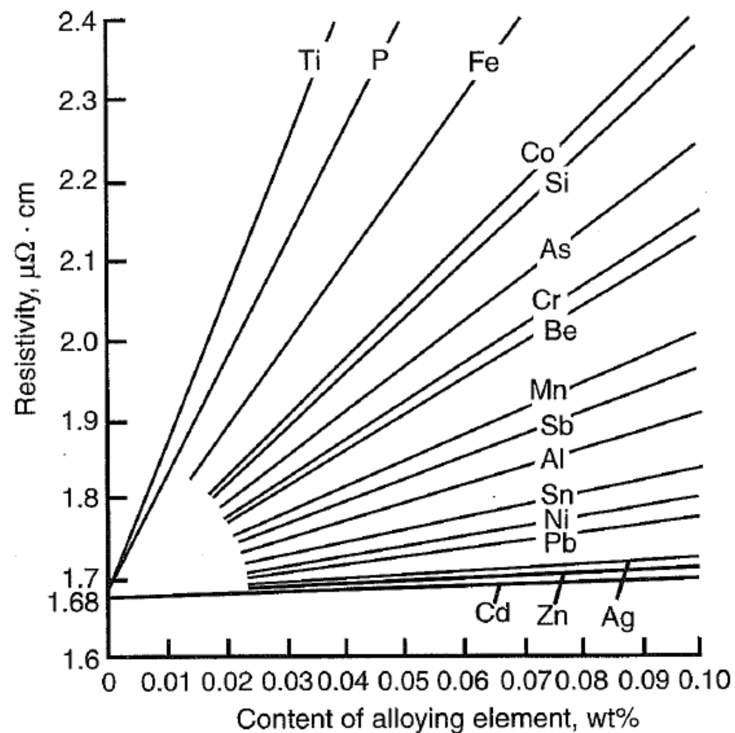

Figure 9. The effect of small additions of solute atoms on the resistivity of copper.[58]

Solid solution strengthening is easily accomplished in SLM since it depends on the alloy chosen rather than specific processing conditions. In most applications, pre-alloyed powder of a fixed composition is used repeatedly, and thus the amount of solid solution strengthening does not vary from run-to-run. For example, 316L stainless steel is a single phase (austenite) solid solution, and it is available commercially for SLM. Segregation upon cooling must be well understood if a single phase solid solution is desired. For some alloy systems, segregation may be significant enough that, although in the homogenized (nominal composition everywhere)

state it is a single phase, the segregation can cause the formation of secondary phases in the interdendritic regions. A secondary homogenization heat treatment would then be required to dissolve the unwanted phases back into the matrix.

2.3.3.4 Precipitation Hardening (Strengthening)

Precipitation hardening involves the formation of nanometer scale precipitates that interact with (impede the motion of) dislocations. Precipitation hardening requires increasing solid solubility of solute atoms with temperature that allows for “solution treatment”. During solution treatment at high temperature, the alloy is a single phase with all of the solute atoms dissolved in the matrix. Upon quenching, a super-saturated solid solution is formed with all of the solute atoms “stuck” in the matrix because there was not enough time to form an equilibrium second phase. Heat treatment at a moderate temperature (in the two phase region), termed artificial aging, results in a high precipitation rate and a network of fine precipitates are formed in the matrix. The ideal temperature for aging is one that balances the driving force for precipitation (higher at lower temperatures) with the diffusion rate which is required to form and grow the precipitates (increases with temperatures).[44, 45]

As the particles nucleate and grow, the mechanisms for dislocation-particle interaction, and hence the strengthening mechanisms, change. Figure 10 shows a schematic representation of the strengthening mechanisms active

during artificial aging of a precipitation hardening alloy.[45] Note that the aging time may be replaced with the particle radius and the plot would appear the same. The SSS curve refers to solid solution strengthening. The contribution from SSS is maximum before any particles have nucleated (t=0) because all the alloying elements are in the super-saturated solid solution matrix. However, as precipitation progresses and the alloying elements are forming the second phase precipitates, the contribution of SSS approaches zero. There are two primary mechanisms by which dislocations can pass through a second phase particle: shearing (cutting) and looping. The bulk strength of alloys with precipitates is highly dependent on the particle radius and volume fraction. Volume fraction is typically determined by the alloy composition, but obviously the particle radius changes throughout aging as the particles grow due to Ostwald ripening. The changing particle radius affects both the strengthening contribution from a particular mechanism and the active mechanism. Dislocations will bypass particles in whichever way requires the least energy. Therefore, the intersection of the curves, corresponding to the shearing to looping transition in Figure 10 is extremely important. Although mechanisms and intricacies exist for dislocation-particle interactions, for most important commercial precipitation hardening alloys the simplified discussion presented here is adequate.

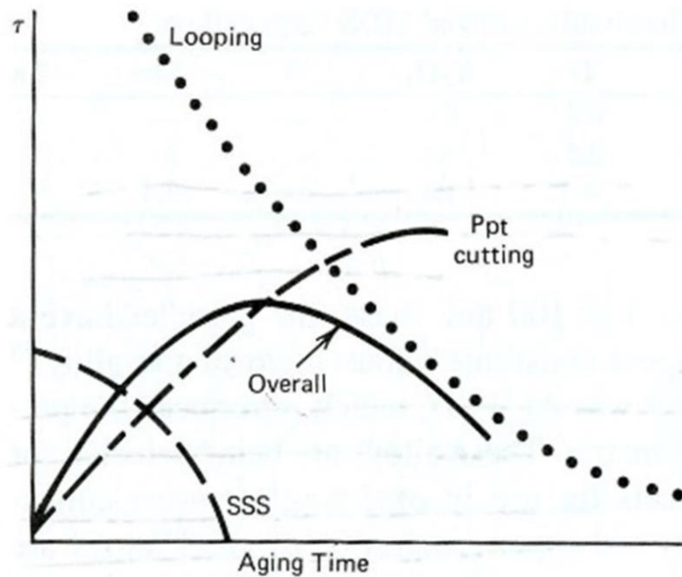

Figure 10. Schematic diagram of the major strengthening mechanisms active during a precipitation hardening aging heat treatment.[45]

Shearing requires the particles have some degree of coherency with the surrounding matrix. Even if a dislocation can shear through a precipitate, there is some resistance to dislocation motion through that precipitate which provides a strengthening effect. Calculations of how much resistance a shearable precipitate introduces to dislocation motion depend on the particular nature of dislocation-particle interaction. The two most important mechanisms for particles to resist shearing are antiphase boundaries (APB) and coherency strengthening (misfit hardening). In a particular alloy, typically only one mechanism is active determining the shape of the cutting curve in Figure 10.

APB occur in alloys that have ordered precipitates (e.g. γ' in Ni alloys). If the precipitate is ordered, a dislocation shearing through it would destroy the ordering and create an extremely unfavorable condition. Essentially, the dislocation from the matrix has a Burgers vector half the length of an ideal

dislocation in the particle. Two identical dislocations may cut through the precipitate, but an APB is formed between them and the APB energy is quite high and is therefore very effective at strengthening.[45, 59] There is also some contribution to strengthening from interfacial energy effects for particles where an APB is formed, but the contribution is usually negligible compared to the APB energy.[49] Alternatively, If a particle has the same crystal structure as the surround matrix, but a slightly different lattice parameter, dislocation shearing through the particle will be inhibited by coherency strengthening. The most important variable for coherency strengthening is the misfit strain between the particle and the matrix. Greater misfit strains provide more strengthening, however they also lead to more rapid Ostwald ripening which lowers strength.[45]

If a particle cannot be sheared, Orowan looping occurs. Orowan looping typically occurs if the particle is incoherent with the matrix and thus dislocations cannot pass into the particle, or if looping becomes easier than shearing because the particle has grown too large and the interparticle spacing increases (particle radius(r) on the order of >15nm).[59] Orowan looping requires a dislocation line to bend around the precipitate and the difficulty of looping is tied to the interparticle spacing. The nature of the particle is inconsequential (assuming of course it cannot be sheared) to the increase in strength. Initial estimations by Orowan used a square grid on the slip plane, but the interparticle spacing was later refined by Ashby using particle statistics

to relate the increase in strength to more easily measured values of the particle size and volume fraction.[49, 59]

Particle resistance to shearing increases as the particle radius increases. However, as particles become larger and therefore the interparticle spacing increases, looping becomes easier than the shearing mechanisms even if the particles can be sheared in theory. The exact particle size when the transition occurs varies based on the particular alloy system, but it is typically around 15nm. Thus, the Orowan looping mechanism (non-shearable particles) defines the maximum possible precipitate strengthening at any given particle size and volume fraction. In practice, it is extremely difficult to create large volume fractions of non-shearable particles at the size range where Orowan looping results in a greater increase in strength than shearable precipitates. In contrast, large volume fractions of sub 15nm shearable precipitates are readily produced in common alloy systems. The peak strength of precipitation hardenable alloys is typically where the transition from shearing to looping occurs as shown in Figure 10. Aging past this transition (peak age) lowers the overall strength of the alloy and is referred to as over aging.

The characteristics of second phases generally have a very small effect on the resistivity of precipitation hardened copper alloys. In Cu-Ni-P precipitation hardening alloys for example, Miyake and Fine found that electron scattering by particles was only a major factor for alloys with particles approximately 1 nm.[60, 61] Precipitate sizes in the peak age condition are

much large and as a result don't directly scatter electrons strongly. For larger particles in a copper matrix (i.e. the particle conductivity is much lower than the particle), the effective resistivity (ρ_{eff}) of the mixture is given by Equation 6.[57]

$$\rho_{eff} = \rho_M \frac{(1+\frac{1}{2}X_p)}{(1-X_p)} \quad \textit{Equation 6}$$

Where ρ_{M} is the resistivity of the matrix and X_p is the volume fraction of particles. For this equation to be valid, ρ_{M} must be less than 10% of the particle resistivity. This condition is typically met in copper alloys since the copper matrix has such a low resistivity. If the particles and matrix have similar resistivity values, a simple rule of mixtures applies. Strengthening precipitates are typically present in copper alloys at volume fractions from 1-5+%. Even at the high end of volume fractions of strengthening precipitates, the effective resistivity increases on the order of the volume fraction of the particle. Although this equation ignores coherency strain effects and likely underestimates the increase in resistivity in precipitation hardened alloys, it provides a reasonable first approximation. Although the contribution of second phases to resistivity described by Equation 6 is small, second phase particles will also indirectly alter the resistivity of the alloy. Particles of varying sizes affect the solute concentration in the vicinity of smaller particles as described by the Gibbs-Thomson effect.[62] Variations in particle size introduce a concentration gradient in the surrounding matrix which will detrimentally affect the conductivity of the alloy via Nordheim's Rule (Equation 5). Miyake and

Fine were able to combine the governing equations for these effects to show a quantitative relationship between resistivity and particle radius in Cu-Ni-P alloys.[61] The results indicate that any decrease in solute content in the matrix (in their case via particle growth) decreased resistivity as expected at the expense of the strength of the material. Thus, over aging continues to increase the conductivity of precipitation hardening alloys to a certain degree.

Precipitation hardening is the ideal strengthening mechanism for SLM. The high cooling rate of SLM makes it possible to avoid a solution heat treatment in some alloys which can improve process efficiency and reduce costs. Additionally, heat treatment to increase the strength via precipitation retains the inherent advantages of AM. Precipitation hardening alloys fabricated via traditional methods (extrusion for example with aluminum alloys) still requires post-process heat treatment to achieve peak strength, so AM is not a disadvantage in utilizing precipitation hardening compared to conventional manufacturing technology. Indeed, there are several precipitation hardening alloys commercially available for SLM.[27]

2.3.3.5 Dispersion Strengthening

Dispersion strengthening is differentiated from precipitation hardening in that the fine particles introduced to the alloy during processing are not inherently reliant on the alloy chemistry or increasing solubility with temperature. The most common techniques for making dispersion strengthened alloys are mixing of dispersoid powder with copper powder,

mechanical alloying, and internal oxidation. As a result, the particles in dispersion strengthened alloys are incoherent and unrelated to the matrix phase. The particles cannot be cut/sheared and follow the Orowan looping mechanism as described in the previous section. The particles do not dissolve into the matrix, and thus the high temperature stability of the alloys is greater than that of precipitation hardened alloys. This advantage dictates their common applications of resistance welding electrodes and other high current/temperature electrical contacts. However, precipitation hardening has the capability form a higher volume fraction of finer strengthening precipitates, so the low temperature strength of dispersion strengthened alloys is typically lower than precipitation hardened alloys as shown in Figure 6.

Oxide particles are the most common particles used in dispersion strengthened copper alloys, hence the term Oxide Dispersion Strengthened (ODS) alloys. In copper alloys, alumina particles (up to ~2.7 volume% particles) are the most common although silicon, beryllium, and yttrium oxide particles in copper have been demonstrated to be effective ODS systems.[59] The method of internal oxidation provides the finest and most uniform dispersion of particles, but it is resource intensive. Since oxide particles are incoherent and have very high resistivity, the conductivity of ODS alloys is described well by Equation 6. The low volume fraction of oxide particles typically found in commercial ODS alloys implies a high conductivity, however

in reality residual alloying elements in the matrix decrease the conductivity below values calculated by Equation 6. [16]

Oxide dispersion has seen limited application in SLM and AM in general. In the case of EBM copper and SLM steel, oxide particles that are present in the source powder for AM remain through processing, despite complete melting of the source powder. The oxide particles apparently do not have time to significantly migrate or collect on top of the melt pool and are pushed to the intercellular regions during solidification. Since the cooling rate, and therefore the solidification substructure, in PBF processes is very high, the particles are well dispersed.[25, 63] In SLM 316L stainless steel, fine nanometer scale oxide particles were found in the finished component despite their lack of presence in the source powder, indicating that SLM may be a viable technique for in-situ oxidation to fabricate ODS alloys.[64]

2.3.4 The Cu-Sn System

Figure 11 shows the copper tin phase diagram. Tin bronzes are commercially available up to around 15% tin by weight. Alloys above 10% are used for bearing and gear applications where good wear resistance is the primary concern. Alloys destined for electrical applications fall below 10%, and more typically below 5% tin to ensure an acceptable combination of strength and electrical conductivity. Around 8% tin is the threshold for forming second phases during most solidification processes. The solidification range for Cu-Sn alloys is quite large leading to a significant amount of solidification segregation

(coring). Above a nominal concentration of 8% tin, the extent of segregation in typical casting processes is enough to form δ-phase in the intercellular regions (the tin concentration reaches ~13.5% before forming δ). δ is a hard phase that can be beneficial to the wear rate in gear applications, but it is not typically found in the lower tin concentration alloys used in electrical components. According to the phase diagram, it should be possible to precipitation harden copper tin alloys via the ε phase. However, Figure 11 is an equilibrium phase diagram and the precipitation kinetics of ε are far too slow to practically be utilized as a precipitation hardening system.

Tin bronzes are commonly phosphor deoxidized to ensure the alloy has a reasonable amount cuprous oxide (Cu_2O). If the oxygen content of the alloy is too low, hydrogen embrittlement can readily occur. If the oxygen content is too high, formability is reduced. In casting, although a small amount of cuprous oxide is not exceedingly deleterious to mechanical properties of electrical conductivity directly, excess oxide leads to discontinuous solidification and a significant degree of porosity in the solid component. Copper alloys are unique in the melt exhibiting a eutectic at 0.39 weight% oxygen and thus an appreciable amount of cuprous oxide can form during solidification and be found throughout the casting. Cuprous oxide exists as a liquid phase in melt and cannot be easily separated as in the case of easily separated oxide dross in other alloy systems.[16] Fortunately, most other elements have a higher affinity for oxygen than copper, and the oxygen content in the melt can be

reduced by reaction with other elements which keeps the formation of cuprous oxide to acceptable levels (~0.5 weight%). In the case of commercially pure copper, this limits the amount of impurity elements in the matrix by forming immiscible oxides but in alloys where some alloying elements are desired in the matrix the oxygen must be removed prior to solidification.[65] Phosphorous is the most economical and effective deoxidizer. It forms a liquid slag of cuprous phosphate that easily separates from the rest of the melt and can be skimmed from the surface of the melt. The improved castability and lower oxide content in the alloy comes at the price of reduced conductivity, as shown by the significant effect of residual phosphorous on conductivity in Figure 9.[16]

There is no literature investigating Cu-Sn alloys fabricated via full melting SLM. Examining the established processing knowledge of single phase copper alloys for wrought and casting applications gives some insight into important microstructural features. The degree of segregation will be particularly important to investigate to ensure that no undesirable second phases are formed. Additionally, oxygen incorporation into the alloy and its interaction with the tin is of interest. The source powder for SLM could have an oxide shell and increase oxygen content in the finished part.[6] In general, however, the Cu-4.3Sn alloy that is investigated in this research is a fairly simple single phase alloy. The primary purpose of studying Cu-4.3Sn in this investigation is to serve as a simple fundamental system to gain insight into

how relatively high copper alloys respond to SLM and secondary post-processing.

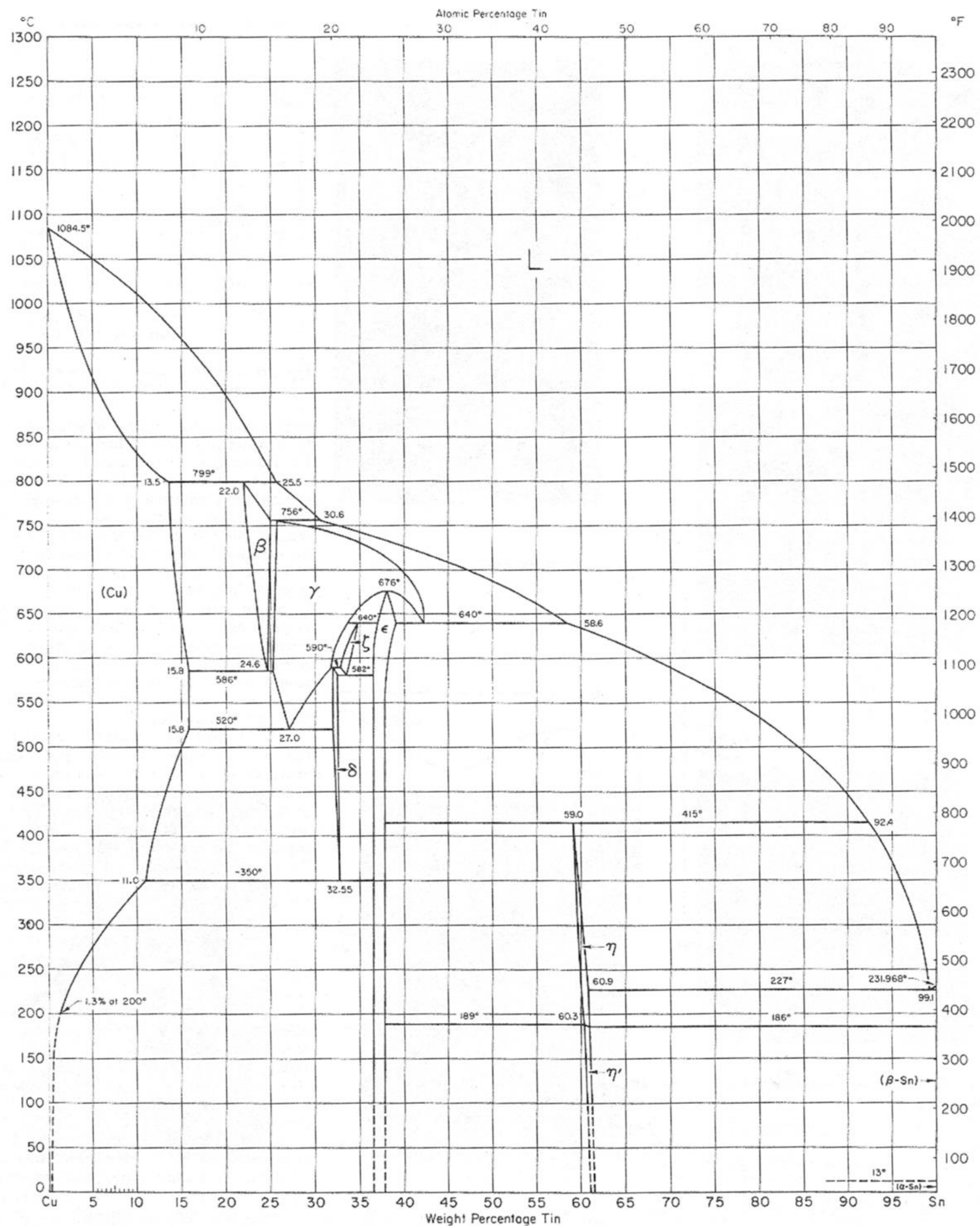

Figure 11. Copper-Tin equilibrium phase diagram. [16]

2.3.5 The Cu-Ni-Si System

Precipitate strengthening of copper alloys via the formation of silicide particles was first introduced by Corson in 1927, which lead to the alloy system commonly being referred to as “Corson alloys”. [66] The first and most common generation of the alloys has nickel compositions between 2 and 3 percent and typically contain 2-3% volume fraction of precipitates (UNS C70250/ASTM B422). The composition specifications for alloy C70250 are presented in Table 1.These alloys have yield strengths around 700 MPa and have an electrical conductivity of around 35-40% IACS (International Annealed Copper Standard) in the peak aged condition. CuNiSi alloys are most commonly manufactured via hot and cold rolling into plate and strip with subsequent cold forming into a final electrical product. CuNiSi alloys are not implanted directly from casting, and typically the structure is homogenized and thoroughly wrought after processing. As a result, literature focuses exclusively on wrought products and solidification phenomena in the alloy is not addressed.

Table 1. UNS C70250 alloy composition specifications.[67]

Element	**Cu**	**Ni**	**Si**	**Mg**	**Fe max**	**Zn max**	**Mn max**	**Pb max**
Weight %	Bal.	2.2 - 4.2	0.25 - 1.2	0.05 - 0.30	0.20	1.0	0.10	0.05

The primary interest in CuNiSi alloys comes from a desire to replace traditional copper-beryllium alloys for applications requiring high strength and

good conductivity. Beryllium containing metals can cause lung disease and they are increasingly discouraged from use, particularly in the European Union; however, CuNiSi alloys generally lag behind their CuBe counterparts with regards to physical properties and cannot reach yield strengths greater than around 900 MPa . Regardless, the good strength, conductivity and stress relaxation resistance of CuNiSi alloys makes them ideal candidates for electrical applications requiring moderately-high strength. [16] Corson had originally suggested that the strengthening particles were δ-Ni_2Si and presented a quasi-binary phase diagram in his original work. [66] Several groups subsequently disputed the claim and insisted that the strengthening silicides were other Ni_xSi_y phases. Transmission electron microscopy (TEM) and diffraction techniques were eventually utilized to study the particles, and the strengthening silicide particles were most notably studied in two key papers by Lockyer and Noble circa 1994 where many previous suggestions about the silicide particles were confirmed. [68]

Lockyer and Noble studied the strengthening precipitate morphology in a Corson alloy with a composition of approximately 2% Ni and 0.6% Si. The exact composition was not determined, but the range falls within the C70250 specification. TEM and Vickers hardness were utilized to study the precipitate structure and aging behavior. Water quenching produced precipitate free material for samples 1-2mm thick. Precipitates were found to have formed after just 1 hour at 450°C, and significant strain contrast was observed around

the precipitates at aging times up to around 100 hours, conforming to earlier x-ray diffraction studies by Dies *et al.* which found the precipitates to have an orthorhombic crystal structure in a well-defined crystallographic direction with respect to the matrix. Electron diffraction showed that the same a/b ratio of the orthorhombic unit cell found by Toman (1.4088) for δ-Ni_2Si. [68] As a result, Lockyer and Noble confirmed the precipitates were in fact disc-shaped orthorhombic δ-Ni_2Si oriented with respect to the copper matrix such that $(100)_{matrix}$ || $(001)_{ppt}$ and $[011]_{matrix}$ || $[010]_{ppt}$ with an $(011)_{matrix}$ habit plane. A dark-field micrograph of the precipitates is shown in Figure 12.

Figure 12. Dark-field micrograph of a CuNiSi alloy aged at 450°C for 750 hours with the beam direction parallel to the <001> of the copper matrix using the $(020)_{ppt}$ diffraction spot for imaging.[68]

The precipitates are readily observed in dark-field along either the $<001>_{Cu}$ or the $<111>_{Cu}$. The diffraction spots from the precipitates are skewed by their disc-like morphology and lattice strain.[69] Additionally, several

variants of precipitates produce diffraction spots simultaneously and thus the resulting diffraction patterns are a combination of the different precipitate orientations that are parallel to the beam along with secondary diffraction effects. The specifics of these effects and an explanation of the resultant diffraction pattern was addressed by Jia *et al.* several years after Lockyer and Noble initially explained the diffraction patterns. Figure 13 shows simulations of precipitate diffraction patterns that combine with secondary diffraction effects that result in the experimentally observed patterns along the $<111>_{Cu}$ projection.[70] An analogous description is given for the $<001>_{Cu}$ projection to similar effect. The misfit between the precipitates and the matrix for the b and c directions was estimated to be around 1%, indicating that the interface on the habit plane is highly coherent.[68]

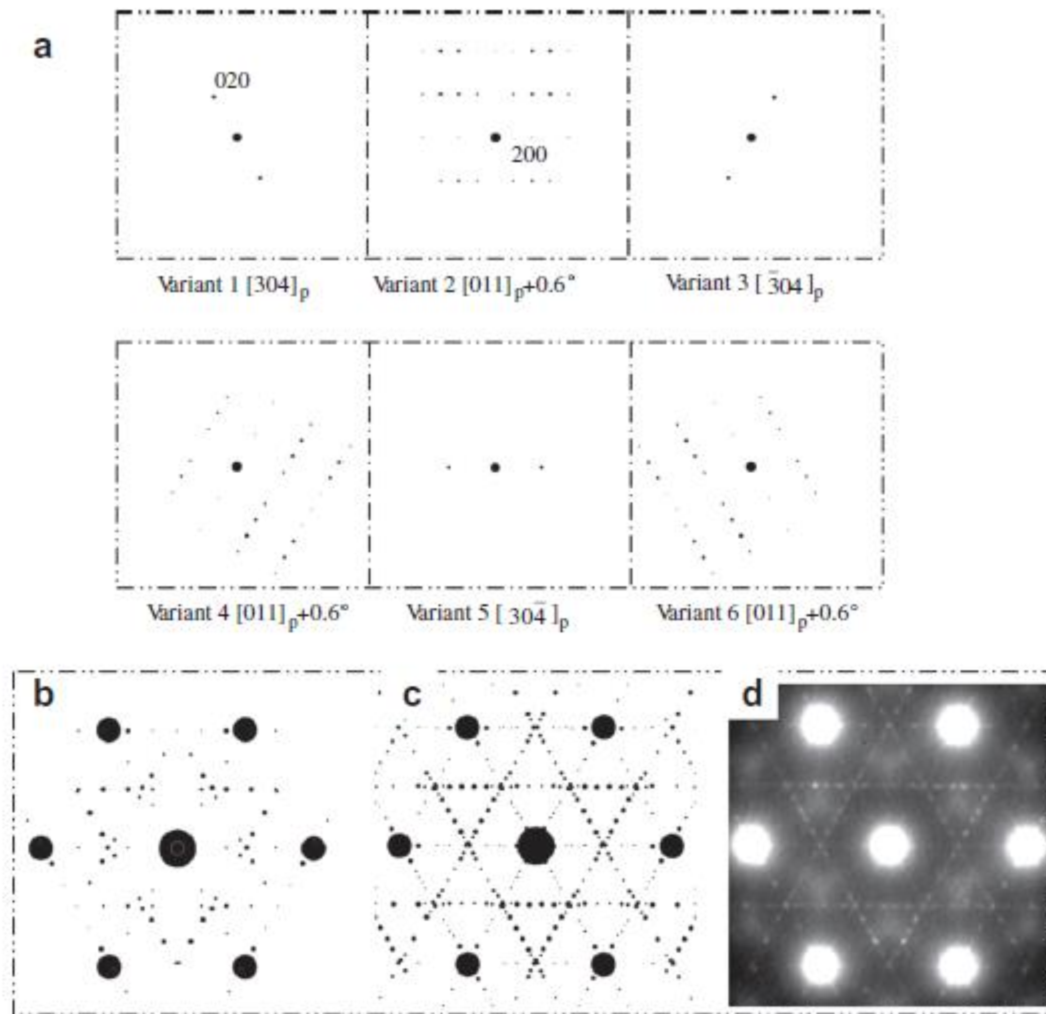

Figure 13. (a) Simulations of the 6 δ-Ni_2Si diffraction patterns that are present when viewing along the <111>$_{Cu}$ (b) the copper and δ-Ni_2Si patterns superimposed and (c) secondary diffraction effects added to (b) next to (d) an experimental pattern.[70]

Figure 14 shows the change in precipitate morphology with aging treatment observed in the study. The diameter of the disc shaped particles increases more drastically than the thickness due to the semi-coherent nature of the particles. Although TEM was performed on samples aged from 1 hour up to 1000 hours, the bulk of the precipitate characterization and diffraction

analysis was performed on samples aged longer than 100 hours. This is beyond observed peak age condition (25 hours), and may not fully represent the early stages of precipitation up to the peak aged condition.

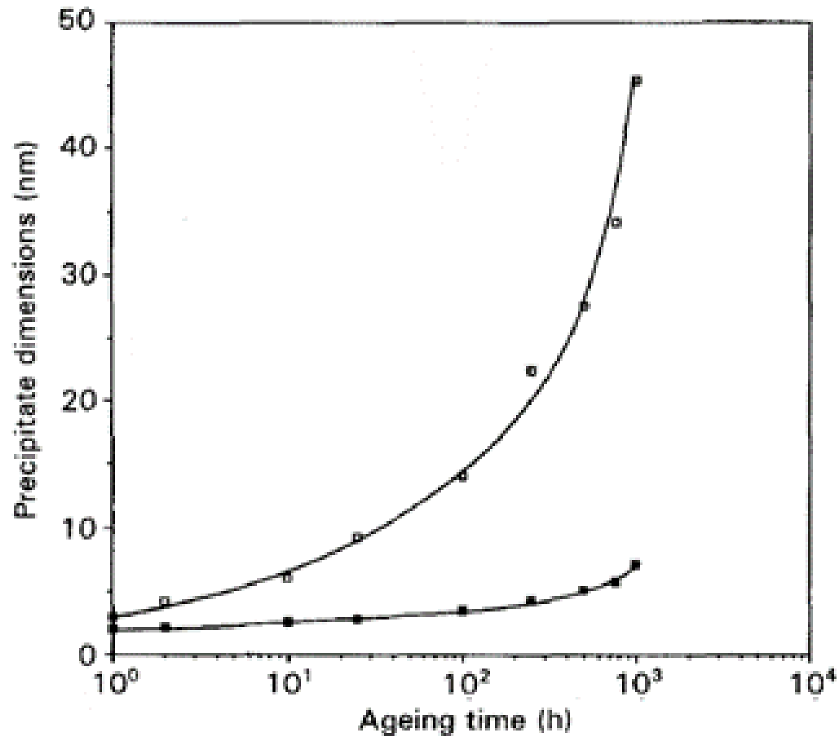

Figure 14. Variation in precipitate thickness (▪) and diameter (▫) during aging at 450°C for CuNiSi.[68]

With respect to mechanical properties, Lockyer and Noble found that the peak hardness of 197 HV occurred after 25 hours of aging at 450°C following a 2 hour solution treatment at 800°C. Ro`ughly comparing the observed particles at peak aging to the expected strengthening if Orowan looping was the mechanism yielded reasonable agreement. Additionally, the authors argued that due to the complexity of the precipitate crystal structure and its orientation relationship with the matrix, shearing of the particles would

be highly unlikely. The as-received material exhibited the highest yield strength due to prior cold work. Interestingly, the solution treated and 2 hour aged samples exhibited more dramatic work hardening behavior than any other condition. If particle cutting was predominant in the under-aged condition, then the increased work hardening would not result; however, if the particles could not be cut and Orowan strengthening was occurring, the predicted yield strength should be higher than the 25 hour age. Therefore, the authors hypothesized that the behavior may be due to a small amount of cutting active when the precipitates are small that is then limited by a buildup of dislocations at the interfaces of the particles leading to increased work hardening.[71]

In 2003, Zhao *et al.* performed TEM analysis of alloy C70250 (Cu-3.2Ni-.75Si) in the early stages of precipitation. [72, 73] Aging above a critical temperature resulted in discontinuous precipitation of δ-Ni_2Si which had a slightly lower strength than the sub-T_{cr} aging treatment. They suggest that below a critical aging temperature of 500°C, spinodal decomposition occurs prior to $(Cu,Ni)_3Si$ ordering (DO_{22} structure). Upon further aging, δ-Ni_2Si precipitates within the ordered $(Cu,Ni)_3Si$ regions. The eraly stage kinetics of precipitation are extremely rapid. At 450°C, the spinodal decomposition was estimated to occur after about 100-200 seconds at temperature, as evidenced by x-ray peak broadening and a plateau in the resistivity at this time followed by a sharp decrease in resistivity when the structure formed ordered

$(Cu,Ni)_3Si$ particles. A schematic free energy curve presented by the authors is shown in Figure 15 to describe the multi-step precipitation process. The author's state that at the peak age condition (10hrs at 450°C), the strengthening was only attributed to the Orowan mechanism (i.e. only from the δ-Ni_2Si and no contribution from any remaining $(Cu,Ni)_3Si$ ordered regions surrounding the particles). Indeed, the peak strength is similar for different aging temperatures (where the path to form the δ-Ni_2Si was proposed to be different) was the same, agreeing with Lockyer and Noble's earlier suggestions. Extensive direct observation and characterization of the early stages of silicide precipitation is limited in literature. Although the early stages of precipitation are complex and not well understood, literature is generally in agreement that in the peak age condition the Orowan mechanism is the main strengthening mechanism.

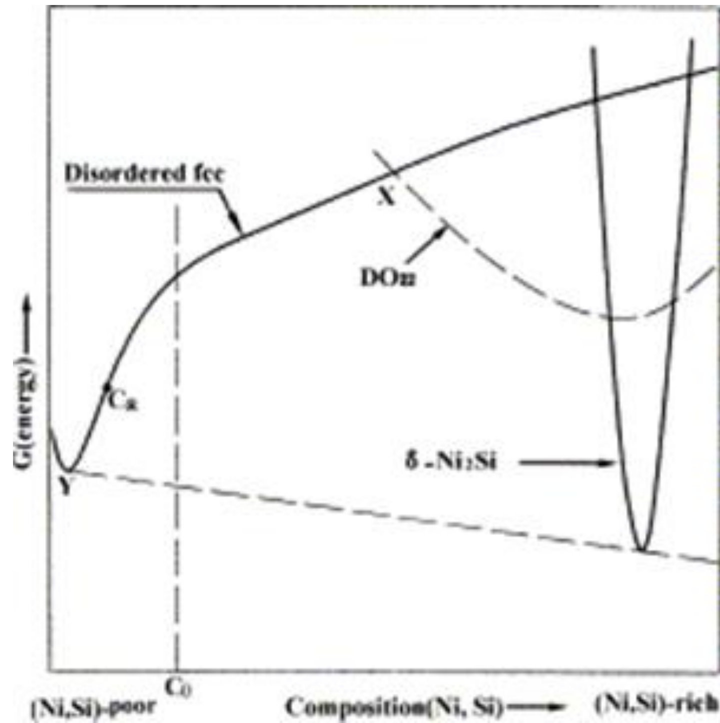

Figure 15. Schematic free energy curve at sub-critical aging temperatures for CuNiSi alloys proposed by Zhao et al. [73]

Despite a large portion of the literature indicating that δ-Ni_2Si was the strengthening phase, several investigations also have reported other silicide phases or suggested that a precursor phase may be the relevant hardening phase. More recently, Hu *et al.* has utilized high resolution TEM and atomic resolution scanning TEM (STEM) to determine the exact silicide phase that forms along with the orientation relationship of the silicides with the matrix throughout the later stages of aging.[74] The authors calculated the formation enthalpies of the possible silicide phases which indicated that δ-Ni_2Si is the most likely phase to form. After 10 minutes of aging at 450°C (the shortest aging time characterized), disc shaped δ-Ni_2Si precipitates approximately 3 nm long were in fact found. The peak age for the alloy studied was 100

minutes (~1.7 hours). Any precursor phases or regions that form prior to δ-Ni_2Si that were suggested in other studies therefore are not a significant factor near the peak age times. Well before and up to the peak age condition, the δ-Ni_2Si precipitates have the orientation relationship introduced by Lockyer and Noble. Beyond the peak age condition, after around 100 hours of aging, when the hardness has dropped to around 75% of the peak hardness the precipitates begin to rotate slightly. The over aged precipitates consist of slightly rotated δ-Ni_2Si and δ-Ni_2Si with a new orientation relationship and morphology. The changes in orientation relationship and morphology as precipitates grow serves to form a broad interface and minimize strain energy consistent with ideal rotation calculations based on the particle misfit along various planes of the copper matrix.[74]

In the peak aged condition the strengthening precipitates, δ-Ni_2Si, have a well-defined structure and orientation relationship with the copper matrix that has been confirmed by multiple studies and techniques. Additionally, literature is in agreement that in the peak age condition Orowan looping is the primary strengthening mechanism. However, amongst the CuNiSi alloys investigated that fall within or near the C70250 specification, the aging behavior at 450°C is highly variable in both peak age time and degree of over aging. CuNiSi alloys investigated in literature have peak age times at 450°C ranging from 1 to 40 hours. Some investigations indicate predictable and very stable logarithmic aging behavior (parabolic aging curves vs log aging time) in excess of 100

hours of aging time, while others experience rapid over aging beyond peak aging at much shorter times.[68, 71–73, 75–78] Additionally, discontinuous coarsening occurs in different amounts concurrently with continuous precipitate Ostwald ripening in literature investigations of CuNiSi alloys which is an established softening mechanism in precipitation hardening alloys.[79–82] The aging response of CuNiSi alloys appear to be extremely sensitive to changes in composition, starting microstructure, and/or processing history. This is of particular interest in relation to this investigation because of the unique processing characteristics of SLM.

CHAPTER 3

MECHANICAL PROPERTIES AND MICROSTRUCTURAL CHARACTERIZATION OF Cu-4.3%Sn FABRICATED BY SELECTIVE LASER MELTING

3.1 Abstract

Components were fabricated via selective laser melting of pre-alloyed Cu-4.3%Sn powder and heat treated at 873 K (600 °C) and 1173 K (900 °C) for 1 hour. Tensile testing, conductivity measurement, and detailed microstructural characterization was carried out on samples in the as-printed and heat treated conditions. Optimization of build parameters resulted in samples around 97% dense with a yield strength of 274 MPa, an electrical conductivity of 24.1 %IACS, and an elongation of 5.6%. Heat treatment resulted in lower yield strength with significant increases in ductility due to recrystallization and a decrease in dislocation density. Tensile sample geometry and surface finish also showed a significant effect on measured yield strength but a negligible change in measured ductility. Microstructural characterization indicated that grains primarily grow epitaxially with a sub-micron cellular solidification sub-structure. Nanometer scale tin dioxide particles identified via XRD were found throughout the structure in the tin rich intercellular regions.

3.2 Introduction

Selective Laser Melting (SLM) is an additive manufacturing technique based on powder bed fusion technology that can produce near fully dense metal components. In SLM, a laser guided by a computer model is used to fully melt metal powder on a build platform layer-by-layer until a fully functional component is produced. The key advantages of SLM include reduced development time, design freedom, and little material waste.[2] Copper alloys have seen extensive use with additive manufacturing as a binder or infiltrant, but rarely as a principle component to take advantage of their high conductivity properties.[19] Although some work exists on electron beam melting of commercially pure copper, there is relatively little available research on electrical grade copper alloy systems fabricated by SLM.[25, 26] Copper alloys have been difficult to process via SLM due to the poor laser absorption of copper, but increases in laser power in commercial SLM units present the opportunity to fabricate high density copper alloy components.[21, 83] Copper alloy components are of particular interest for electrical connector prototyping and fabrication of small production run components.

Numerous studies have been conducted on other metal alloys that demonstrate unique processing parameters inherent in SLM that affect microstructural characteristics and the resulting mechanical properties.[11, 32] Of particular importance is the high cooling rate, which can be up to 10^8 K/s.[28] As a result of this high cooling rate, there is a significant chance for

the formation of metastable phases and/or fine solidification substructure. For example, in Ti-6Al-4V, the resulting SLM microstructure is fine acicular martensitic.[29] Austenitic stainless steels such as 316L retain their austenitic structure, exhibiting solidification substructures with cell spacing on the order of 1 μm or less.[31] Additionally, intermetallic phases and non-metallic particles have been found at the melt pool boundary, occasionally serving as initiation sites for cracking and failure. These particles include those that normally occur in the alloy during solidification/segregation as well as defects retained from the source powder or the SLM processing atmosphere.[29, 36] Nearly all metallic alloys currently utilized in SLM exhibit epitaxial growth from the previous build layer resulting in elongated grains in the build direction. Titanium alloys, in particular, exhibit very large columnar prior β grain boundaries and conventional mill heat treatments do not produce optimum mechanical properties in SLM Ti-6Al-4V.[29, 38] Studies on Ti-6Al-4V have also found that columnar grains formed from epitaxial growth have preferred growth directions that can vary throughout the cross section of the sample, and the morphology can be altered with the addition of in-process deformation steps.[34, 37] Texture resulting from directional solidification can be tailored with scanning strategy as shown in an aluminum alloy as well as 316L stainless steel. Small changes in scanning complexity, for example rotating the laser scan between build layers, was found to be sufficient to suppress strong texture development.[23, 24]

Observations in literature of the microstructural features present in SLM components are inherently focused on the particular physical metallurgy of the alloy being investigated. The research available on SLM does not address mechanical properties or microstructural characteristics of common copper alloy systems. The objectives of this research are to develop an understanding of a SLM copper alloy including the relationship between microstructural characteristics and mechanical properties as they develop during post-processing heat treatment. A binary Cu-4.3%Sn alloy was selected for this study as a simple model system to understand the general response of copper alloys to SLM.

3.3 Experimental Methods

Pre-alloyed Cu-4.3%Sn gas-atomized powder was purchased from ECKA Granules with a maximum size of 63 μm. The powder was processed in an EOSINT M280 Direct Metal Laser Sintering (DMLS) unit with a 200 Watt Yb-fiber laser under a nitrogen atmosphere housed at TE Connectivity's Harrisburg, Pennsylvania facility. A preliminary investigation was performed to determine the optimum laser parameters for maximum printed density measured by the Archimedes technique. Components were built on top of a support structure from a steel baseplate and a standard raster scanning strategy with a 90° rotation between layers was employed. Along with the raster scanning, pre-contour and post-contour passes on the outer edge of each pass was completed. The interior volumes of the samples for this study

were fabricated with a laser power of 195 Watts, a scan speed of 390 mm/s, a beam spot size of 190 µm and a line spacing of 100 µm. The layer thickness was kept constant at 20 µm. The final density achieved with these settings was approximately 97% as measured by the Archimedes technique and confirmed by light optical porosity measurements. Any further changes that resulted in higher total energy input such as a finer laser spot or a slower scan speed did not improve density beyond this point. These laser parameters were used to fabricate 1 mm thick strip samples for conductivity measurement, all tensile samples, and 1 cm cubes for microstructural analysis.

Selected samples were post-fabrication heat treated at 873 K (600 °C) and 1173 K (900 °C) in a sealed tube furnace under an argon atmosphere. The samples were heated at a rate of 15 K/minute and held at the target temperature for 1 hour. After the heat treatment, the samples were air cooled. Tensile testing was conducted on ASTM E-8 sub-size rectangular specimens in the as-printed condition as well as CNC machined samples cut from over-printed rectangular prisms. The sub-size rectangular tensile test samples had an overall length of 100 mm with 10 mm wide grip sections and a reduced section 32 mm long by 6 mm wide. The filet radius between the grip section and reduced section was 6 mm. Uniaxial tensile tests were carried out on an Instron 5567 load frame with a 30-kN load cell and samples were gripped with serrated mechanical wedge grips. Strain was determined by digital image correlation in conjunction with Bluehill 3 software and an Instron AVE2 video

extensometer. Tensile specimens were loaded perpendicular to the build axis. Three samples of each condition were tested and an average was taken for mechanical property reporting. The yield strength was calculated using the 0.2% offset method and the elongation was taken as the strain at failure. Resistivity measurements were taken on 1x1x60 mm^3 Cu-4.3%Sn strips (machined from larger printed sheets) using a 4-wire method on a Keithley 580 Micro-Ohmeter. Four samples were measured for each condition and averaged to determine the conductivity as a percentage of the International Annealed Copper Standard (%IACS) based on the resistivity of pure annealed copper (172.41 $\mu\Omega$ - cm).[16]

Printed cubes were sectioned using a Struers Accutom-50 high speed abrasive cutoff wheel and mounted in cold-setting epoxy. Metallographic specimens were prepared using standard preparation techniques with a final attack polish (1% ammonium hydroxide, 1% hydrogen peroxide and 98% 0.05 µm colloidal silica) for light optical microscopy on a Reichart-Jung MeF3 optical microscope. Digital images were captured with a Nikon DxRi-1 camera and NIS Elements D software. Samples were etched in Klemm’s I reagent. Vickers microhardness measurements were taken on etched metallographic samples with a Leco LM248AT using a load of 25 g. Electron backscatter diffraction (EBSD) was conducted on polished metallographic samples in a Hitachi 4300 field-emission scanning electron microscope (FE-SEM). EBSD analysis was completed using TSL OIM analysis software and the data was

cleaned using grain dilation with a maximum of 9% of the collected points changed. A JEOL JXA 8900R Electron Probe Microanalyser (EPMA) was used to perform wavelength-dispersive spectroscopy (WDS) analysis. Electron transparent specimens for (scanning) transmission electron microscope ((S)TEM) characterization were prepared by an FEI SCIOS Focused Ion-Beam (FIB) instrument and were gently cleaned by using a Fischione 1040 Nanomill at 900 eV. TEM/STEM analysis including X-ray Energy Dispersive Spectrometry (XEDS) was completed using a JEOL JEM-ARM200CF aberration-corrected STEM. As-printed strip samples polished to 1 μm using standard metallographic preparation techniques were used for X-ray Diffraction (XRD). XRD was completed on a PANalytical Empyrean unit with a Cu tube operating at 45 kV and 40 mA using Bragg-Brentano geometry. A θ:θ scan was done for 2θ angles from 20° to 100° with a step size of .013° using a PIXcel3D-Medipix3 area detector in scanning line detector mode. Phi was varied from -30° to +30° to reduce any possible orientation effects, although no significant difference in the intensity of peaks between scans was observed. Peaks were identified using PDXL software and the ICDD PDF-2 database.

3.4 Results

Prior to testing, tensile specimens were heat treated at 873 K (600 °C) and 1173 K (900 °C) for 1 hour. The lower temperature heat treatment represents a standard annealing heat treatment for typical bronze alloys.[16]

The higher temperature heat treatment was chosen as a severe condition to induce significant microstructural change. Figure 16 shows the uniaxial tensile test results of 3 mm thick SLM Cu-4.3%Sn in the as-printed condition as well as with the two heat treatments. All samples in Figure 16 were tested with the printed surface condition (i.e. tensile bars were printed with dimensions that match ASTM E-8 sub-size samples and tested with no alteration to the surface condition except removal of the support structure on one side).

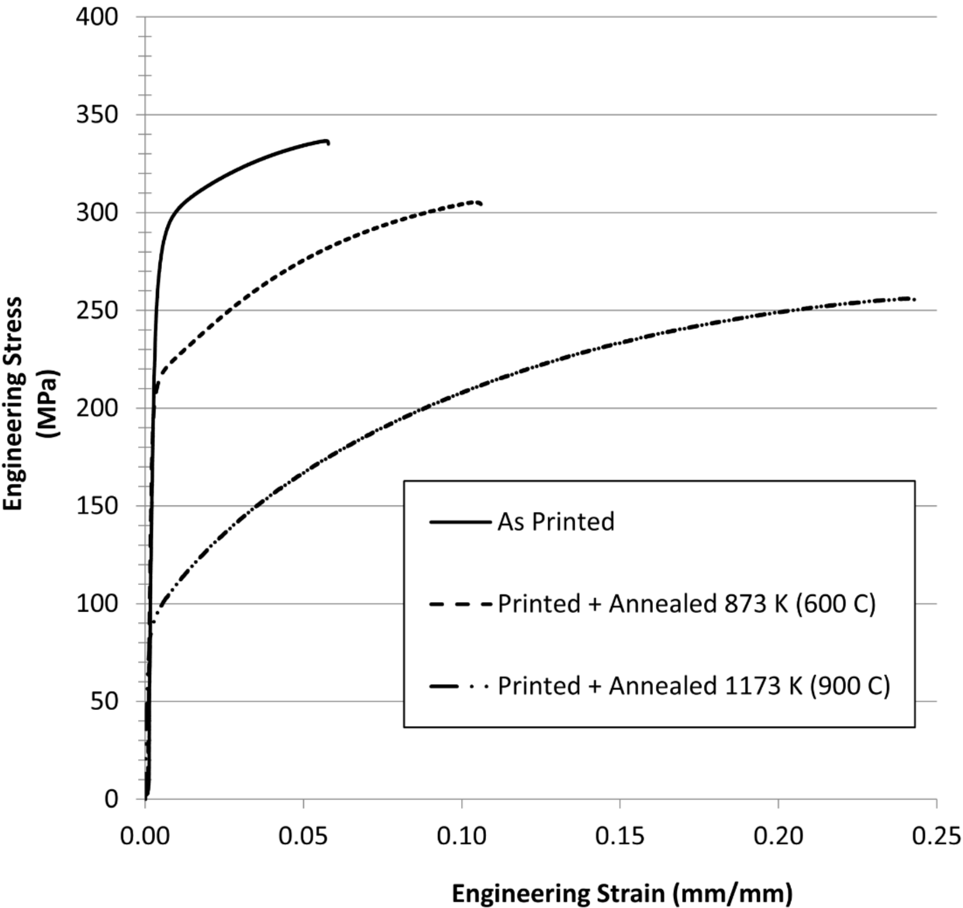

Figure 16. Prototypical uniaxial tensile test results of SLM Cu-4.3%Sn in the as-printed condition as well as post-process heat treated at 873 K (600 °C) and 1173 K (900 °C).

The physical properties of the SLM Cu-4.3%Sn are shown in Table 2. The yield strength of the as-printed material is the highest with a value of 274 MPa. The heat treated samples have lower yield strength values inversely related to the heat treatment temperature. The 873 K (600 °C) and 1173 K (900 °C) heat treated samples have yield strengths of 208 MPa and 102 MPa, respectively. Table 2 shows that the ultimate tensile strength values follow a similar trend. Ductility is the lowest in the as-printed sample at an elongation of 5.6%. Ductility increases with heat treatment temperature with values of 12.4% and 26.1% for the low and high temperature heat treatments, respectively. Although the total elongation has significant changes between the sample conditions, none of the samples exhibit any significant localized ductility after the ultimate tensile strength is reached. Conductivity measurements (Table I) show that the as-printed condition has the highest conductivity of 24.1 %IACS while the two heat treated samples have similar conductivity values around 21 %IACS. These values are in good agreement with wrought bronze alloys available commercially with similar tin concentrations.[16]

Table 2. Physical Properties of SLM Cu-4.3%Sn in the As-Printed and Post-Process Heat Treated Conditions

Sample	Yield Strength (MPa)	Ultimate Tensile Strength (MPa)	Elongation at Failure (%)	Conductivity (%IACS)
As Printed	274	334	5.6%	24.1%
Printed + Annealed 873 K (600 °C)	208	309	12.4%	21.2%
Printed + Annealed 1173 K (900 °C)	102	267	26.1%	21.0%

Figure 17 shows a light optical micrograph of the build direction of as-printed Cu-4.3%Sn. Individual weld pools from the SLM process can be seen running horizontally in Figure 17. Grains are elongated along the build direction although their shape is highly varied. The grains also appear to stretch through multiple build layers. EPMA mapping showed a generally homogeneous distribution of tin throughout the material, with slight variations at the weld lines.

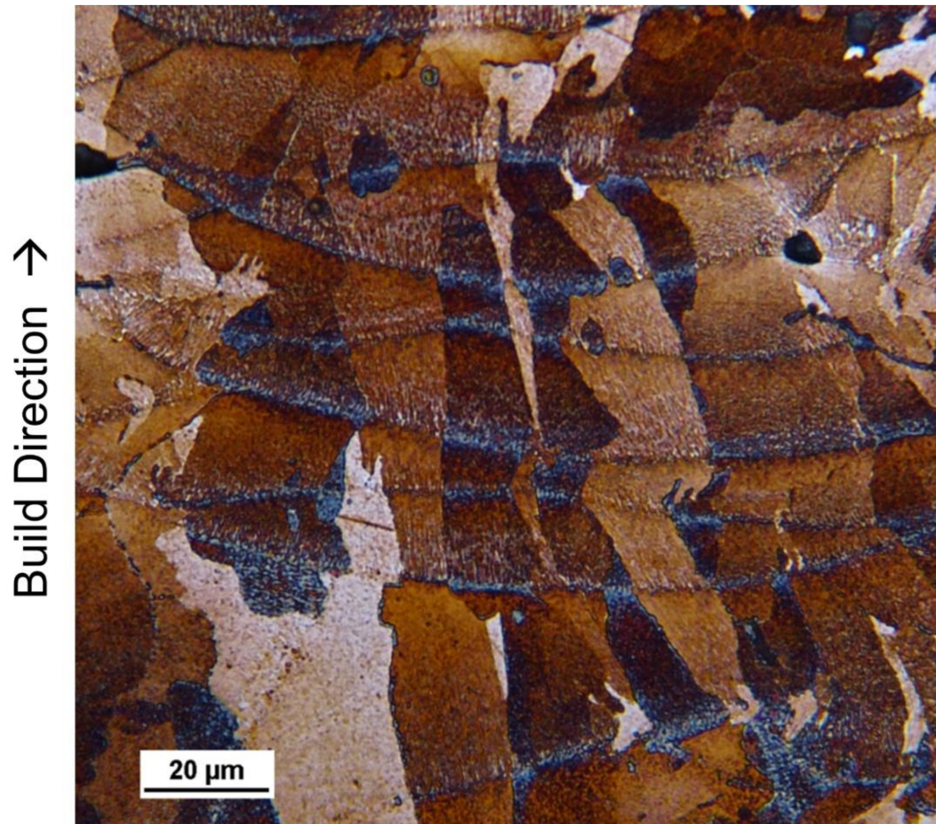

Figure 17. Light optical micrograph of the build direction of as-printed Cu-4.3%Sn etched in Klemm's I reagent.

Figure 18 shows inverse pole figure (IPF) maps for SLM Cu-4.3%Sn in the as-printed and heat treated conditions, obtained by EBSD. The maps more clearly show the elongated grain structure that was observed in Figure 17. In the as-printed condition, abnormally large grains as well as very fine grains can be found. However, most grains regardless of size tend to be elongated along the build direction. After the 873 K (600 °C) heat treatment there is little change in the grain morphology. After heat treatment at 1173 K (900 °C) the grain morphology has changed significantly as shown in Figure 18 (c). Grains

are approximately equiaxed and contain annealing twins. Additionally, they are larger on average than in the other two conditions.

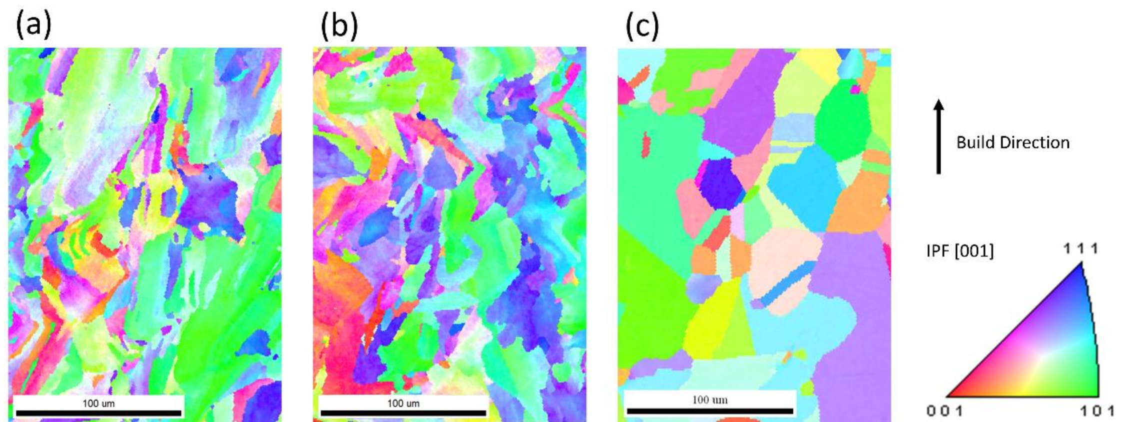

Figure 18. IPF Maps of SLM Cu-4.3%Sn in the (a) as-printed condition, and after heat treatment at (b) 873 K (600 °C) and (c) 1173 K (900 °C).

Figure 19 shows Annular Bright-Field (ABF) STEM images of SLM Cu-4.3%Sn in the as-printed and two heat treated conditions. The images show a high dislocation density in the as-printed condition as well as a moderate dislocation density in the printed and heat treated at 873 K (600 °C) sample. In contrast, the sample that underwent a heat treatment at 1173 K (900 °C) does not show an appreciable number of dislocations.

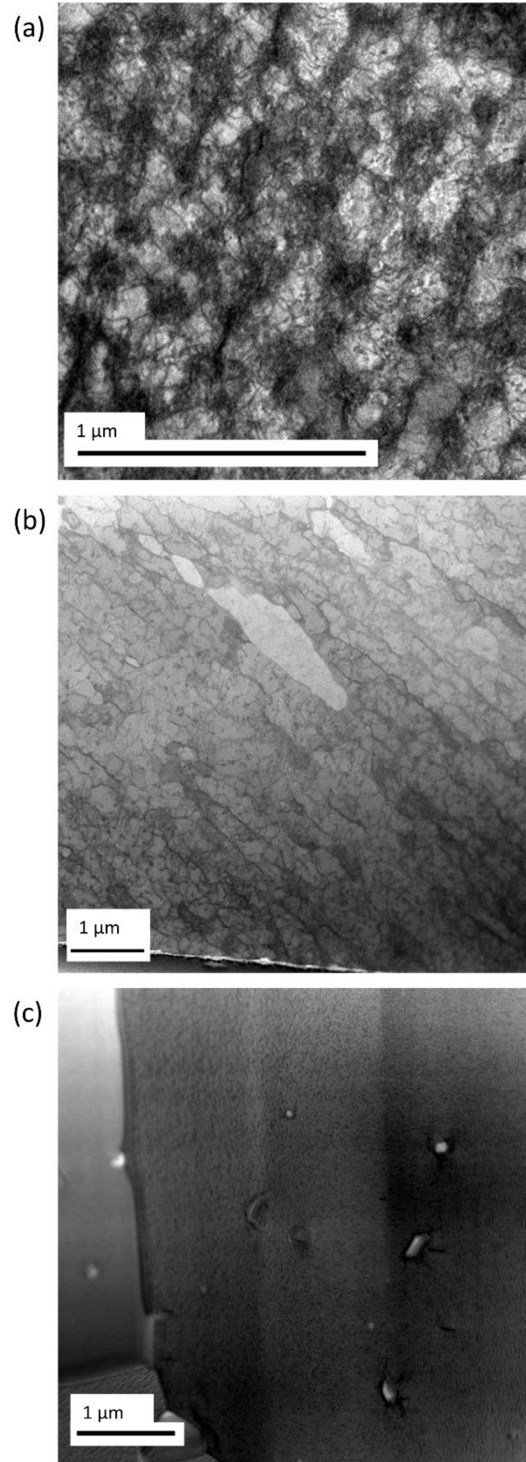

Figure 19. ABF STEM microstructural comparison between SLM Cu4.3%Sn in the (a) as-printed condition as well as printed and heat treated at (b) 873 K (600 °C) and (c) 1173 K (900 °C).

3.5 Discussion

3.5.1 Grain Morphology

The grain morphology observed in completed components is quite complex. Figure 17 shows many grains that extend through multiple build layers. In the bulk of the components (i.e. away from the initial layers of the build), the molten metal is solidifying on top of previously solidified material of the same composition. As a result, there is complete wettability and the underlying layer acts as a nucleation site for solidification leading to epitaxial growth from lower layers similar to that commonly observed in autogenous welding and has been observed in SLM of other alloys.[24, 29, 33, 34] In this experiment, there is a rotation of the laser scan direction between passes as well as the significant overlap and re-melting in the build plane and between layers expected based on the build parameters. The direction of columnar growth is not entirely consistent throughout the material as the direction of maximum heat extraction is changing slightly during scanning in each individual weld pool. This is particularly noticeable in Figure 17 when grains change solidification direction abruptly along another (100) fast solidification direction at the weld line. However, the grains are all generally aligned along the build axis to a certain degree as it is the common primary solidification direction. Although many grains clearly appear to have solidified epitaxially, it is also likely that heterogeneous nucleation mechanisms are active. There are a number of possible nucleation sites including but not limited to partially-

melted adjacent powder particles, contamination in the weld pool (e.g. oxide particles) and free surfaces. The significant amount of re-melting makes it difficult to individually identify the secondary grain nucleation mechanisms, and epitaxial growth appears to be the dominant solidification mechanism. During solidification, competitive growth takes place causing some grains to grow significantly larger and extend through multiple build layers while other grains are very fine, as shown in Figure 17 and Figure 18.

Given the significant amount of re-melting leading to epitaxial solidification and columnar grains, it is possible some texture would develop along the build direction. Figure 20 shows the EBSD IPFs taken from the transverse direction (IPFs are parallel to the build direction) of SLM Cu-4.3%Sn in the as-printed and two heat treated conditions. No significant texture was confirmed along the build direction in any of the sample conditions. Rotation of the laser-scanning direction appears to change the solidification conditions enough between different laser scans to inhibit a strong texture from developing. Similar observations have been reported in aluminum alloys.[29] However, the fields scanned to create these pole figures were held constant at 150 μm by 150 μm leading to insufficient statistics to make definitive claims about the bulk texture of SLM Cu-4.3%Sn. A more detailed X-ray texture analysis is needed to fully understand the bulk texture of these samples.

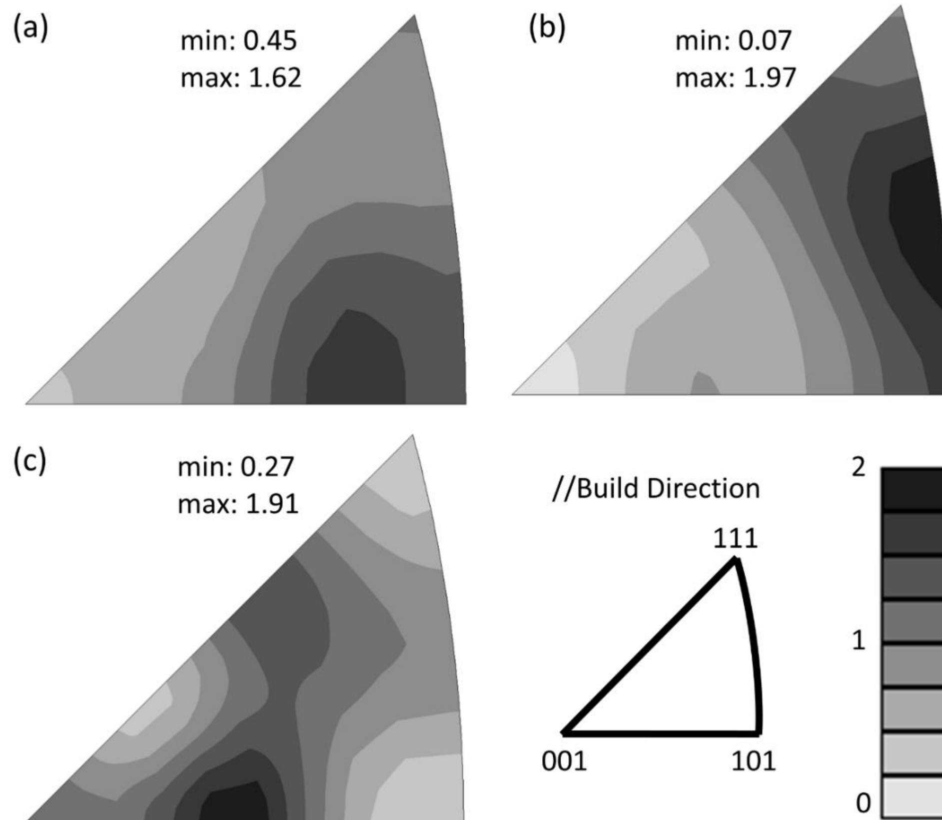

Figure 20. Inverse pole figures taken from the transverse direction (parallel to the build direction) of SLM Cu-4.3%Sn in the (a) as-printed condition as well as heat treatment at (b) 873 K (600 °C) and (c) 1173 K (900 °C).

3.5.2 Effect of Geometry on Tensile Properties

From a practical standpoint, it is useful to know if the mechanical properties measured in Figure 16 will be representative of small scale electrical components fabricated from copper alloys via SLM. Figure 21 shows the uniaxial tensile testing results for samples tested under different surface and geometry conditions. The curve of as-printed 3 mm thick sample shown in Figure 21 corresponds to the as-printed curve in Figure 16 with a yield strength of 274 MPa. There are marked changes in yield strength and ultimate tensile strength based on the thickness of the tensile specimen as well as the

surface conditions. The measured yield strength is the highest of 301 MPa for the case of a machined 3mm thick sub-size tensile sample. The sample was machined down from a rectangular prism blank that was printed with a minimum of 1 mm of excess material on all sides. Additionally, samples in the as-printed condition with the same sub-size geometry but a thickness of 1 mm have the lowest yield strength of 211 MPa. Using the 3 mm thick as-printed condition as a baseline, there is a change of approximately +10% and -23% for the machined and 1 mm thick as-printed samples, respectively.

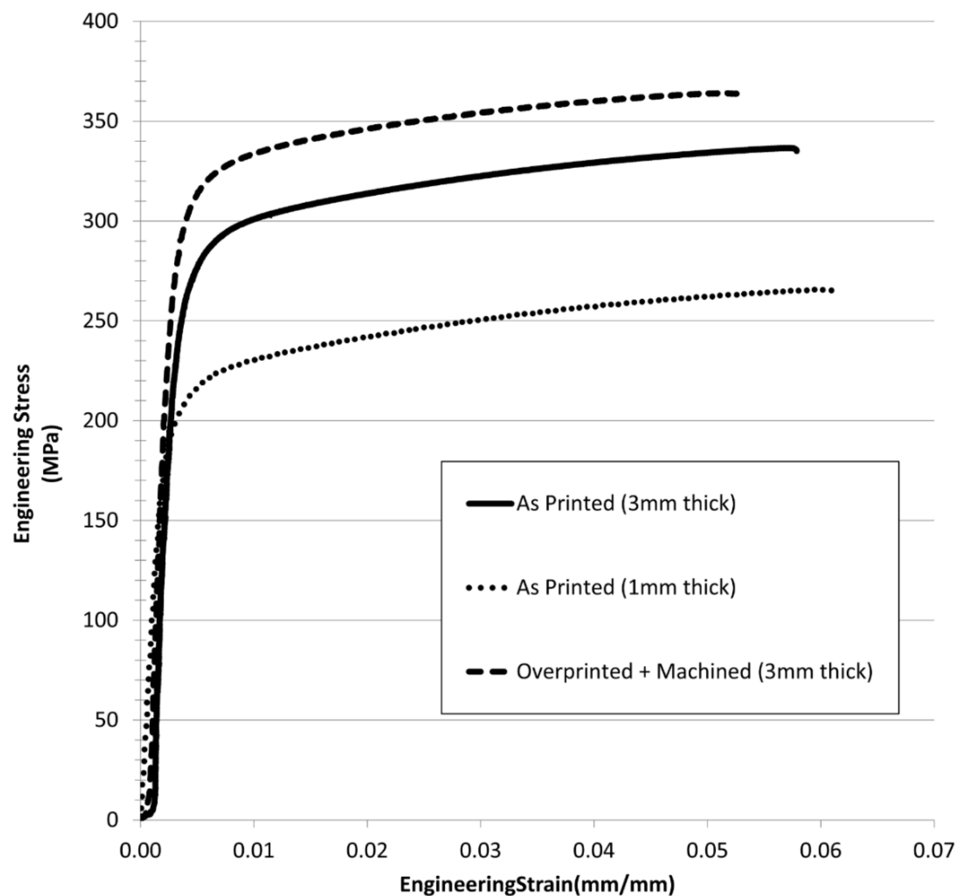

Figure 21. Prototypical uniaxial tensile test results of SLM Cu-4.3%Sn in the as-printed condition 3mm thick, 1mm thick and a sample that was machined from a rectangular prism to 3mm thick.

Several studies have been conducted to investigate size effects during tensile testing as they pertain to making small components. In traditional wrought microstructures during tensile testing, there is a general trend of decreasing strength as thickness decreases. This phenomenon is explained by the relationship of the grain size and the thickness of the specimens as well as the increased relative contribution from imperfections. As the number of grains spanning the cross section of the tensile specimen decreases, eventually a significant portion of the grains are not constrained by surrounding material as is the case in thicker polycrystalline samples leading to lower overall strength.[84] The critical thickness versus grain size varies for individual testing conditions. Work on aluminum and copper alloys have shown that for sheet with grain sizes on the order of 50 μm, the critical sheet thickness where the trend becomes noticeable is less than 1 mm.[84, 85] Although it is difficult to directly apply this theory to the SLM structures observed in this study due to the unique grain morphology, observing the grain sizes from Figure 18 (a) combined with a minimum specimen thickness of 1 mm suggests that the contribution of this mechanism is insignificant. This is further supported by the negligible change in ductility in Figure 21 which does not align with findings from wrought structures where the grain size/thickness effect was found to be active. Similarly, the effect of surface roughness was found to be relatively insignificant in literature, particularly on samples thicker than 1 mm.[85]

Given the presence of porosity, oxide inclusions, and irregular grain morphology, the relative imperfection contribution is more likely to have a significant effect on the tensile properties of SLM materials. Of particular interest is porosity that tends to concentrate at the interface of the raster scan and the contours of the outside surface of the parts which has been observed in this study approximately 50-100 μm from the surface. In the samples machined from a larger blank, this porosity band would be removed. In contrast, this porosity band would be more significant (i.e. have a larger contribution related to the cross section of the gauge length) in the 1 mm thick as-printed samples. As a result, there is a significant variation in tensile properties reflected in Figure 21 based on sample condition and this must be accounted for in component design.

3.5.3 Effect of Heat Treatment on Tensile Properties

Figure 16 established the mechanical property dependence on heat treatment for SLM Cu-4.3%Sn for samples in the as-printed condition (no surface finishing) with a thickness of 3 mm. For electrical connectors, typically the highest yield strength is desired to elastically store energy thereby holding spring force in use. In the absence of required post-SLM forming operations (e.g. bending to final part geometry), the ideal condition for use would be the as-printed condition. Regardless, heat treatment has a significant effect on both the strength and ductility of SLM Cu-4.3%Sn.

Comparing the grain morphology in Figure 18 between the as-printed and 873 K (600 °C) heat treated conditions indicates that there is no significant change between the two conditions. This implies that grain growth and the Hall-Petch relationship are not the dominant factor in the change in mechanical properties of the two conditions. Figure 19 (a) shows a TEM image of the as-printed sample with a high dislocation density substructure. Although there is no deformation in the classical sense associated with the SLM process, significant thermal gradients and repeated heating and cooling cycles cause significant residual stresses.[8, 39] As a result, the observed high dislocation density structure occurs giving the as-printed condition the highest yield strength of the tested conditions. Additionally, the as-printed sample has a less pronounced strain hardening effect than the 873 K (600 °C) heat treated sample. Despite the 873 K (600 °C) heat treatment being typical for wrought alloys of this type, recrystallization has apparently not occurred after 1 hour at this temperature. Figure 19 (b) shows qualitatively that the 873 K (600 °C) heat treated sample still has a significant number of dislocations present in the structure though less than in the as-printed condition. These observations combined with the tensile properties of the 873 K (600 °C) heat treated sample suggest that some recovery has taken place and recrystallization may be occurring in discrete locations in the sample. Figure 22 shows a differential interference contrast light optical micrograph of the build direction of the 873 K (600 °C) heat treated sample. Grains exemplifying the structure observed in

Figure 18 (b) can be found on the left half of the image, while a colony of equiaxed grains can be found on the right half. Microhardness measurements taken from 6 different fields show that the equiaxed grain colonies have an average hardness of 84 HV compared to an average of 123 HV for the surrounding grains that have similar morphology to the as-printed material. The equiaxed nature of the grains, the presence of annealing twins, as well as the lower microhardness measurements from the grains indicate that they formed from recrystallization. The observed significant decrease in strength is not expected from a low stacking fault energy material like bronze from recovery processes alone, which supports the hypothesis that the 873 K (600 °C) heat treated sample underwent the initial stages of recrystallization.[86] The decreased number of dislocations in the sample and the discrete areas that have undergone recrystallization result in a lower yield strength and accompanying increase in ductility and strain hardening response.

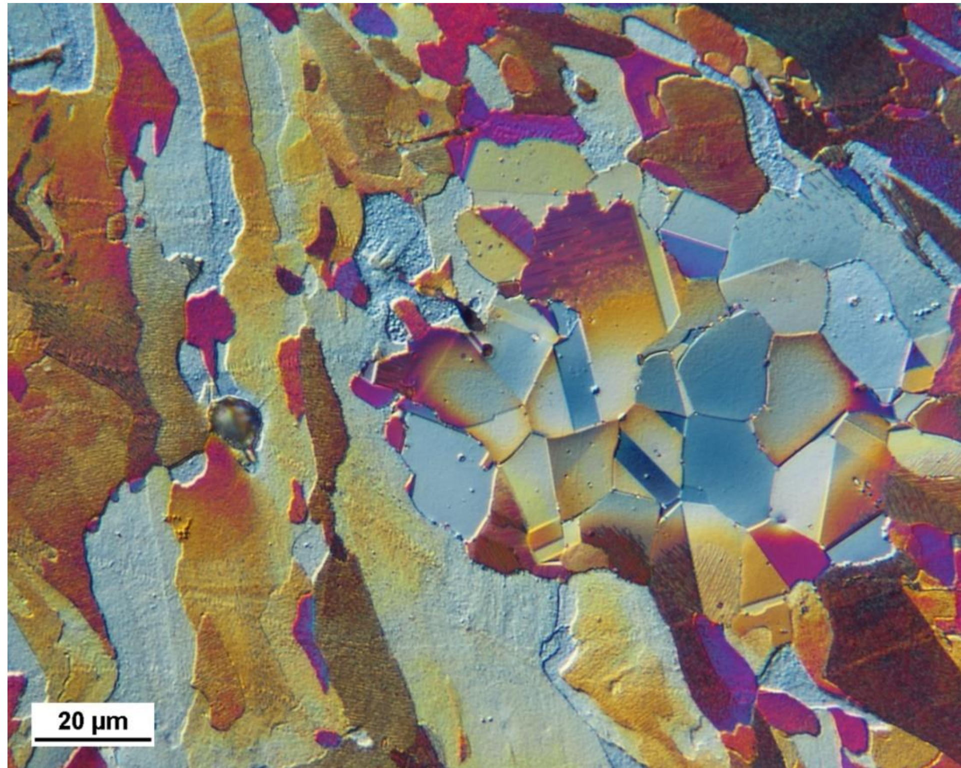

Figure 22. Differential interference contrast light optical micrograph of the build direction of SLM Cu-4.3%Sn heat treated at 873 K (600 °C) etched in Klemm's I reagent.

The 1173 K (900 °C) heat treated samples have completed the recovery and recrystallization process. EBSD shows an equiaxed grain structure with a generally unimodal size distribution. Annealing twins can also be seen clearly within the grains. The structure would be expected to have a low dislocation density and the lowest strength of the sample conditions in this experiment. The structure is relatively dislocation free as seen in Figure 19 (c). With a larger grain size than the as-printed or 873 K (600 °C) heat treated condition and a less dense network of dislocations, dislocation motion is not significantly impeded. The strength of this structure will be lower than the high dislocation density of the as-printed condition. The relatively large grained, low

dislocation density structure of the 1173 K (900 °C) heat treat sample has the lowest yield strength, highest ductility, and most dramatic strain hardening effect as shown in Figure 16.

The overview of the mechanical properties in this study in Table 2 shows a wide range of attainable properties for SLM Cu-4.3%Sn. In relation to the mechanical properties, one of the largest effects of heat treatment is from alteration of the dislocation density in the material by way of recovery and recrystallization. The results indicate that heat treatments can be tailored to achieve desired properties, but the highest strength condition, in the case of the single phase Cu-4.3%Sn alloy used in this study, is in the as-printed condition.

3.5.4 High Magnification STEM and EDS

Weld lines characteristic of the SLM process can be clearly seen in Figure 17. Although weld lines could be resolved in the light optical images, EPMA compositional analysis did not indicate detailed inhomogeneity within the weld pools. The solidification substructure is apparently too fine to be resolved using light optical microscopy or EPMA. To examine the solidification substructure as well as the transition zone at the weld line, an electron transparent TEM specimen was extracted from a single grain across a weld line using a FIB instrument. This area of interest along the build direction of SLM Cu-4.3%Sn is shown in Figure 23. Areas rich in tin, verified via XEDS, are observed with a cellular morphology. Interestingly, the cell spacing

appears to decrease as distance from the weld line increases. The findings are in agreement with the type of substructures found in SLM aluminum alloys.[24]

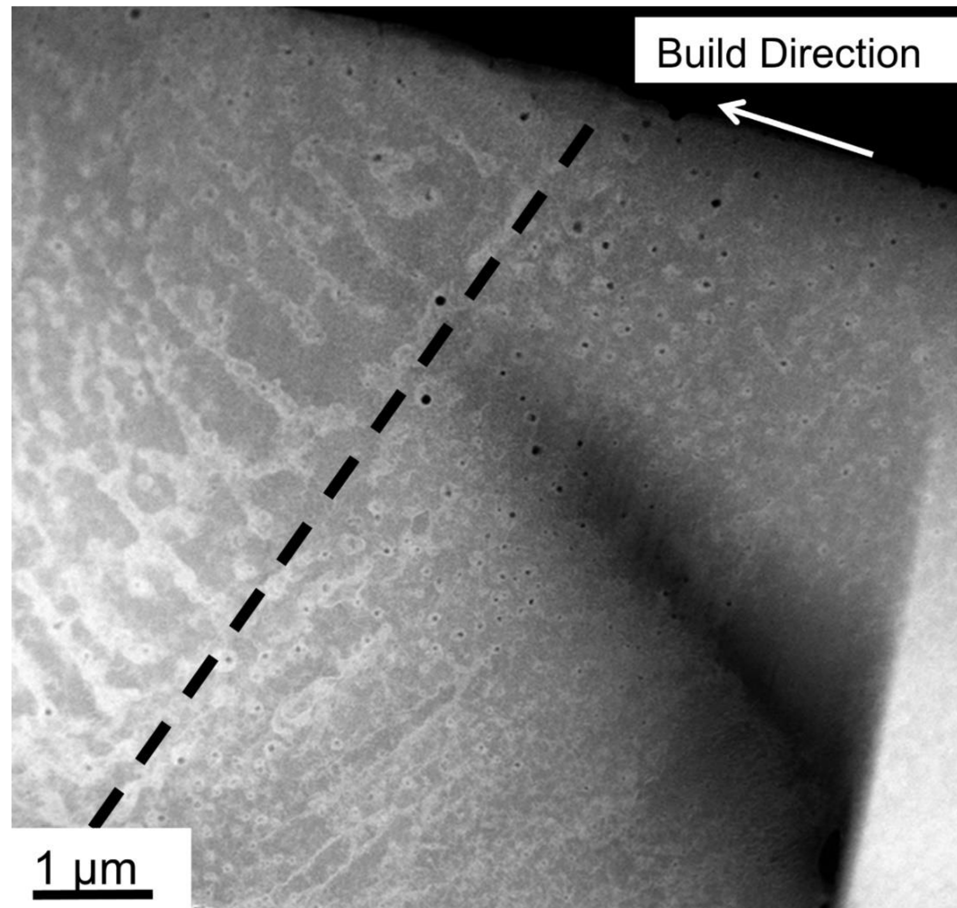

Figure 23. ABF STEM image along the build direction of as-printed SLM Cu-4.3%Sn showing an individual weld line (dashed line) and solidification sub-structure.

Figure 23 also shows particles (dark spots) in the intercellular region. Based on the alloy composition, the microstructure is expected to be a single phase face-centered cubic solid solution with no second phase particles. Figure 24 shows a high magnification Bright-field (BF) STEM image of one of the particles from the as-printed condition along with XEDS intensity maps of

copper, oxygen and tin. The particles show a high intensity of tin and oxygen compared to the surrounding matrix phase. There is negligible copper intensity within the particle, indicating that the particles are some type of tin oxide, likely due to the relatively high affinity of tin to form tin oxide compared to copper.[87]

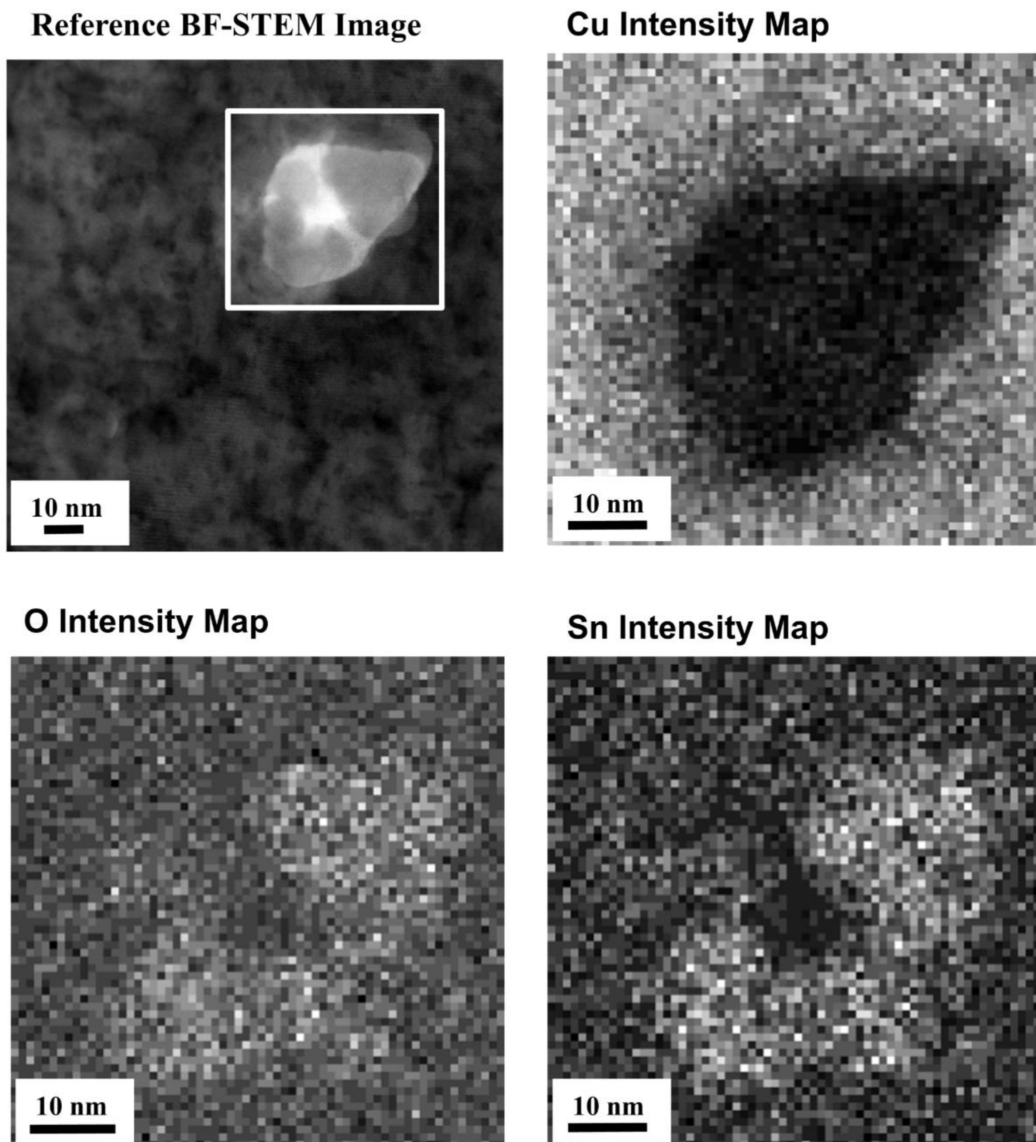

Figure 24. BF- STEM and accompanying XEDS intensity maps of typical small particles observed in the intercellular regions of the as-printed Cu-4.3%Sn.

Figure 25 shows XRD results of the as-printed SLM Cu-4.3%Sn. Peaks from the FCC copper matrix (with tin in solid solution) are identified along with peaks corresponding to the oxide particles which indicate that the particles are SnO_2. The particles are approximately 40-60 nm in diameter and homogeneously distributed through the specimen on a large scale, although they are typically confined to the intercellular regions locally. The particles are likely introduced from oxide on the surface of the precursor powder given the low oxygen build atmosphere that is flushed with argon in the EOSINT M280 used for this experiment. During solidification, tin and oxygen that are dissolved in the copper are expected to be segregated into the intercellular regions simultaneously due to constitutional supercooling. Upon reaching a critical temperature, the SnO_2 is expected to form during solidification.

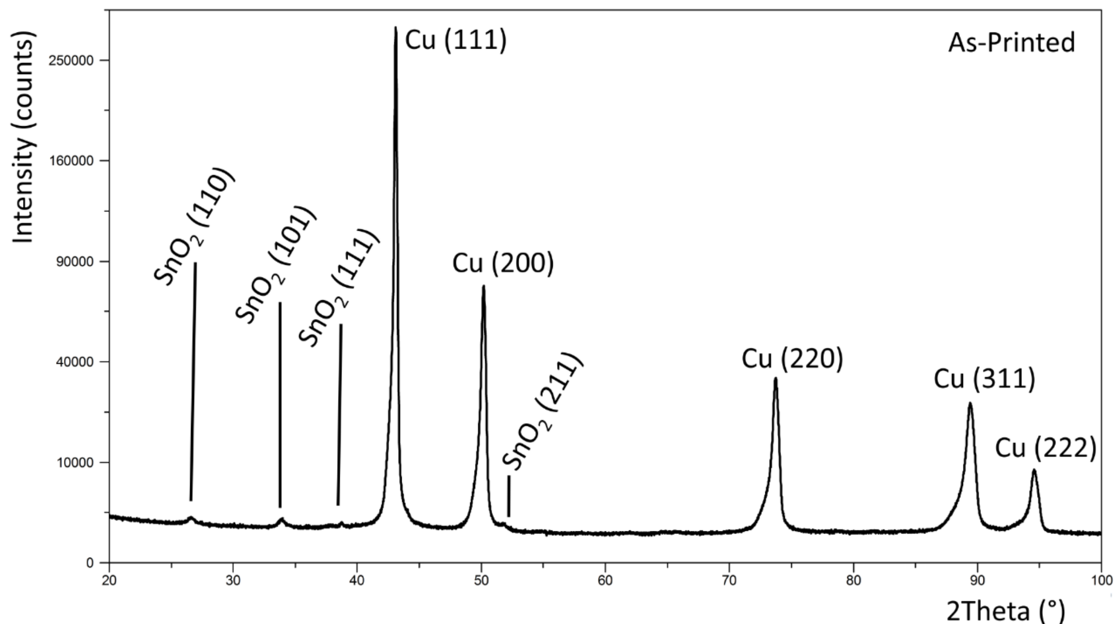

Figure 25. XRD pattern obtained from as printed SLM Cu-4.3%Sn.

After heat treatment at 873 K (600 °C) the oxide particles do not have a significant change in morphology. Although evidence of the cellular substructure is eliminated, the size and distribution of the oxide particles does not noticeably change as shown in Figure 26. The oxide particles are small enough to interact with dislocations in the as-printed and 873 K (600 °C) heat treated sample, suggesting that they may be acting as strengthening particles as in oxide dispersive strengthened alloys. Additionally, the oxide particles may be interfering with recovery and recrystallization thereby explaining the limited response of the material to the 873 K (600 °C) heat treatment. Due to the significant microstructural changes during heat treatment of the samples in this study, a definitive contribution to strength from the oxide particles could not be established.

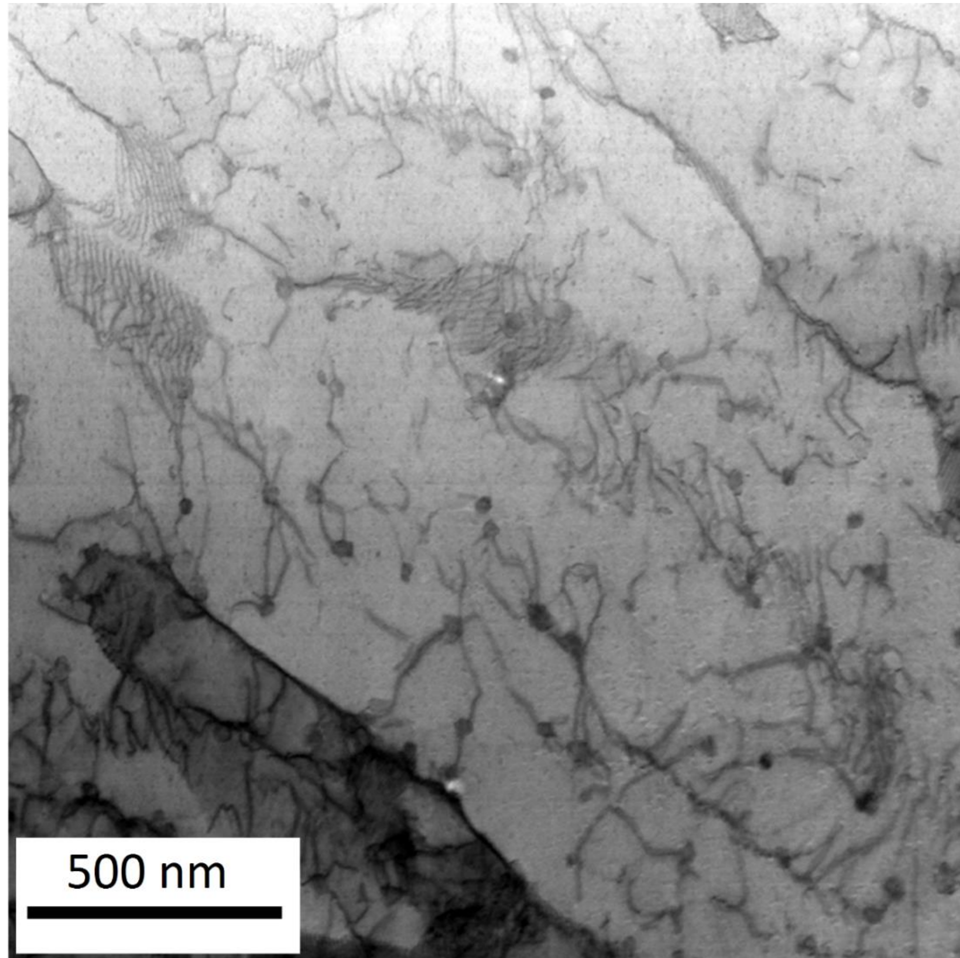

Figure 26. ABF-STEM image of oxide particles (dark spots) observed in SLM Cu-4.3%Sn heat treated at 873 K (600 °C).

After heat treatment at 1173 K (900 °C), the oxide particles have coarsened significantly to sizes that are unlikely to significantly enhance strength as seen in Figure 27. There is a wide range of particle sizes in the 1173 K (900 °C) heat treated sample, with particularly large particles along grain boundaries and at triple points. The oxide coarsening is consistent with an Ostwald ripening mechanism wherein small particles are sacrificially

dissolved as large particles grow. Particles on boundaries grow larger due to the enhanced diffusion along grain boundaries.[62]

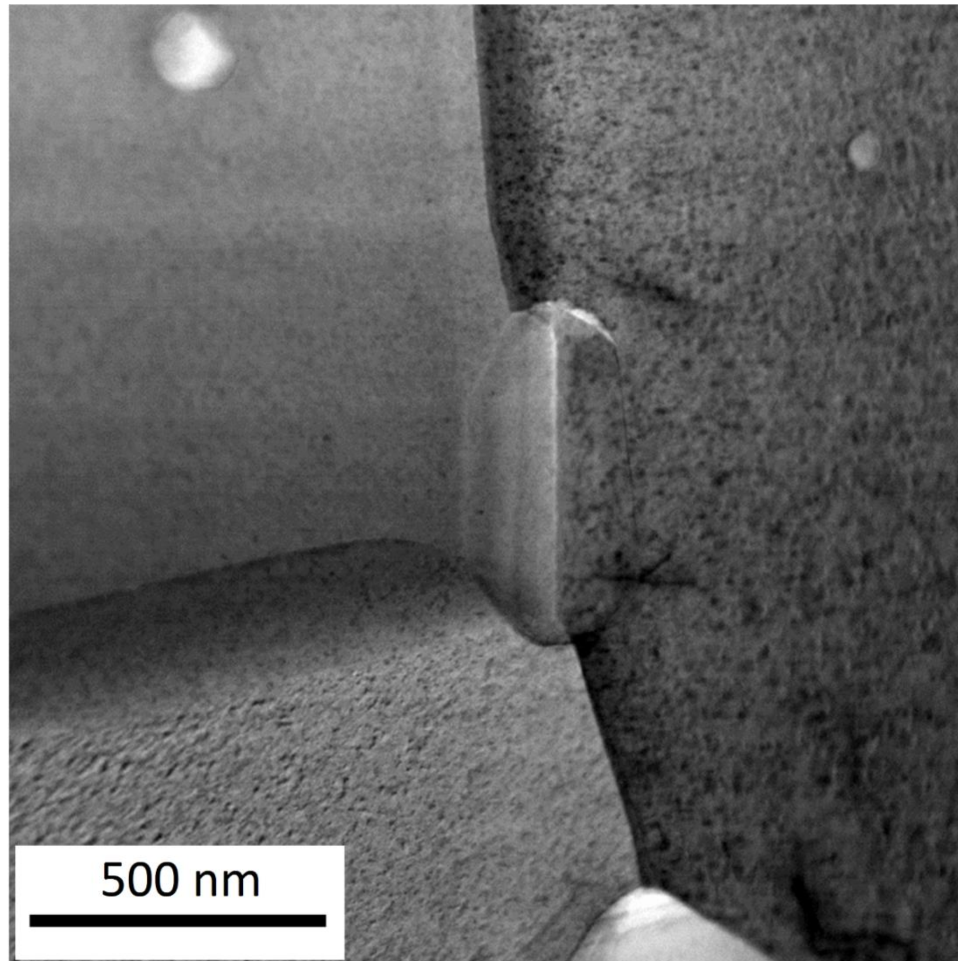

Figure 27. BF-STEM image of oxide particles observed in SLM Cu-4.3%Sn heat treated at 1173 K (900 °C).

Based on the qualitative observations of dislocation density from TEM analysis the conductivity would be expected to increase with heat treatment.[16] However, conductivity was highest in the as-printed condition. The changes in conductivity between the sample conditions described in Table 2 are likely a result of the oxide particle coarsening process. During heat

treatment, tin and oxygen atoms from smaller particles are dissolved back into the matrix and diffuse along a concentration gradient between particles of different sizes resulting from the Gibbs-Thomson effect.[62] Although the larger particles are growing, the local solute concentration in the matrix increases in relation to the as-printed condition because of the sacrificial dissolution of smaller particles. Solute atoms in the matrix have a significant effect on the conductivity of copper alloys, resulting in a decrease in conductivity which outweighs the contribution from a lower dislocation density structure.[16] In other words, solute atoms (oxygen and tin in this case) are more influential than lowering the dislocation density thereby degrading the conductivity.

3.6 Conclusions

The mechanical properties of selective laser melted Cu-4.3%Sn during post-processing heat treatment were investigated in conjunction with microstructural characterization. Samples were fabricated for analysis in the as-printed condition as well as heat treated at 873 K (600 °C) and 1173 K (900 °C). Uniaxial tensile tests and electron microscopy techniques were utilized to characterize the resultant microstructure and properties of each condition. The following conclusions were reached as a result of this work pertaining to selective laser melting Cu-4.3%Sn:

1. Optimization of build parameters, namely the laser power and beam focus, resulted in part densities around 97%. The primary grain

growth mechanism is epitaxial growth and there is a cellular solidification sub-structure with sub-micron spacing.

2. The as-printed condition has the highest yield strength and conductivity measured (274 MPa, 24.1 %IACS) but the lowest ductility (5.6% elongation)
3. Heat treatment reduces the yield strength and increases the ductility markedly primarily as a result of recrystallization and a decrease in dislocation density.
4. Tensile sample geometry and surface finish have a significant effect on the measured tensile properties and must be taken into account during design and processing.
5. High resolution STEM analysis reveals nanometer scale tin dioxide particles throughout the structure in the tin rich intercellular regions.

3.7 Acknowledgements

The authors would like to thank TE Connectivity, ltd. for the partial funding of this research along with collaboration throughout the study. The authors thank the Loewy Family Foundation for financially supporting this project and two of the authors, (Anthony P. Ventura) as a Loewy Graduate Fellow and (Wojciech Z. Misiolek) through the Loewy Professorship at Lehigh University.

This material is based on research sponsored by Air Force Research Laboratory under agreement number FA8650-12-2-7230 and by the Commonwealth of Pennsylvania, acting through the Department of Community and Economic Development, under Contract Number C000053981. The U.S. Government is authorized to reproduce and distribute reprints for Governmental purposes notwithstanding any copyright notation thereon. Any opinions, views, findings, recommendations, and conclusions contained herein are those of the author(s) and should not be interpreted as necessarily representing the official policies or endorsements, either expressed or implied, of the Air Force Research Laboratory, the U.S. Government, the Commonwealth of Pennsylvania, Carnegie Mellon University, or Lehigh University.

CHAPTER 4

THE EFFECT OF AGING ON THE MICROSTRUCTURE OF SELECTIVE LASER MELTED Cu-Ni-Si

4.1 Abstract

Precipitation hardening copper alloy C70250 was selectively laser melted to successfully produce components around 98 percent dense with high mechanical strength and electrical conductivity. Aging heat treatments were carried out at 723 K (450 °C) directly on as-printed samples up to 128 hours. Mechanical testing found that a peak yield strength of around 590 MPa could be attained with an electrical conductivity of 34.2 %IACS after 8 hours of aging. Conductivity continues to increase with further aging while the peak strength appears to be less sensitive to aging time exhibiting a broad range of time where near-peak properties exist. After aging for 128 hours, there is a drop in yield strength to 546 MPa with an increase in conductivity to 43.2 %IACS. Electron microscopy analysis revealed nanometer-scale silicon-rich oxide particles throughout the material that persist during aging. Deformation twinning is observed in the peak age condition after tensile testing and several strengthening mechanisms appear to be active to varying degrees throughout aging which account for the broad range of aging time where nearly the peak mechanical properties exist.

4.2 Introduction

Selective Laser Melting (SLM) is a powder bed fusion based additive manufacturing (AM) technology that utilizes a laser as the heat source to melt powdered materials.[2] SLM has seen significant growth in both commercial and research settings due in part to its design freedom, flexibility, and low material waste. There have been significant developments in design, processing, and materials for SLM in recent years.[10, 88] From a metallurgical perspective there are a number of challenges and, in fact, potential opportunities associated with the unique processing conditions present during SLM. Notable microstructural features of SLM components that result from these conditions include porosity, very fine solidification substructures, meta-stable phase formation, variable texture development, and incorporation of impurities during processing.[24, 28–32, 35, 38] Recent work has increasingly demonstrated that control of the processing parameters can allow for specific tailoring of grain size, texture and microstructural constituent morphology.[22, 34, 89] As new alloys are evaluated for fabrication via SLM, the possibility of deviation from traditional microstructures (i.e. from classic wrought microstructures), and therefore expected material properties, must be considered and understood for each alloy system that has properties suited to particular applications.

Copper alloys are the preferred choice for applications requiring high electrical or thermal conductivity. In particular, precipitation hardened alloys

are often employed when a balance of high strength and good conductivity are desired. Cu-Ni-Si precipitation hardening alloys, also known as Corson alloys, are used as spring contacts and lead frames as an alternative to beryllium-containing alloys due to the associated health risks. The most common Cu-Ni-Si alloys typically contain 2-3 percent volume fraction precipitates and achieve strengths around 700 MPa with an electrical conductivity of 35-45 percent IACS (International Annealed Copper Standard) in the peak age condition.[16] Although the early stages of precipitation are complex and several nucleation and growth mechanisms have been proposed, it is generally recognized in literature that in the peak age condition the alloys are strengthened by δ-Ni_2Si silicide particles.[68, 71–73] Hu found that the δ-Ni_2Si orientation relationship with the matrix changes as aging progresses, but that in the peak age condition the precipitates have a disc morphology and an orientation relationship such that $[010]_{\delta}||[110]_{Cu}$ and $(001)_{\delta}||(001)_{Cu}$.[74] Aging is typically carried out at 723 K (450 °C) with peak aging times ranging from around 1-25 hours based on the chemistry of the particular Cu-Ni-Si alloy being investigated.[68, 71–74] Cu-Ni-Si alloy C70250, which contains small amounts of Mg, is of particular interest because of its high strength, high conductivity, and improved stress-relaxation resistance over competing Cu-Be alloys.[16] Although C70250 is a wrought alloy, there are no practical barriers for utilizing it in powdered form which, in combination with the established commercial applications for C70250, makes it an interesting candidate for use in SLM. In

SLM, copper alloys are often used as a liquid phase sintering component rather than the bulk material.[2] In addition, a recent study evaluated the Cu-4.3Sn binary system as a candidate for SLM.[17] The study successfully demonstrated that the mechanical properties of SLM components made from this alloy could be controlled via post-process heat treatment. Similar features to studies on other alloys were observed such as epitaxial growth and a fine cellular solidification structure. Furthermore, nanometer scale tin oxide particles were finely dispersed in the alloy similar to oxides which have also been observed in SLM iron alloys.[64] However, the strength and conductivity of the binary were relatively low in comparison to high performance precipitation hardened copper alloys like C70250. Therefore, it is essential to investigate detailed microstructure evolution of C70250 alloys fabricated by the SLM process in order to meet demand for better electrical performance. In this study, detailed microstructure characterization has been performed by conventional metallography through advanced electron microscopy in combination with measurements of mechanical properties and electrical conductivity.

4.3 Experimental Methods

Pre-alloyed inert gas atomized powder was acquired from ECKA Granules for this investigation. The composition of the powder is shown in Table 3 and is within the specifications for alloy C70250.[16] An EOSINT M280 Direct Metal Laser Sintering (DMLS) unit with a 200 Watt Yb-fiber laser

was used to fabricate samples for investigation. During processing, a nitrogen atmosphere was used to minimize oxygen in the build chamber.

Table 3. C70250 powder composition from ECKA Granules specifications.

Element	Cu	Ni	Si	Mg	Fe	Zn	Mn	Pb
Weight %	Bal.	3.3	.9	.13	.08	.6	<.01	<.01

A common raster scanning strategy with 90° of rotation between each build layer was used for the internal portion of the components with pre-contour and post-contour passes around the perimeter. Laser parameters were selected based on a preliminary investigation by TE Connectivity to find the maximum attainable as-printed density evaluated by the Archimedes technique and verified by area fraction measurements on metallographic samples. The resulting energy density (Q) for sample fabrication was 107 J/mm^3 based on the adapted laser welding equation from Roehling.[22] The final energy density is in the range of values reported in literature for other alloy systems and in the case of this investigation produced components with a density of approximately 98 percent. Specimens with various geometries were built on a steel baseplate with copper alloy support structures in between. Cubes (1 x 1 x 1 cm^3) were fabricated for density measurements and microstructural analysis, strip (1 x 1 x 60 mm^3) samples were used for conductivity measurement, and rectangular prisms (110 x 4 x 14 mm^3) were printed for mechanical testing. All samples were oriented with the long axis slightly offset from the powder wiper-blade travel axis to avoid defects during powder spreading. All post-fabrication heat treatment was completed in a calibrated

tube furnace under a cross-flow of argon. Solution treatments were done at 1173 K (900 °C) with a soak time of 1 hour followed by a water quench based on studies on wrought C70250.[68, 71, 74] Aging treatments were carried out at 723 K (450 °C) followed by air cooling. The heating rate was 15 K/minute, all aging times are presented as the time spent at the target temperature.

Uniaxial tensile testing was performed after rectangular prisms were heat treated then machined to 3 mm thick ASTM E-8 sub-size specifications (overall length of 100 mm, 10 mm wide in the grip section, and a 32 x 6 mm^2 reduced section with a 6 mm radius filet). The loading axis was perpendicular to the build direction and the samples were held using serrated mechanical wedge grips. A 30-kN load cell was used on an Instron 5567 load frame in conjunction with an Instron AVE2 video extensometer to measure strain. Three samples of each condition were measured. The properties extracted from each curve were averaged for presentation. Yield strength was measured using the 0.2 percent offset method and elongation was taken as the total strain at failure. The work hardening rate was determined from one representative curve after the engineering stress-strain data was converted into true stress and true plastic strain by the derivative function in Origin and smoothed using adjacent averaging. Conductivity was determined from 4 samples of each condition and averaged using the 4-contact method on a Keithley 580 Micro-Ohmeter. The conductivity data was then expressed as a

percentage of the International Annealed Copper Standard (%IACS) based on the resistivity of pure copper (172.41 µΩ-cm).[16]

A high speed abrasive cutoff wheel was used to cut samples that were then mounted in cold-setting epoxy for metallographic examination. Standard metallographic preparation was completed with a final attack polish (1% ammonium hydroxide, 1% hydrogen peroxide, and 98% 0.05 µm colloidal silica) before etching in Klemm's I reagent (50 ml saturated aqueous sodium thiosulfate and 1 g potassium metabisulfate) for light optical microscopy (LOM). For twinning observation, LOM samples were etched in a solution of 5 g ferric nitrate, 25 ml hydrochloric acid and 70 ml water. For each condition 50 Vickers microhardness measurements were taken on un-etched metallographic samples using a load of 300 g and a 15 second dwell time. Strip samples polished to 1 µm were used for x-ray diffraction (XRD) conducted on a PANalytical Empyrean unit using Cu Kα radiation and a Bragg-Brentano setup. A θ:θ scan was done for 2θ angles from 10° to 100° with a step size of 0.013° using a PIXcel3D-Medipix3 area detector in scanning line detector mode. XRD peaks were identified by comparison to simulated diffraction patterns from JEMS electron microscopy simulation software.

Electron Backscatter Diffraction (EBSD) measurements were conducted in a Hitachi 4300 field-emission scanning electron microscope (FE-SEM). EBSD analysis was completed using TSL OIM software. Thin-foil

specimens for Transmission Electron Microscopy (TEM) and scanning TEM (STEM) were prepared using an FEI SCIOS Focused Ion-Beam (FIB) instrument and cleaned using a Fischione 1040 NanoMill, operated at 900 eV, to remove surface damage induced during FIB thinning. TEM characterization was carried out on a JEOL 2000FX operated at 200 kV. Selected area diffraction (SAD) patterns were indexed and compared to simulated patterns from JEMS electron microscopy simulation software.[90] Precipitate/secondary-phase size was determined by averaging 50 particle measurements directly from dark-field TEM micrographs. A JEOL JEM-ARM200CF aberration-corrected STEM was used for imaging and analysis including X-ray Energy Dispersive Spectrometry (XEDS). XEDS data obtained from STEM work was quantified using the ζ-factor method.[91]

4.4 Results

Figure 28 shows the physical properties obtained from uniaxial tensile tests and four-point conductivity measurements of SLM C70250 aged at 723 K (450 °C) from the as-printed condition. At this temperature, the mechanical properties change quite rapidly and after just one hour the yield stress is 80 percent of the peak attainable yield stress. After the initial rapid increase in properties, there is a small additional increase in strength with aging time until the curve begins to plateau. As a result, the peak aging time is not well defined and there is a relatively large window where nearly the nominal peak strength exists. The absolute highest measured average value of yield strength of 596

MPa occurs after 32 hours of aging; however, the yield strength is within the standard deviation of the maximum value from 8 hours to 32 hours of aging. The maximum average value of the ultimate tensile stress of 711 MPa was obtained after 8 hours of aging. The ultimate tensile strength has a similar but lower range of time where there is no statistically observable change from around 4 to 16 hours of aging. In the context of this study, the “peak age” time was defined as the lowest amount of time to achieve a strength within the standard deviation of the maximum measured value. Therefore, the peak age heat treatment was 8 hours at 723 K (450 °C) for SLM C70250. After 128 hours of aging, there is a definite drop in both ultimate tensile strength and yield strength and thus it was defined as the “over age” condition for comparison. Decreases in ductility predictably follow a similar trend as the yield strength and ultimate tensile strength. Following a significant drop in ductility after 1 hour of aging, there is relatively little further change as aging progresses. The conductivity increases as aging progresses. This has also been shown in studies on wrought C70250.[76, 92, 93] Conductivity in metal alloys is dramatically affected by solute atoms that serve as additional scattering centers in the copper matrix, while second phase particles in the matrix have a much less pronounced effect. Consequently, as precipitation progresses and solute atoms are removed from the matrix to form second phase particles the conductivity increases.[16, 57] Additionally, the size of the precipitates indirectly affects the conductivity of the matrix via the Gibbs-

Thomson effect which accounts for the continued increase in conductivity as precipitates grow during the later stages of aging.[61]

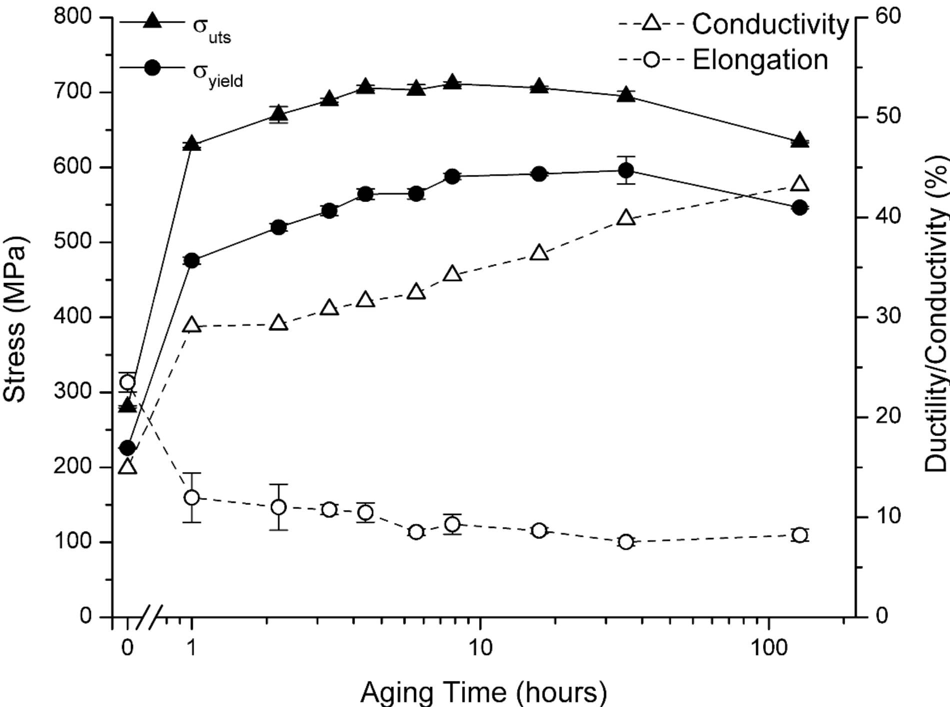

Figure 28. Physical property evolution of SLM C70250 during aging at 723 K (450 °C) from the as-printed condition.

Polarized light optical micrographs of the as-printed grain structure are shown in Figure 29. The black marks in Figure 29(a) are reference microhardness indents. The grains are significantly elongated in the build direction and extend through several build layers. The transverse orientation, Figure 29(b), shows regions on the order of the beam size (~200 μm) that have a grain structure similar to high speed welds with elongation in the heat source travel direction characteristic of teardrop shaped weld pools.[33]

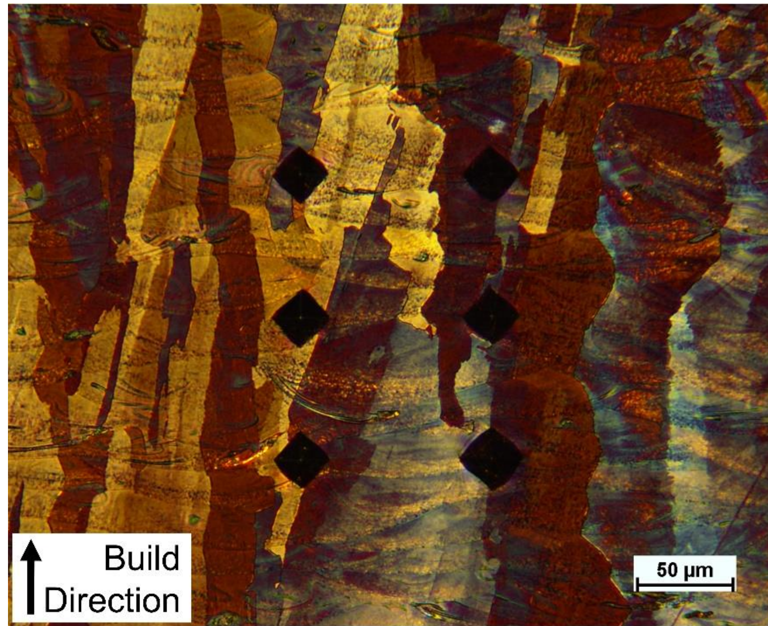

(a)

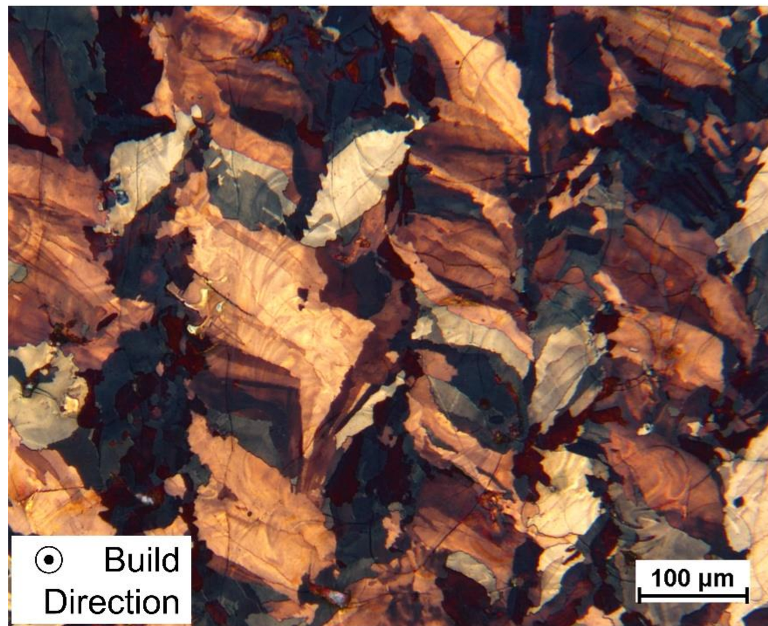

(b)

Figure 29. Polarized light optical micrographs of as-printed SLM C70250 in the (a) build direction and (b) transverse direction.

Figure 30 shows a bright-field TEM micrograph of the melt pool boundary in as-printed SLM C70250. The sample was extracted from a region

similar to Figure 29(a) such that the solidification substructure near the melt pool boundary, which is difficult to resolve in optical microscopy, could be examined in TEM. A high density wall of dislocations can be seen in the intercellular regions of the solidification substructure. Additionally, there are second phase particles (two examples are indicated by arrows) that can be found primarily in the intercellular regions. Moving away from the melt pool boundary along the build direction (not shown in Figure 30) the spacing of the cells becomes finer until it is difficult resolve a cellular structure. The maximum intercellular spacing, i.e. at the melt pool boundary, is approximately 500 nm.

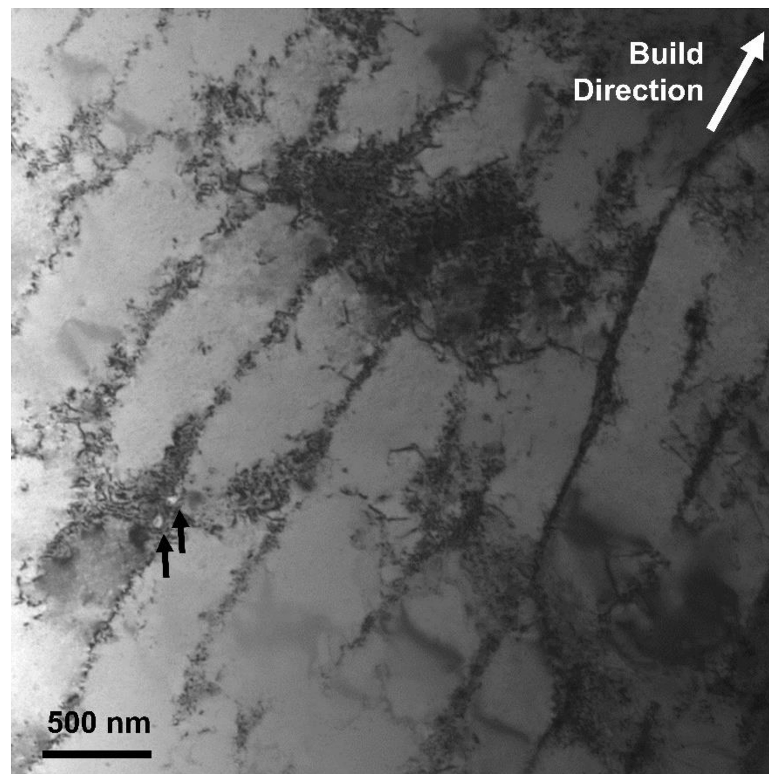

Figure 30. Bright-field TEM micrograph of dislocations in the solidification substructure at the melt pool boundary in as-printed SLM C70250.

Figure 31 shows XRD measurements of SLM C70250 at various stages during aging. In the as-printed condition the copper matrix peaks are well defined. As aging progresses, the shape of the copper peaks changes slightly as some asymmetry develops. The over age sample is the only sample in which evidence of the δ-Ni_2Si diffraction peaks can be seen, and even then only the most intense peaks are clearly shown due to the small volume fraction of particles. Thus, the XRD results alone are insufficient for confirming the identity of the strengthening precipitates.

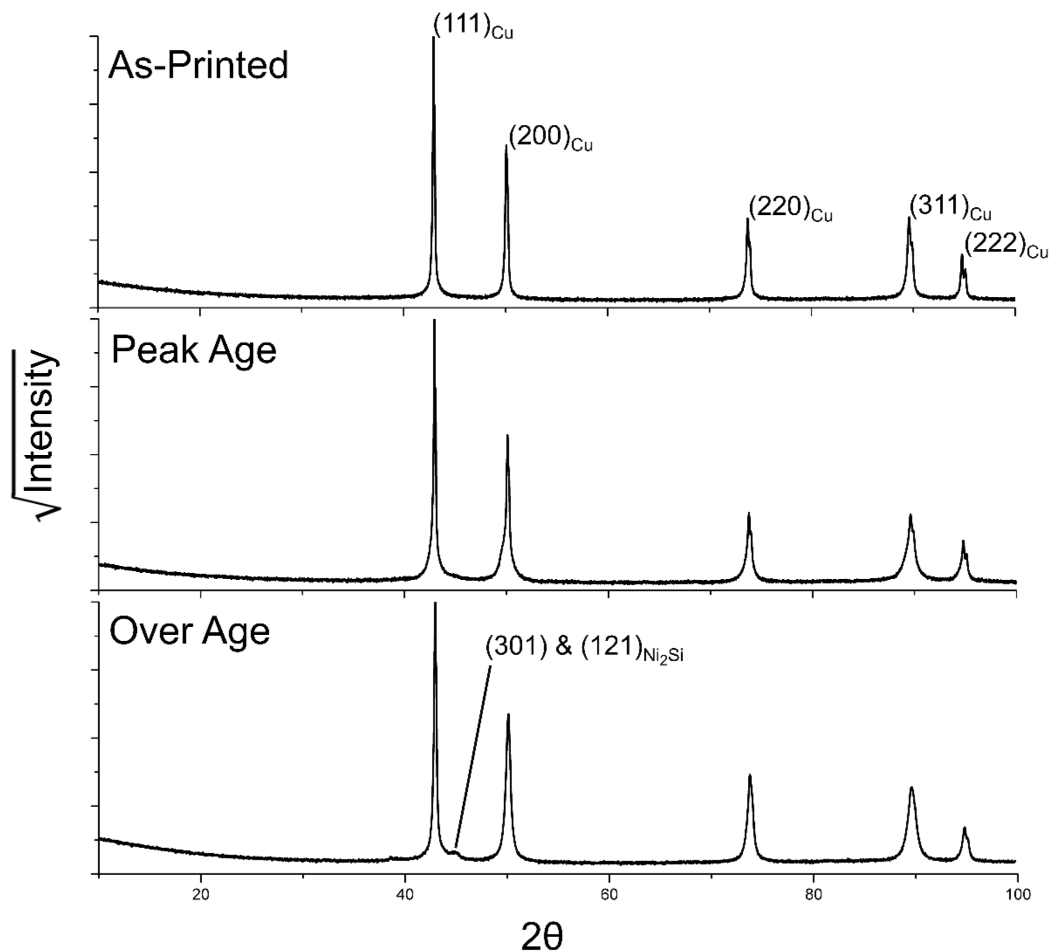

Figure 31. XRD patterns of SLM C70250 at various stages of aging.

Figure 32 and Figure 33 show dark-field TEM micrographs and corresponding SAD patterns (dark-field aperture indicated by circle), taken of the $<111>_{Cu}$ projection, that confirm the strengthening precipitates are δ-Ni_2Si. Figure 32 shows the peak age condition and Figure 33 shows the over age condition. The precipitates are consistent with literature on wrought Cu-Ni-Si alloys.[71, 74] The precipitates lie on the $\{110\}_{Cu}$ matrix planes. In Figure 32(b) and Figure 33(b) the disc-shaped precipitates are oriented parallel to the beam and the resulting diffraction spots are elongated normal to the $\{110\}_{Cu}$ planes from each of the precipitate variants.[69–71, 74] Direct measurement of the particles from dark-field images indicate that in the peak age condition the long axis (diameter of the discs) is approximately 7.0 ± 1.7 nm while in the over age condition it is 19.4 ± 5.5 nm. The measurements are in reasonably good agreement with the measurements made by Lockyer and Noble under the same aging conditions.[71]

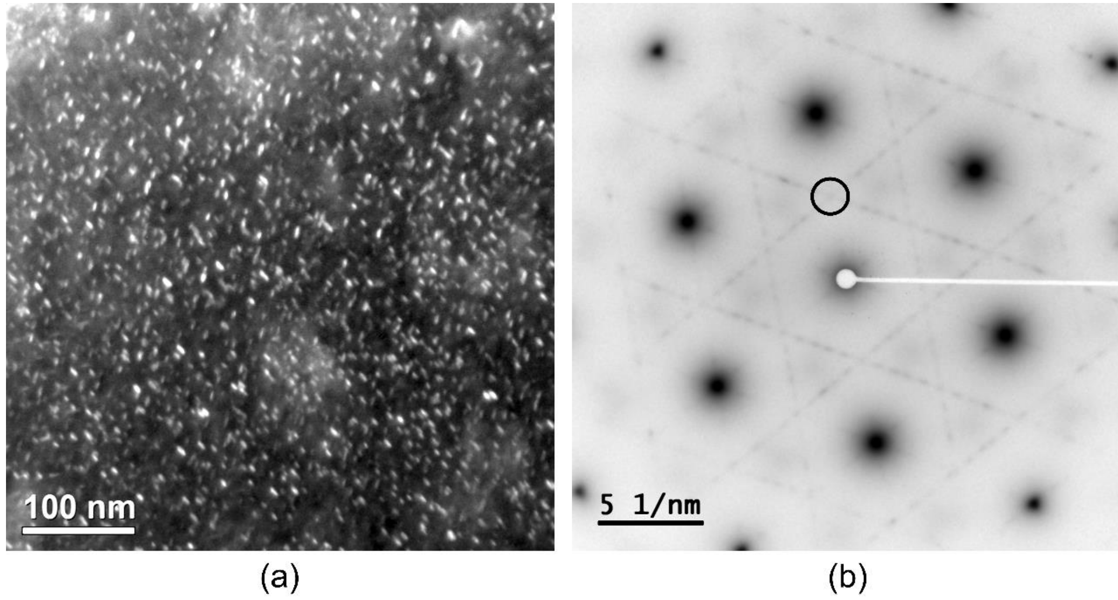

Figure 32. (a) Dark-field TEM micrograph of the δ-Ni_2Si strengthening precipitates in the peak age condition and (b) the corresponding SAD pattern of the $[111]_{Cu}$ matrix projection.

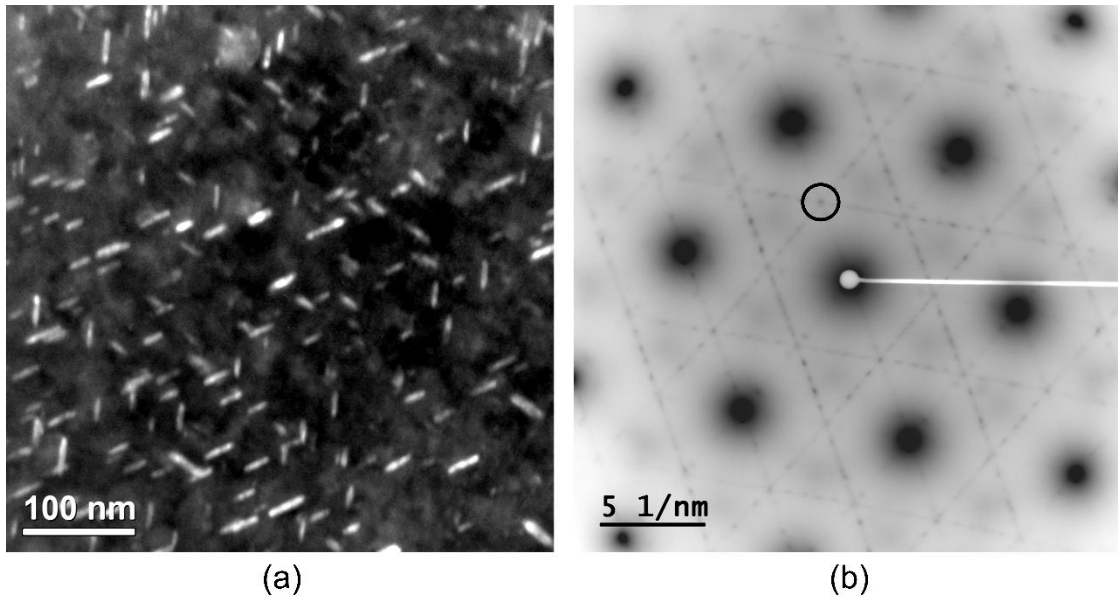

Figure 33. (a) Dark-field TEM micrograph of the δ-Ni_2Si strengthening precipitates in the over age condition and (b) the corresponding SAD pattern of the $[111]_{Cu}$ matrix projection.

4.5 Discussion

4.5.1 As-Printed Microstructural Features

In SLM, grains typically grow epitaxially from the previously solidified layer.[17, 24, 34, 38] According to classical nucleation theory the energy barrier for nucleation is zero when the liquid completely wets the solid substrate. In SLM, as in autogenous welding, the liquid composition is nominally the same as the solid and thus there is complete wetting and the lack of energy barrier for nucleation results in epitaxial growth.[33, 62] The subsequent grain structure consists of highly elongated grains that extend through many build layers as shown in Figure 29. Other nucleation mechanisms can occur at locations away from the fusion line, and it has been suggested that several of those mechanisms can be active during SLM. Some mechanisms that have been suggested include epitaxial growth from partially melted powder particles, dendrite fragmentation, heterogeneous nucleation on impurities, and surface nucleation.[22, 24, 34] In the case of dendrite fragmentation, heterogeneous nucleation, and surface nucleation, equiaxed grains would be expected to form and be visible away from the fusion line. In this investigation, no equiaxed grains were observed in the as-printed microstructure. However, there is a significant amount of re-melting during the printing process that may be eliminating such grains or elongating those grains into the next build layer thereby masking their initial morphology. Regardless, the microstructure in the finished component consists of grains elongated in

the build direction, with some variation in the exact elongation axis as a result of the change in scan direction between scan lines and build layers which alters the solidification direction. The grain morphology can be significantly altered by subtle variations in the size and shape of the weld pools. The weld pool shape is sensitive to processing parameters and even small impurity element concentrations.[33] A single-track study would allow for a detailed analysis of the nucleation mechanisms active in SLM C70250 potentially allowing for tunable grain morphology during fabrication, but this was outside the scope of this particular investigation.

The morphology and size of the solidification substructure is highly dependent on the temperature gradient (G) and the solidification/growth rate (R). When there is a moving heat source, as opposed to a simpler case of casting, for example, G and R vary based on position in the weld pool. R is related to the scan speed by $R=V \cos \alpha$ where V is the scan speed and α is the angle between the scan direction and the normal to the solid liquid interface. The ratio of G/R dictates the type of solidification substructure, while the product of GxR (the cooling rate) defines the scale of the substructure.[33] In SLM, as in classic welding metallurgy, G and R vary throughout the weld pool which typically results in changes in the substructure with distance from the fusion line (i.e. from the previous build layer). Figure 34 shows a bright-field light optical micrograph of the solidification substructure in the as-printed condition. The segregation is a cellular morphology of varying size throughout

the microstructure. In some regions, seen in the bottom of Figure 34, a small planar growth region exists, however this region is highly unstable and quickly transitions into a cellular structure even in the cases where it is present. At the weld fusion line, G is at a maximum but R is minimum. Moving towards the centerline, R increases while G tends to decrease because the region was previously melted and thus the temperature gradient is lower. The change in G is likely less significant than the change in R because of the small size of the weld pool compared to the rest of the build and the high thermal conductivity of copper (i.e. there is a significant heat sink and the heat is easily carried away). Apparently, the ratio of G/R has a relatively insignificant change as the solidification substructure remains cellular similar to SLM of other alloys.[24, 31] In contrast, GxR increases with distance from the fusion line so the substructure gets much finer as shown in Figure 34.

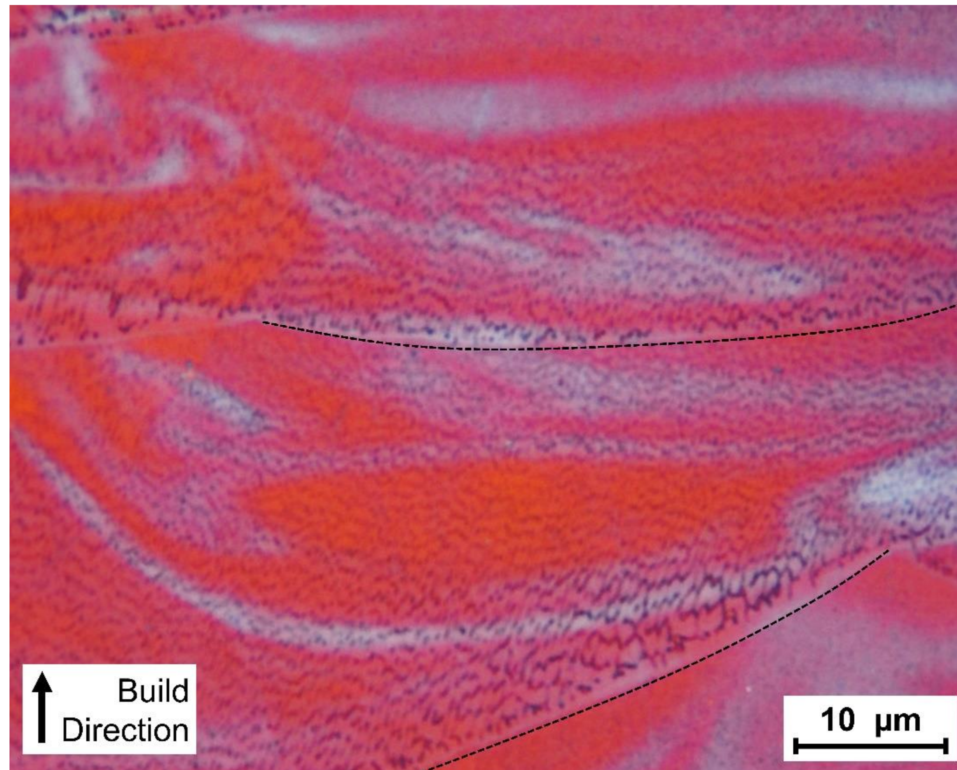

Figure 34. Bright-field LOM micrograph of as-printed SLM C70250 showing the change in solidification substructure scale throughout the weld pools. Dashed lines mark the fusion line of two melt pools.

To attain a more detailed understanding of the segregation in the as-printed part and to identify the unknown particles in Figure 30, XEDS analysis was conducted. Figure 35 shows the elemental maps of two cells taken from the same sample as Figure 30 along with a bright-field STEM micrograph of the same field of view. The general segregation of the main alloying elements (Ni and Si) is in line with predications based on the partitioning coefficients (the average ratio of solute in the solid to the liquid over the solidification temperature based off of the binary phase diagrams).[62, 94] Nickel tends to segregate mildly to the cell core while silicon segregates to the boundary. In SLM, due to the extremely high cooling rate, some degree of dendrite tip

undercooling and solute trapping may be expected. The resulting segregation of silicon would tend to be less significant than in conventional solidification processes thus limiting any detrimental effects of segregation.[22, 33, 94] The oxygen and tin found in the XEDS analysis are not intentionally added in the C70250 specification and are therefore considered as impurities.

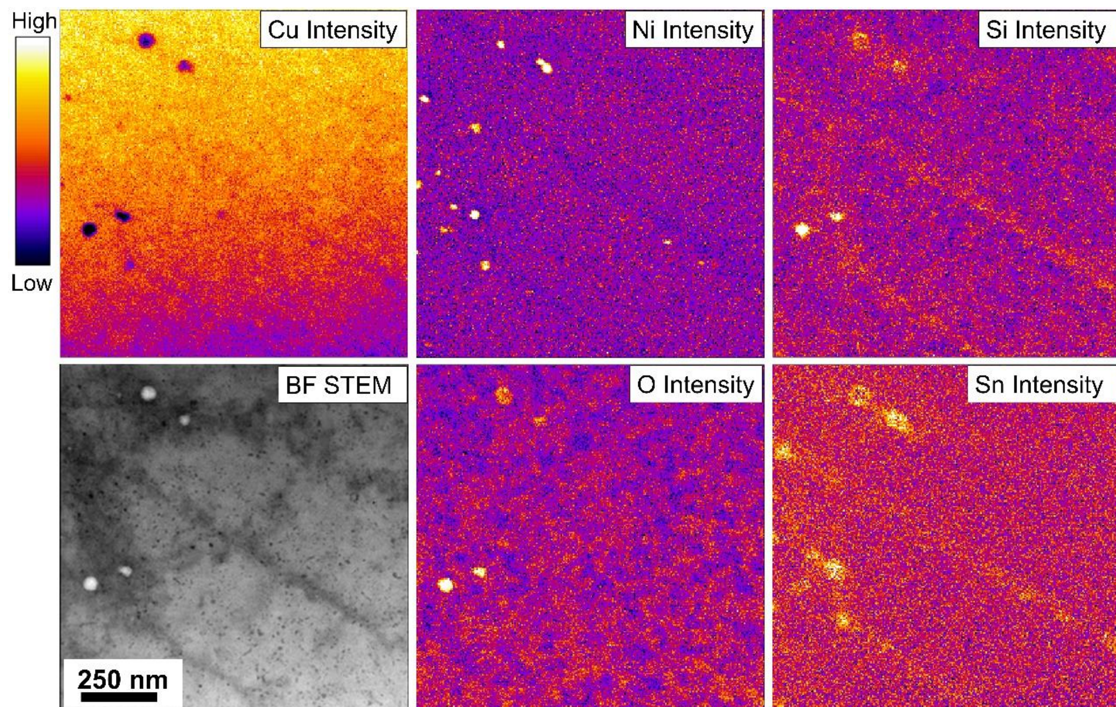

Figure 35. Bright field STEM and XEDS intensity maps (normalized to the Cu intensity) of the solidification substructure at the weld line in as-printed SLM C70250.

Two unexpected features appear to exist in the intercellular regions. The first is discrete particles of high silicon and oxygen intensity. No diffraction spots could be detected from the silicon- and oxygen-rich particles suggesting that they are an amorphous silicon-rich oxide particle. Oxide particles with different morphologies have been shown to form in SLM components.[17, 64]

Additionally, oxide dispersion strengthened powdered metals processed via SLM retain their distribution of oxide particles.[63] The source powder for this investigation was inert gas atomized, therefore it is likely that oxygen was introduced to the melt pool during fabrication either from the build chamber or the surface of the powder that was stored in open air, rather than discrete oxide particles being retained from within the source powder. The oxide particles are expected to form in the melt due to the high oxygen affinity of silicon then be pushed to the intercellular regions as solidification progresses.[87] The cooling rate in SLM is extremely high, which is in line with the seemingly amorphous structure of these oxide particles. Additionally, literature characterizing oxide particles observed in SLM steel alloys, although larger than those observed in this study, found that the oxide particles are amorphous.[64, 95] The particles in this case are well distributed due to the fine solidification substructure, particularly away from the fusion line.

The second unique feature in the intercellular regions is the nickel and tin distributions. In this case nickel-rich refers to the discrete high concentrations of nickel in the cell wall in Figure 35 rather than the much less pronounced tendency for nickel to be in the cell core as predicted by classic solidification theory. The tin appears to segregate generally to the intercellular regions but is particularly concentrated in the same areas as the nickel rich regions. Nickel forms a fully miscible solid solution with the FCC copper matrix and in fact tends to concentrate towards the cell cores, so the presence of

nickel rich regions in the cell walls is unique. In several cases, the nickel- and tin-rich regions coincide with the oxide particles. Furthermore, the morphology of some particles suggests a nickel rich “core” with a combination of tin and silicon rich oxide surrounding. This may indicate some relationship as a site for heterogeneous nucleation between the two features, however this could not be confirmed and requires further investigation. Nevertheless, determining the attainable performance of SLM C70250 with regard to microstructural and mechanical property development during aging was that primary goal of this investigation. Considering this perspective, it is worth noting that of the unique solidification features discussed in this section, the oxide particles are the only feature that persists through aging at 723 K (450 °C). The solidification segregation and discrete nickel-tin rich regions were not observed during TEM analysis of either the peak age samples or over age samples. Additionally, the precipitates shown in Figure 32 and Figure 33 for the peak and over age condition were homogeneously distributed throughout all samples investigated, indicating that any segregation of the principle alloying elements was either eliminated early in the heat treatment or did not significantly influence the precipitation process.

4.5.2 Aging and Precipitation Contributions to Strengthening

To ensure that solidification segregation was not influencing the bulk properties, an exploratory high temperature heat treatment was carried out as a homogenization and solution treatment for a small number of specimens.

Figure 36 shows a comparison of microhardness and electrical conductivity between samples aged directly after printing (P+A) and samples aged after an intermediate solution treatment (P+ST+A) at 1173 K (900 °C). The samples that underwent solution treatment had a lower microhardness than the as-printed sample. However, during aging the average microhardness of the solution-treated samples is quite close to the printed and aged samples. The consistently lower microhardness of the solution treated samples may be the result of recovery and/or grain growth during the solution treatment, but the general trend is the same because precipitation hardening is the dominant strengthening mechanism in this alloy. The conductivity measurements also indicate that the as-printed samples had the same aging characteristics as the solution-treated samples. Based on these observations, solution treatment is unnecessary for SLM C70250. The high cooling rate of the SLM process appears to be sufficient to form a supersaturated solid solution in this alloy which facilitates aging directly after fabrication. Additionally, eliminating an unnecessary heat treatment will benefit the turnaround time and economics of the process in a commercial setting.

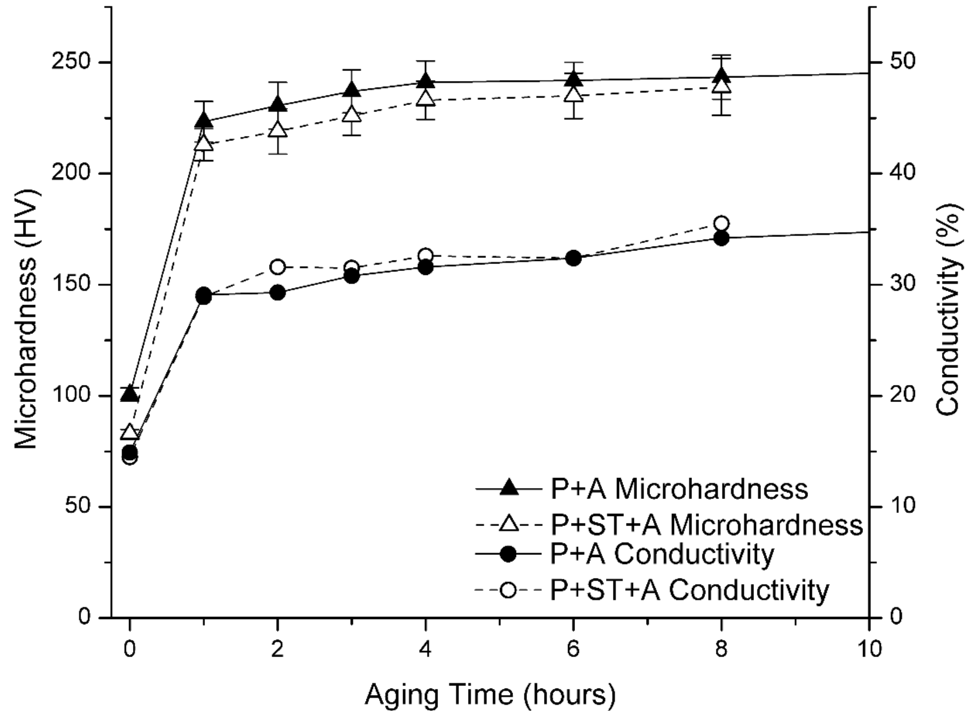

Figure 36. Microhardness and electrical conductivity comparison between SLM C70250 aged directly after printing (P+A) and samples that had an intermediate homogenization/solution heat treatment (P+ST+A).

Discontinuous precipitation (DP) and coarsening have been proposed as one of the mechanisms by which over aging occurs in Cu-Ni-Si alloys.[80, 96] DP results in a lamellar structure (of the matrix and the precipitate) devoid of the continuous precipitates in the vicinity of a migrating boundary due to the high diffusivity pathway. As aging progresses and the boundary moves, the DP zone grows in size and generally lowers the strength of the alloy.[81] Figure 37(a) shows a secondary electron micrograph with an exemplar DP zone in over aged SLM C70250. Figure 37(b-d) shows bright field TEM and SAD analysis of a particle in the DP zone. The precipitates in the DP zone appear to be of the same δ-Ni_2Si type. The discontinuous precipitates maintain

the same orientation relationship as the continuous precipitates, however misfit dislocations appear between the particle and the matrix to accommodate losses in coherency as the particles grow (marked by an arrow in Figure 37(b)). The average spacing of the misfit dislocations is approximately 7.8 nm, which is in line with the 8.26% mismatch between the interplanar spacing of the $(100)_{\delta}$ planes and the $(0\bar{1}1)_{Cu}$ matrix planes determined by Hu.[74] The volume fraction of DP zones in the over aged condition was about 1.9 percent which is quite low compared to studies on wrought C70250 where DP was observed around 90 volume percent at comparable aging conditions.[96] No DP zones were observed in the peak aged condition. Boundary mobility plays a large role in the presence of DP zones, and it is affected by the presence of second phase particles. The oxide particles identified in SLM C70250 may be acting as barriers for boundary migration thereby limiting the extent of DP. Given the low volume fraction of DP zones in SLM C70250, the decline in properties from peak age to over age is likely related to other additional factors.

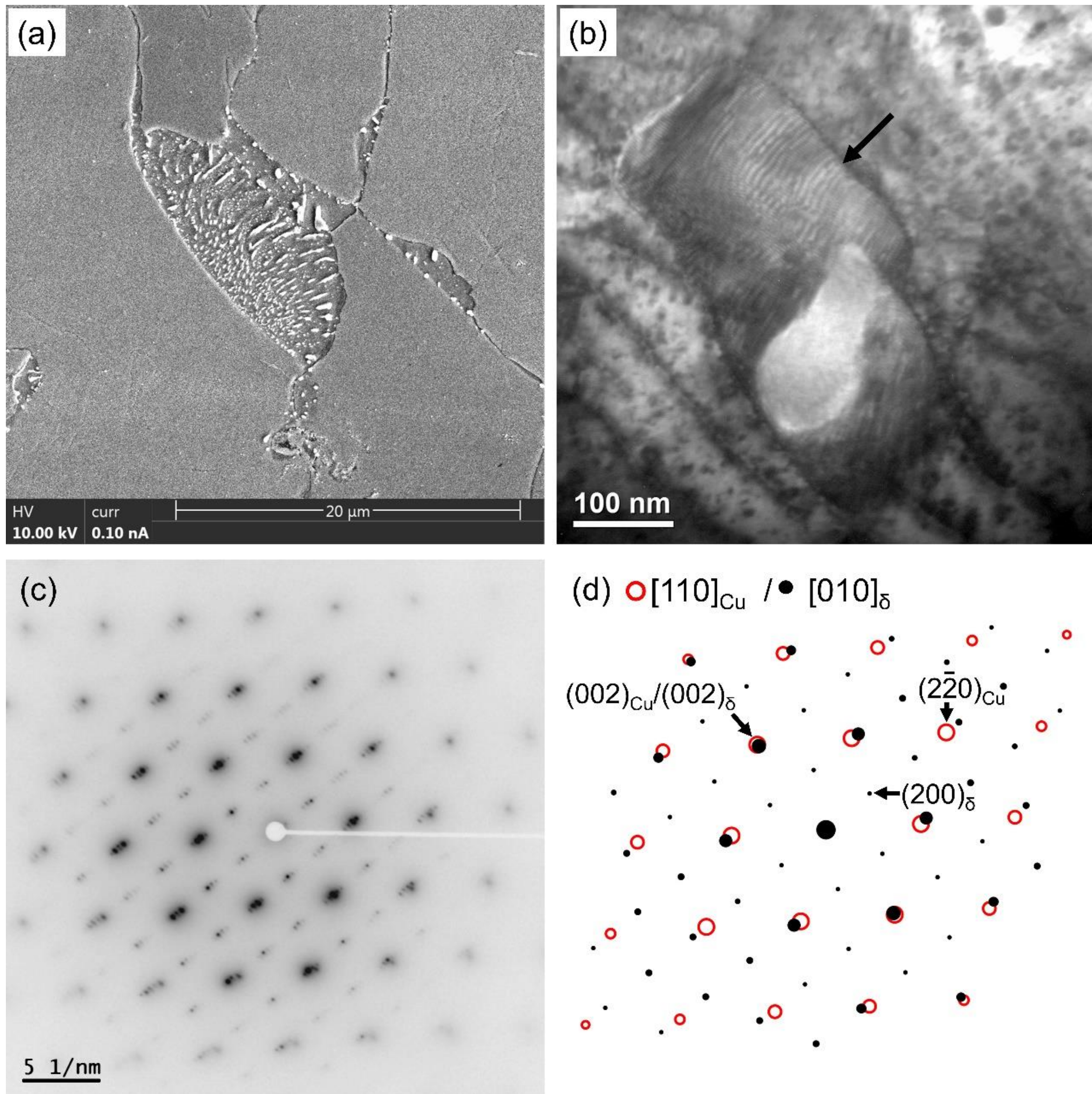

Figure 37. (a) Secondary electron micrograph of a DP zone in over aged SLM C70250 (aged for 128 hours). (b) Bright field TEM micrograph of a precipitate in the DP zone, (c) accompanying SAD pattern of the $[110]_{Cu}$ || $[010]_{\delta}$ projection and (d) the corresponding simulated diffraction pattern.

There are two types of particles that contribute to the strength of the SLM C70250 alloy in the heat-treated state: oxide nanoparticles and precipitates. The increase in yield strength ($\Delta\sigma_y$) resulting from non-shearable particles in a polycrystalline material follows the Ashby-Orowan relationship:

$$\Delta\sigma_y = \frac{0.538 * Gb\sqrt{f}}{X} ln \frac{X}{2b} \quad \textit{Equation 7}$$

where G is the shear modulus of the matrix (48.3 GPa), b is the magnitude of the Burgers vector (0.255 nm), *f* is the volume fraction of particles, and X is the diameter of the particles.[49, 97] An XEDS map of the solidification structure in the as-printed condition was quantified using the ζ-factor method to determine the thickness of the TEM sample. High angle annular dark field STEM imaging of the oxide particles was then used to determine a rough size and volume fraction of oxide particles to estimate their contribution to strengthening. The oxide particles were spherical with an average diameter of 33 nm and a volume fraction around 0.25 percent. The calculated increase in yield strength from the oxide particles per the Ashby-Orowan equation is 42 MPa. Additionally, the morphology of the particles did not change throughout aging based on TEM observations, therefore the oxide particle contribution to strengthening is expected to be constant in all of the sample conditions in this study.

Literature on wrought Cu-Ni-Si alloys suggests that at and beyond the peak age condition, the δ-Ni_2Si precipitates also strengthen the material via the Orowan mechanism. The overall domination of looping compared to shearing was attributed to the complex structure and orientation relationship of the precipitate with respect to the slip systems in the FCC matrix.[71] Within the aging times investigated in this experiment, the precipitate diameter and thickness increase during aging (precipitate growth) is well expressed as a

power-law model. [68, 71] Here, the two TEM direct measurements of the precipitate thickness in the peak age and over age condition were fitted to a power law function to give an estimate of the precipitate thickness throughout aging. The volume fraction of precipitates in wrought C70250 is typically on the order of 2-3 percent.[16] The volume fraction was also measured directly from STEM analysis at the peak age condition in a similar manner to the oxide particles. An XEDS map of the strengthening precipitates was quantified using the ζ-factor method to determine the volume of δ-Ni_2Si in the field of measurement. The determined volume fraction was 2 percent, which is in good agreement with the expected value and was therefore used in further calculations. Figure 38 shows a plot comparing the experimentally determined increase in yield strength versus precipitate thickness and the expected increase in strength calculated from the Ashby-Orowan equation.

The experimental measurements of yield strength show reasonably good agreement with the Ashby-Orowan equation at the two longest aging times when the disc thickness is considered as the critical particle dimension. In contrast, calculating a spherical equivalent diameter of the disc-like precipitates (not shown) results in significantly larger measured strength increases compared to the Ashby-Orowan predicted strength increase, particularly in the over age condition where looping is more likely to be the active mechanism. This suggests that the disc thickness is the most important dimension to consider when estimating the precipitate strengthening response

of SLM C70250. In actuality, the interparticle spacing determines the strengthening contribution of a distribution of hard (non-shearable) particles.[49] The Ashby-Orowan equation assumes spherical precipitates to relate the volume fraction and particle diameter to the interparticle spacing. However, the δ-Ni_2Si discs that lie on the $\{110\}_{Cu}$ planes can have varying orientation relationships to the slip systems in FCC, and the effective interparticle spacing is difficult to directly relate to particle dimensions. Although the thickness of the disc-like precipitates appears to fit the predicted increase in strength reasonably well, an average of the possible orientations of the precipitates on the slip planes could provide a more accurate model of the precipitate strengthening in SLM C70250. Additionally, the coherency strain around the precipitates may affect the strengthening contribution of the precipitates, but further investigation would be required to develop a more accurate precipitation strengthening model for SLM C70250.

The peak of the experimentally measured increase in yield strength as shown in Figure 38 indicates a transition in the yielding or dislocation-particle interaction mechanism. Traditionally, this corresponds to the transition from shearing to looping as the precipitates grow larger than a critical size that depends on the system being investigated. [49, 59] Literature on wrought Cu-Ni-Si alloys has suggested that the precipitates would be difficult to shear due to their structure and orientation with the slip systems in the copper matrix, but some shearing may occur in the under aged conditions. [71] This shearing

was hypothesized to control the yielding behavior in those conditions which would be consistent with the trend observed in Figure 38, but the peak age condition in SLM C70250 in this investigation does not appear to depend entirely on the looping mechanism based on the deviation from the model.

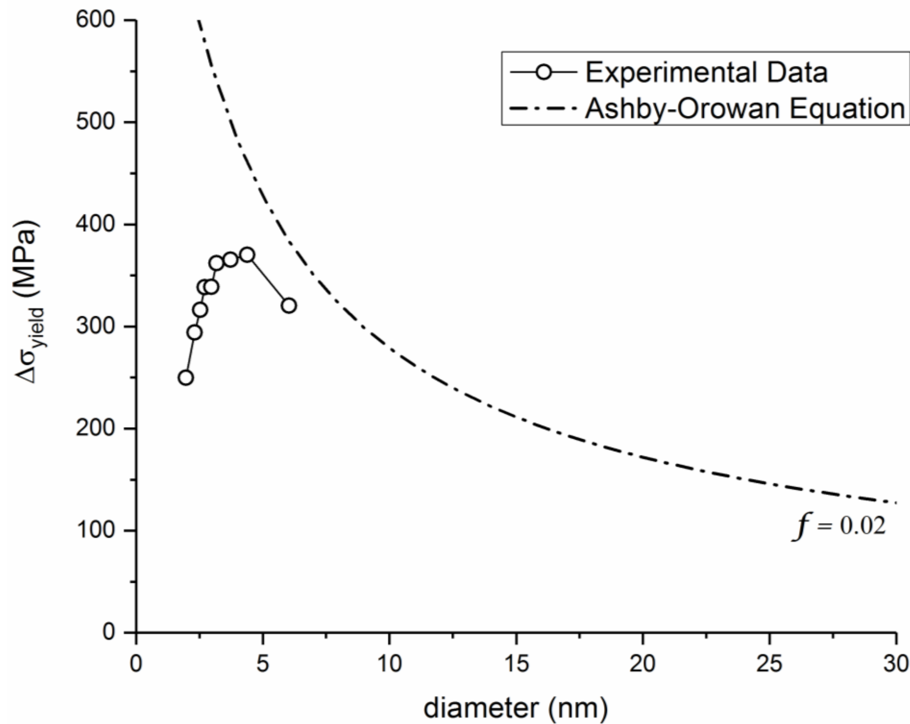

Figure 38. Experimental increase in yield strength vs the precipitate thickness compared to the Ashby-Orowan equation.

4.5.3 Other Contributions to Mechanical Property Development

To determine if the peak in the strengthening contribution from the precipitates observed in Figure 38 corresponds to the shearing-looping transition, the work hardening rate was investigated. The work hardening rate of aluminum alloys has been used as an indirect method to investigate the transition from shearing to looping of strengthening precipitates.[48, 98]

Although coherent, shearable, precipitates resist dislocation motion thereby increasing the yield strength, they do not typically affect the work hardening rate. Non-shearable particles, however, decrease the geometric slip distance (λ_g) which is inversely related to the density of geometrically necessary dislocations. In alloys with plate-like precipitates, λ_g is equal to the plate spacing (in a single phase polycrystals, λ_g is equal to the grain size). As a result, when non-shearable particles are introduced the amount of geometrically necessary dislocations required during deformation increases and the work hardening rate also increases.[99] The work hardening rate(Θ) is described by the slope of the stress-strain diagram at any point after yielding:

$$\Theta = \frac{\partial \sigma}{\partial \epsilon} \quad \textit{Equation 8}$$

where σ is the flow stress and ϵ is the true plastic strain.[46, 47] If there is a transition from shearable to non-shearable precipitates in aluminum, it manifests as a change in the shape of the work hardening versus normalized flow stress curve. In that case, after a rapid decline in rate, there would be a temporary rate increase near the yield strength followed by further decline, as compared to the nearly linear downward slope of single phase FCC polycrystals.[47] Figure 39 shows the work hardening rate versus the normalized flow stress for SLM C70250 throughout aging. It should be noted that these curves were extracted from tensile tests conducted at constant extension rate rather than constant strain rate, and porosity was not considered in this analysis. The effect of these variables is consistent among

the data presented in Figure 39 which should allow for relative comparisons but not reporting of the absolute measured values. The as-printed work hardening rate is in line with the typical behavior for single phase FCC metals.[46–48, 98, 99] Throughout aging, the work hardening rate is higher than that of the as-printed material. This was not observed in previous work hardening studies on a similar Cu-Ni-Si-Mg alloy and suggests that particle shearing is not the only mechanism active in any of the investigated aging conditions.[75] The initial stage of the curve where a rapidly decreasing work hardening rate is observed before the lower portion is also larger in the aged conditions compared to the as-printed condition. Although there are subtle differences between the different aging conditions, there is no definitive change in the curve shape, as was observed in other alloys, that would indicate a significant shift in dislocation-particle interaction mechanisms.[48, 75, 98]

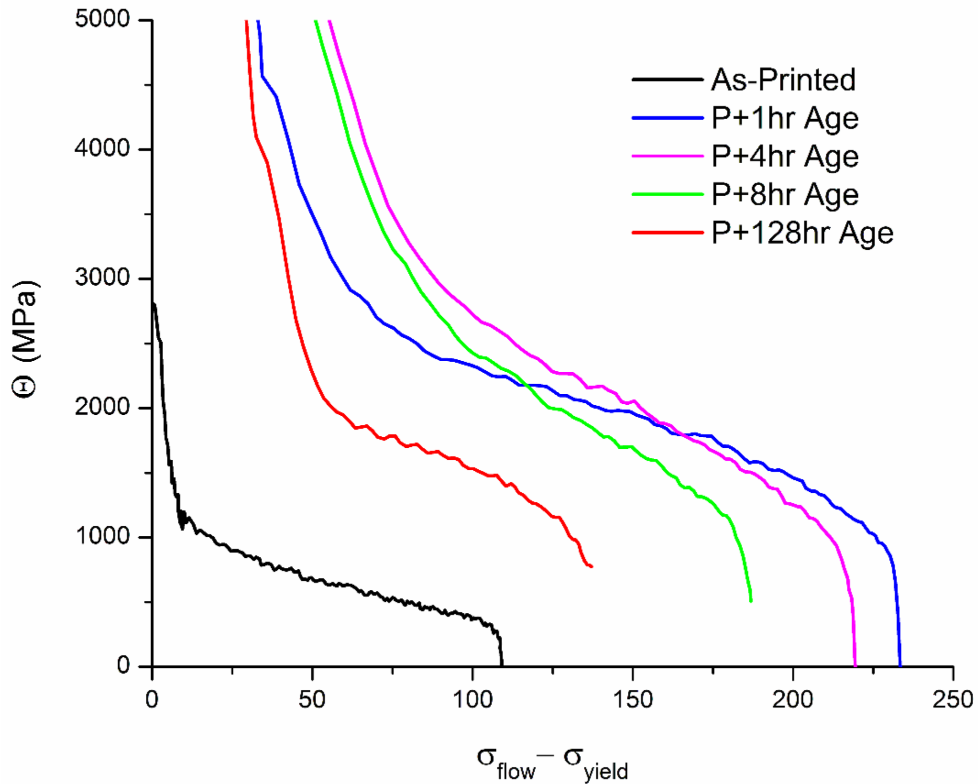

Figure 39. Work hardening rate versus the normalized flow stress for SLM C70250 at various stages of aging.

In addition to dislocation plasticity, deformation twinning has been observed in Cu-Ni-Si-Mg alloys as well as other copper alloys.[75, 100, 101] Figure 40 shows LOM and EBSD observation of deformation twins in the vicinity of the fracture surface in a peak aged sample that has been tensile tested to failure (the fracture surface is at the top of the micrograph). The peak aged condition has the highest concentration of deformation twinning compared to the as-printed or over aged sample. Deformation twinning can occur in copper alloys when the barrier for slip is higher than that of twinning (in this case due to the presence of precipitates). It is accompanied by an increase in strength and in the work hardening rate due to subdivision of the

grains.[75, 100] The presence of deformation twinning therefore obscures utilization of the work hardening rate as an indicator of dislocation-particle interaction mechanism.

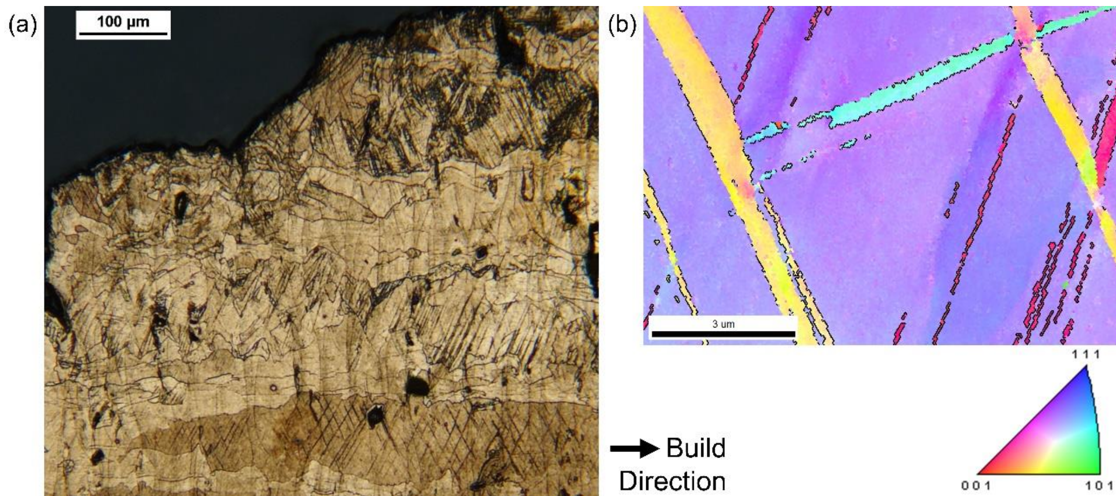

Figure 40. (a) LOM observation and (b) EBSD analysis of deformation twinning observed in a peak aged SLM C70250 sample deformed in a uniaxial tensile test to failure. The black lines in (b) outline FCC twin boundaries.

The variance in the amount of twinning observed implies that twinning is affected by the size/distribution of the strengthening precipitates. As precipitation occurs the solute concentration in the matrix decreases and the stacking fault energy is expected to increase, both of which should decrease the likelihood of deformation twinning. However, the formation of the precipitates also increases the strength significantly which has been suggested as the reason twinning occurs in the aged conditions but not in the solution treated condition. Twinning observed in FCC metals at high strains after significant work hardening is explained by a similar phenomenon, i.e. a

barrier exists for continued slip to accommodate the deformation so twinning begins to occur.[75, 101]

The results show that the mechanical response of SLM C70250 throughout aging is quite complex. Several mechanisms are involved in the material's response to stress after aging, and the contribution of different mechanisms evolves as aging progresses. This is likely the reason there is such a broad range of aging times where the peak strength of the alloy seems to remain constant, despite the fact that the strengthening precipitates are increasing in size. The broad range of peak properties means that precise control during post-processing is not necessary for maximizing strength, and that it is acceptable to choose long aging times that increase the electrical conductivity without significant loss of strength.

This investigation has shown that alloy C70250 is well suited for the SLM process. The alloy achieves a good as-printed density, does not require an intermediate solution heat treatment, and as a result achieves high strength and conductivity when aged directly after fabrication. The most unique aspect of C70250 fabricated via SLM compared to traditional manufacturing techniques is the presence of nanometer scale oxide particles. Fabricating alloy C70250 via SLM results in a hybrid precipitation and oxide dispersion strengthened alloy. Although it is unexpected, the oxide particles are well distributed in the microstructure due to the unique nature of SLM, and their size is similar to oxide particles in dispersion strengthened copper alloys

currently used commercially.[16] The increase in yield strength from the oxide particles in this study was quite low compared to the other mechanisms discussed (42 MPa estimated increase from oxide particles compared to the experimentally measured 362 MPa increase from other mechanisms during aging) due to the low volume fraction. However, there are many possibilities to intentionally introduce more oxygen to the material during processing. Examples include mixing in oxygen rich powder or controlling the fabrication atmosphere. Increasing the volume fraction of oxide particles in the structure via SLM could further improve the room temperature and high temperature mechanical properties of the alloy. Future investigations can utilize the findings of this work as a basis for creating new SLM-specific high performance copper alloys with novel properties.

4.6 Conclusions

The mechanical properties of selective laser melted C70250 during aging at 723 K (450 °C) were investigated. Based on a combination of mechanical testing and electron microscopy characterization, the following conclusions were reached with regards to SLM C70250:

1. Samples of SLM C70250 around 98 percent dense can be produced and aged directly from the as-printed condition to reach peak strength. Grains grow epitaxially from prior build layers and a fine cellular substructure exists throughout the material.

2. Aging at 723 K (450 °C) improves the mechanical properties drastically with a maximum yield strength of 596 MPa compared to the as-printed yield strength of 226 MPa. After aging for 128 hours there is a drop in yield strength to 546 MPa.
3. The conductivity in the as-printed condition is 15%IACS and increases during aging. The conductivity in the peak age and over age condition is 34.2 and 43.2 %IACS, respectively.
4. Nanometer-scale silicon-rich oxide particles exist throughout the material and persist during aging. Their contribution to strengthening is predicted to be far less significant than the strengthening precipitates due to their low volume fraction and large size.
5. Several strengthening mechanisms appear to be active to varying degrees as aging progresses which results in a broad range of aging time where nearly the peak properties are attained.

4.7 Acknowledgements

The authors would like to thank TE Connectivity, ltd. for the funding of this research along with collaboration throughout the study. The authors thank the Loewy Family Foundation for financially supporting this project and two of the authors, (Anthony P. Ventura) as a Loewy Graduate Fellow and (Wojciech Z. Misiolek) through the Loewy Professorship at Lehigh University. Lastly, the authors thank the W. M. Keck Foundation for financial support of Dr. Christopher J. Marvel.

CHAPTER 5

SUMMARY

5.1 Significance of Findings

A fundamental understanding of the microstructure-property relationship in two SLM copper alloys has been established. Copper alloy components were successfully fabricated with a wide range of properties that were tunable with post-process heat treatment. The attractive physical properties of copper alloys are invaluable in a wide range of electrical and thermal applications. Implementation of SLM is expanding and SLM copper alloys must be developed to meet the challenges associated with new applications. Utilizing this work, single phase and precipitation hardened copper alloys may be processed in currently available commercial SLM setups. The findings establish attainable physical and electrical properties, as well as processing conditions required to achieve those properties. The immediate impact then serves to fill the gap in literature and industry on the production of copper alloy components in SLM and their associated physical properties. Beyond the directly valuable practical knowledge established by this research, broader significance exists related to the implications of the unique microstructural features in SLM copper alloys. Characterization of the as-printed and heat treated microstructures of the two alloys presents a foundation enabling the development of SLM-specific copper alloys. Future investigations can utilize knowledge of the expected grain morphology,

chemical segregation, and oxygen incorporation to optimize the alloy composition and processing parameters.

5.2 Future Work

This research is a balance between practical engineering findings pertaining to the properties and processing of SLM copper alloys and a scientific understanding of the physical metallurgy mechanisms behind those properties. Based on the findings, several future investigations are possible that would advance knowledge and implementation of copper alloys in SLM. Potential future research includes short term studies that would facilitate understanding and commercial use of either alloy characterized in this study, as well as long term projects that would have much wider reaching implications in developing entirely new SLM copper alloys. Some of the most beneficial possibilities for future research that build upon this investigation are presented below.

5.2.1 Fabrication Parameters

Utilizing this investigation as a baseline, there are numerous possibilities for investigating the microstructural/performance effect of different processing parameters of the two alloys investigated in this study. The SLM processing parameters were held constant after some optimization for both alloys studied in this work, and maximum part densities were around 97-98%. Process parameters have a drastic effect on the as-printed density and microstructure which can then affect further post-processing. There is a

staggering number of processing variables that can be altered in an SLM unit. Furthermore, there are differences in fabrication between various machine manufacturers. The following studies could be conducted to build knowledge and potentially improve performance of either alloy studied in this research:

1. Further optimization of the laser parameters may lead to improved density. The role of laser power, scan strategy/geometry, and layer thickness could be investigated in combination with micro-CT density measurements. The results would enable a better understanding of the pore structures in SLM copper alloy and aid in eliminating or controlling the porosity.
2. At the maximum attainable density of SLM copper alloys in these investigations, there is a range of satisfactory processing parameters (example shown in Figure 41). Literature has established that laser parameters can directly control solidification and therefore the microstructure. Understanding the changes in microstructure in this range of acceptable density would provide another tool in controlling part properties (for example by controlling microstructural texture for more/less isotropic properties).

5.2.2 Post-Processing and Other Mechanical Property Metrics

Annealing heat treatments and aging heat treatments were studied, however other possible post-processing studies that would affect the microstructure and therefore the properties of SLM copper components.

1. For Cu-4.3%Sn, annealing at 600°C for 1 hour produced a microstructure in the intermediate stages of recrystallization, while annealing for 1 hour at 900°C produced a fully recrystallized structure with significant grain growth. Although a wide range of properties was established, the kinetics of annealing and recrystallization directly after printing are not fully understood. Expanding the study to different temperatures and times would give a more complete understanding of heat treatment of SLM copper alloys.
2. The most common aging temperature for the wrought counterpart was investigated for SLM C70250. To facilitate processing, higher aging temperatures or dual-aging treatments may be employed to lower aging time and streamline processing. An investigation of the aging response and precipitation process of SLM C70250 under different aging conditions is integral to determining the ideal industrial processing conditions of SLM C70250.
3. Hot Isostatic Pressing (HIP) is commonly employed in structure-critical components made by SLM to close internal porosity and improve performance, particularly in fatigue scenarios. However, due to the high temperature, HIP can drastically change the microstructure. The relationship between HIP densification, microstructural change, and further aging heat treatments will require investigation to achieve full density copper SLM components.

4. Relatively simple (room temperature, uniaxial) mechanical properties were the primary metric for performance in this investigation. For applications at elevated temperature or under cyclic loading, which is relatively common for copper alloys, additional testing is required to gage the performance of SLM components. The most relevant tests include stress relaxation rate investigations and fatigue testing. These tests will establish performance limits for the alloys investigated in this study and potentially identify different optimal post-processing depending on the most important performance metric.

5.2.3 Copper Alloy Development for SLM

Large scale projects based on the unique microstructural observations in this study have the most potential for building from this work and advancing SLM of copper alloys. Although literature has shown some degree of oxide particle incorporation in iron alloys, this work has demonstrated that the phenomenon occurs in copper alloys and the oxide particles are well suited to dispersion strengthening. The incorporation of nanometer scale oxide particles into SLM copper alloys provides a pathway for creating hybrid strengthened copper alloys. The following investigations have the potential to create a novel set of copper alloys that exploit the unique processing conditions of SLM:

1. In alloy C70250, nanometer scale oxide particles from fabrication remained stable during aging, but their volume fraction and hence

strengthening effect was low. Investigations to understand formation of oxide particles in copper SLM and the key variables controlling their morphology could increase the level of oxide dispersion strengthening and improve the mechanical properties of SLM precipitation hardened copper alloys without significant loss of conductivity. Investigation could be carried out on C70250 by introducing oxygen, either through the build chamber atmosphere or incorporation of oxygen rich powder particles to understand if the volume fraction can be improved while retaining the small size and uniform distribution.

2. Given that nanometer scale oxide particles were present in both alloys in this study, oxide particle formation in-situ is likely possible in other copper alloys. Several other precipitation strengthening copper alloys exist that contain high oxygen affinity alloying elements (e.g. Cu-Ti, Cu-Cr) that may be able to utilize the phenomenon observed in this investigation to achieve novel properties via SLM. Since some of the alloying elements will be reacting with oxygen, tuning of the chemical composition will likely be required for optimum performance.

REFERENCES

[1] C. W. Hull, “Apparatus for production of three-dimensional objects by stereolithography,” US4575330 A, 11-Mar-1986.

[2] I. Gibson, D. W. Rosen, and B. Stucker, *Additive Manufacturing Technologies: Rapid Prototyping to Direct Digital Manufacturing*, 2010 edition. London ; New York: Springer, 2009.

[3] S. Kalpakjian and S. Schmid, *Manufacturing Processes for Engineering Materials*, 5th ed. Prentice Hall, 2007.

[4] E. Herderick, “Additive Manufacturing of Metals: A Review,” in *Additive Manufacturing of Metals*, 2011, vol. 2011.

[5] S. H. Huang, P. Liu, A. Mokasdar, and L. Hou, “Additive manufacturing and its societal impact: a literature review,” *Int J Adv Manuf Technol*, vol. 67, no. 5–8, pp. 1191–1203, Jul. 2013.

[6] R. M. German, *Powder Metallurgy & Particulate Materials Processing*. Princeton, New Jersey: Metal Powder Industry, 2005.

[7] W. J. Sames, F. A. List, S. Pannala, R. R. Dehoff, and S. S. Babu, “The metallurgy and processing science of metal additive manufacturing,” *International Materials Reviews*, vol. 61, no. 5, pp. 315–360, Jul. 2016.

[8] M. Rombouts, J.-P. Kruth, L. Froyen, and P. Mercelis, “Fundamentals of selective laser melting of alloyed steel powders,” *CIRP Annals-Manufacturing Technology*, vol. 55, no. 1, pp. 187–192, 2006.

[9] L.-C. Zhang and H. Attar, “Selective laser melting of titanium alloys and titanium matrix composites for biomedical applications: a review,” *Advanced Engineering Materials*, 2015.

[10] D. Bourell, “Perspectives on Additive Manufacturing,” *Annual Review of Materials Research*, vol. 46, pp. 1–18, 2016.

[11] D. D. Gu, W. Meiners, K. Wissenbach, and R. Poprawe, “Laser additive manufacturing of metallic components: materials, processes and mechanisms,” *International Materials Reviews*, Nov. 2013.

[12] E. O. Olakanmi, R. F. Cochrane, and K. W. Dalgarno, “A review on selective laser sintering/melting (SLS/SLM) of aluminium alloy powders: Processing, microstructure, and properties,” *Progress in Materials Science*, vol. 74, pp. 401–477, 2015.

[13] M. Agarwala, D. Bourell, J. Beaman, H. Marcus, and J. Barlow, “Direct selective laser sintering of metals,” *Rapid Prototyping Journal*, vol. 1, no. 1, pp. 26–36, 1995.

[14] W. E. Frazier, “Metal Additive Manufacturing: A Review,” *J. of Materi Eng and Perform*, vol. 23, no. 6, pp. 1917–1928, Jun. 2014.

[15] T. Vilaro, C. Colin, J.-D. Bartout, L. Nazé, and M. Sennour, “Microstructural and mechanical approaches of the selective laser melting process applied to a nickel-base superalloy,” *Materials Science and Engineering: A*, vol. 534, pp. 446–451, 2012.

[16] J. R. Davis, *ASM Specialty Handbook: Copper and Copper Alloys*, 1st ed. Materials Park, OH: ASM International, 2001.

[17] A. P. Ventura, C. A. Wade, G. Pawlikowski, M. Bayes, M. Watanabe, and W. Z. Misiolek, “Mechanical Properties and Microstructural Characterization of Cu-4.3 Pct Sn Fabricated by Selective Laser Melting,” *Metall and Mat Trans A*, vol. 48, no. 1, pp. 178–187, Jan. 2017.

[18] C. R. Deckard, J. J. Beaman, and J. F. Darrah, “Method for selective laser sintering with layerwise cross-scanning,” US5155324 A, 13-Oct-1992.

[19] J. Kruth, P. Mercelis, J. Van Vaerenbergh, L. Froyen, and M. Rombouts, “Binding mechanisms in selective laser sintering and selective laser melting,” *Rapid Prototyping Journal*, vol. 11, no. 1, pp. 26–36, Feb. 2005.

[20] A. V. Gusarov and J.-P. Kruth, “Modelling of radiation transfer in metallic powders at laser treatment,” *International Journal of Heat and Mass Transfer*, vol. 48, no. 16, pp. 3423–3434, Jul. 2005.

[21] N. K. Tolochko, Y. V. Khlopkov, S. E. Mozzharov, M. B. Ignatiev, T. Laoui, and V. I. Titov, “Absorptance of powder materials suitable for laser sintering,” *Rapid Prototyping Journal*, vol. 6, no. 3, pp. 155–161, Sep. 2000.

[22] T. T. Roehling *et al.*, “Modulating laser intensity profile ellipticity for microstructural control during metal additive manufacturing,” *Acta Materialia*, vol. 128, pp. 197–206, Apr. 2017.

[23] T. Niendorf, S. Leuders, A. Riemer, H. A. Richard, T. Tröster, and D. Schwarze, “Highly Anisotropic Steel Processed by Selective Laser Melting,” *Metallurgical and Materials Transactions B*, vol. 44, no. 4, pp. 794–796, Aug. 2013.

[24] L. Thijs, K. Kempen, J.-P. Kruth, and J. Van Humbeeck, “Fine-structured aluminium products with controllable texture by selective laser melting of pre-alloyed AlSi10Mg powder,” *Acta Materialia*, vol. 61, no. 5, pp. 1809–1819, Mar. 2013.

[25] D. A. Ramirez *et al.*, “Novel precipitate–microstructural architecture developed in the fabrication of solid copper components by additive manufacturing using electron beam melting,” *Acta Materialia*, vol. 59, no. 10, pp. 4088–4099, Jun. 2011.

[26] M. A. Lodes, R. Guschlbauer, and C. Körner, “Process development for the manufacturing of 99.94% pure copper via selective electron beam melting,” *Materials Letters*, vol. 143, pp. 298–301, Mar. 2015.

[27] EOS, “EOSINT M Materials for Direct Metal Laser-Sintering.” EOS, 2007.

[28] L.-E. Loh *et al.*, “Numerical investigation and an effective modelling on the Selective Laser Melting (SLM) process with aluminium alloy 6061,” *International Journal of Heat and Mass Transfer*, vol. 80, pp. 288–300, Jan. 2015.

[29] L. Thijs, F. Verhaeghe, T. Craeghs, J. V. Humbeeck, and J.-P. Kruth, “A study of the microstructural evolution during selective laser melting of Ti–6Al–4V,” *Acta Materialia*, vol. 58, no. 9, pp. 3303–3312, May 2010.

[30] L. E. Murr *et al.*, “Microstructures and Properties of 17-4 PH Stainless Steel Fabricated by Selective Laser Melting,” *Journal of Materials Research and Technology*, vol. 1, no. 3, pp. 167–177, Oct. 2012.

[31] E. Yasa and J.-P. Kruth, “Microstructural investigation of Selective Laser Melting 316L stainless steel parts exposed to laser re-melting,” *Procedia Engineering*, vol. 19, pp. 389–395, 2011.

[32] B. Song *et al.*, “Differences in microstructure and properties between selective laser melting and traditional manufacturing for fabrication of metal parts: A review,” *Frontiers of Mechanical Engineering*, vol. 10, no. 2, pp. 111–125, Jun. 2015.

[33] S. Kou, *Welding Metallurgy*. John Wiley & Sons, 2003.

[34] A. A. Antonysamy, J. Meyer, and P. B. Prangnell, “Effect of build geometry on the β-grain structure and texture in additive manufacture of Ti6Al4V by selective electron beam melting,” *Materials Characterization*, vol. 84, pp. 153–168, Oct. 2013.

[35] T. Bormann, B. Müller, M. Schinhammer, A. Kessler, P. Thalmann, and M. de Wild, “Microstructure of selective laser melted nickel–titanium,” *Materials Characterization*, vol. 94, pp. 189–202, Aug. 2014.

[36] W. Shifeng, L. Shuai, W. Qingsong, C. Yan, Z. Sheng, and S. Yusheng, “Effect of molten pool boundaries on the mechanical properties of selective laser melting parts,” *Journal of Materials Processing Technology*, vol. 214, no. 11, pp. 2660–2667, Nov. 2014.

[37] J. Donoghue, A. A. Antonysamy, F. Martina, P. A. Colegrove, S. W. Williams, and P. B. Prangnell, “The effectiveness of combining rolling deformation with Wire–Arc Additive Manufacture on β-grain refinement and texture modification in Ti–6Al–4V,” *Materials Characterization*, vol. 114, pp. 103–114, Apr. 2016.

[38] B. Vrancken, L. Thijs, J.-P. Kruth, and J. Van Humbeeck, “Heat treatment of Ti6Al4V produced by Selective Laser Melting: Microstructure and mechanical properties,” *Journal of Alloys and Compounds*, vol. 541, pp. 177–185, Nov. 2012.

[39] B. Vrancken, R. Wauthlé, J.-P. Kruth, and J. Van Humbeeck, “Study of the influence of material properties on residual stress in selective laser melting,” in *Proceedings of the solid freeform fabrication symposium*, 2013, p. 393.

[40] W. M. Tucho, P. Cuvillier, A. Sjolyst-Kverneland, and V. Hansen, “Microstructure and hardness studies of Inconel 718 manufactured by selective laser melting before and after solution heat treatment,” *Materials Science and Engineering: A*, vol. 689, pp. 220–232, Mar. 2017.

[41] A. B. Spierings, T. L. Starr, and K. Wegener, “Fatigue performance of additive manufactured metallic parts,” *Rapid Prototyping Journal*, vol. 19, no. 2, pp. 88–94, Mar. 2013.
[42] P. Mercelis and J.-P. Kruth, “Residual stresses in selective laser sintering and selective laser melting,” *Rapid Prototyping Journal*, vol. 12, no. 5, pp. 254–265, 2006.
[43] W. Gai and N. Sammes, *An Introduction to Electronic and Ionic Materials*. Hackensack, NJ: World Scientific Publishing Co., 1999.
[44] W. Callister and D. Rethwisch, *Fundamentals of Materials Science and Engineering: An integrated approach*, 3rd ed. Danvers, MA: John Wiley and Sons, Inc., 2008.
[45] R. W. Hertzberg, R. P. Vinci, and J. L. Hertzberg, *Deformation and Fracture Mechanics of Engineering Materials*, 5 edition. Hoboken, NJ: Wiley, 2012.
[46] U. F. Kocks and H. Mecking, “Physics and phenomenology of strain hardening: the FCC case,” *Progress in Materials Science*, vol. 48, no. 3, pp. 171–273, Jan. 2003.
[47] U. Kocks, “Strain Hardening and ‘Strain-Rate Hardening,’” in *Mechanical Testing for Deformation Model Development*, R. Rohde and J. Swearengen, Eds. 100 Barr Harbor Drive, PO Box C700, West Conshohocken, PA 19428-2959: ASTM International, 1982, pp. 121-121–18.
[48] L. M. Cheng, W. J. Poole, J. D. Embury, and D. J. Lloyd, “The influence of precipitation on the work-hardening behavior of the aluminum alloys AA6111 and AA7030,” *Metall and Mat Trans A*, vol. 34, no. 11, pp. 2473–2481, Nov. 2003.
[49] T. Gladman, “Precipitation hardening in metals,” *Materials Science and Technology*, vol. 15, no. 1, pp. 30–36, Jan. 1999.
[50] E. Botcharova, J. Freudenberger, and L. Schultz, “Mechanical and electrical properties of mechanically alloyed nanocrystalline Cu–Nb alloys,” *Acta Materialia*, vol. 54, no. 12, pp. 3333–3341, Jul. 2006.
[51] P. V. Andrews, M. B. West, and C. R. Robeson, “The effect of grain boundaries on the electrical resistivity of polycrystalline copper and aluminium,” *Philosophical Magazine*, vol. 19, no. 161, pp. 887–898, 1969.
[52] K. Schmidtke, F. Palm, A. Hawkins, and C. Emmelmann, “Process and Mechanical Properties: Applicability of a Scandium modified Al-alloy for Laser Additive Manufacturing,” *Physics Procedia*, vol. 12, pp. 369–374, Jan. 2011.
[53] A. B. Spierings, K. Dawson, M. Voegtlin, F. Palm, and P. J. Uggowitzer, “Microstructure and mechanical properties of as-processed scandium-modified aluminium using selective laser melting,” *CIRP Annals - Manufacturing Technology*, vol. 65, no. 1, pp. 213–216, 2016.
[54] N. Ordás, L. C. Ardila, I. Iturriza, F. Garcianda, P. Álvarez, and C. García-Rosales, “Fabrication of TBMs cooling structures demonstrators using

additive manufacturing (AM) technology and HIP," *Fusion Engineering and Design*, vol. 96–97, pp. 142–148, Oct. 2015.
[55] X. P. Li *et al.*, "A selective laser melting and solution heat treatment refined Al–12Si alloy with a controllable ultrafine eutectic microstructure and 25% tensile ductility," *Acta Materialia*, vol. 95, pp. 74–82, Aug. 2015.
[56] G. Kasperovich and J. Hausmann, "Improvement of fatigue resistance and ductility of TiAl6V4 processed by selective laser melting," *Journal of Materials Processing Technology*, vol. 220, pp. 202–214, Jun. 2015.
[57] S. Kasap, *Principles of Electronic Materials and Devices*, 3 edition. Boston etc.: McGraw-Hill Education, 2005.
[58] P. W. Taubenblat, "Copper: Selection of High Conductivity Alloys," in *Encyclopedia of Materials Science and Engineering*, vol. 2, Pergamon Press and the MIT Press, 1986, pp. 863–866.
[59] E. Nembach, *Particle Strengthening of Metals and Alloys*, 1 edition. New York: Wiley-VCH, 1996.
[60] H. Herman, J. B. Cohen, and M. E. Fine, "Formation and reversion of Guinier-Preston zones in Al-5.3 at.% Zn," *Acta Metallurgica*, vol. 11, no. 1, pp. 43–56, Jan. 1963.
[61] J. Miyake and M. E. Fine, "Electrical conductivity versus strength in a precipitation hardened alloy," *Acta metallurgica et materialia*, vol. 40, no. 4, pp. 733–741, 1992.
[62] D. A. Porter and K. E. Easterling, *Phase Transformations in Metals and Alloys, Third Edition (Revised Reprint)*. CRC Press, 1992.
[63] T. Boegelein, S. N. Dryepondt, A. Pandey, K. Dawson, and G. J. Tatlock, "Mechanical response and deformation mechanisms of ferritic oxide dispersion strengthened steel structures produced by selective laser melting," *Acta Materialia*, vol. 87, pp. 201–215, 2015.
[64] K. Saeidi, X. Gao, Y. Zhong, and Z. J. Shen, "Hardened austenite steel with columnar sub-grain structure formed by laser melting," *Materials Science & Engineering: A*, vol. 625, pp. 221–229, 2015.
[65] H. Pops, "Copper Applications in Metallurgy of Copper & Copper Alloys." Copper Development Association, Dec-1997.
[66] Corson M. G., "Copper Hardened by a New Method," *Zeitschrift fur Metalkunde*, vol. 19, p. 370.
[67] ASTM International, "ASTM B422/B422M-15 Standard Specification for Copper-Aluminum-Silicon-Cobalt Alloy, Copper-Nickel-Silicon-Magnesium Alloy, Copper-Nickel-Silicon Alloy, Copper-Nickel-Aluminum-Magnesium Alloy, and Copper-Nickel-Tin Alloy Sheet and Strip." ASTM International, 2015.
[68] S. A. Lockyer and F. W. Noble, "Precipitate structure in a Cu-Ni-Si alloy," *JOURNAL OF MATERIALS SCIENCE*, vol. 29, no. 1, pp. 218–226, Jan. 1994.
[69] C. B. Carter and D. B. Williams, Eds., *Transmission Electron Microscopy*. Cham: Springer International Publishing, 2016.

[70] Y. Jia, M. Wang, C. Chen, Q. Dong, S. Wang, and Z. Li, “Orientation and diffraction patterns of δ-Ni2Si precipitates in Cu–Ni–Si alloy,” *Journal of Alloys and Compounds*, vol. 557, pp. 147–151, Apr. 2013.
[71] S. a. Lockyer and F. w. Noble, “Fatigue of precipitate strengthened Cu–Ni–Si alloy,” *Mater. Sci. Technol.*, vol. 15, no. 10, pp. 1147–1153, Oct. 1999.
[72] D. . Zhao, Q. . Dong, P. Liu, B. . Kang, J. . Huang, and Z. . Jin, “Structure and strength of the age hardened Cu–Ni–Si alloy,” *Materials Chemistry and Physics*, vol. 79, no. 1, pp. 81–86, Mar. 2003.
[73] D. Zhao, Q. M. Dong, P. Liu, B. X. Kang, J. L. Huang, and Z. H. Jin, “Aging behavior of Cu–Ni–Si alloy,” *Materials Science and Engineering: A*, vol. 361, no. 1–2, pp. 93–99, Nov. 2003.
[74] T. Hu, J. H. Chen, J. Z. Liu, Z. R. Liu, and C. L. Wu, “The crystallographic and morphological evolution of the strengthening precipitates in Cu–Ni–Si alloys,” *Acta Materialia*, vol. 61, no. 4, pp. 1210–1219, Feb. 2013.
[75] A. Araki, W. J. Poole, E. Kobayashi, and T. Sato, “Twinning Induced Plasticity and Work Hardening Behavior of Aged Cu-Ni-Si Alloy,” *MATERIALS TRANSACTIONS*, 2014.
[76] J. F. Wang, S. G. Jia, S. H. Chen, K. X. Song, P. Liu, and G. J. Yu, “Effect of Aging Precipitation on Properties of Cu-Ni-Si-Mg Alloy,” *Advanced Materials Research*, vol. 197–198, pp. 1315–1320, Feb. 2011.
[77] S. Suzuki, N. Shibutani, K. Mimura, M. Isshiki, and Y. Waseda, “Improvement in strength and electrical conductivity of Cu–Ni–Si alloys by aging and cold rolling,” *Journal of Alloys and Compounds*, vol. 417, no. 1–2, pp. 116–120, Jun. 2006.
[78] F. Huang, J. Ma, H. Ning, Y. Cao, and Z. Geng, “Precipitation in Cu–Ni–Si–Zn alloy for lead frame,” *Materials Letters*, vol. 57, no. 13–14, pp. 2135–2139, Apr. 2003.
[79] S. Semboshi, T. Nishida, and H. Numakura, “Microstructure and mechanical properties of Cu–3 at.% Ti alloy aged in a hydrogen atmosphere,” *Materials Science and Engineering: A*, vol. 517, no. 1–2, pp. 105–113, Aug. 2009.
[80] S. Z. Han *et al.*, “Increasing toughness by promoting discontinuous precipitation in Cu–Ni–Si alloys,” *Philosophical Magazine Letters*, vol. 96, no. 5, pp. 196–203, May 2016.
[81] D. B. Williams and E. P. Butler, “Grain boundary discontinuous precipitation reactions,” *International Metals Reviews*, vol. 26, no. 1, pp. 153–183, Jan. 1981.
[82] J. D. Nystrom, T. M. Pollock, W. H. Murphy, and A. Garg, “Discontinuous cellular precipitation in a high-refractory nickel-base superalloy,” *Metallurgical and Materials Transactions A*, vol. 28, no. 12, pp. 2443–2452, Dec. 1997.
[83] S. R. Pogson, P. Fox, C. J. Sutcliffe, and W. O’Neill, “The production of copper parts using DMLR,” *Rapid Prototyping Journal*, Apr. 2013.

[84] T. A. Kals and R. Eckstein, “Miniaturization in sheet metal working,” *Journal of Materials Processing Technology*, vol. 103, no. 1, pp. 95–101, Jun. 2000.
[85] C. H. Suh, Y.-C. Jung, and Y. S. Kim, “Effects of thickness and surface roughness on mechanical properties of aluminum sheets,” *Journal of Mechanical Science and Technology*, vol. 24, no. 10, pp. 2091–2098, Oct. 2010.
[86] H. J. McQueen and W. J. M. Tegart, “The Deformation of Metals at High Temperatures,” *Scientific American*, vol. 232, no. 4, pp. 116–125, Apr. 1975.
[87] H. Ellingham, “Reducibility of Oxides and Sulphides in Metallurgical Processes,” *Journal of the Society of Chemical Industry*, vol. 63, no. 5, pp. 125–160, May 1944.
[88] M. K. Thompson *et al.*, “Design for Additive Manufacturing: Trends, opportunities, considerations, and constraints,” *CIRP Annals - Manufacturing Technology*, vol. 65, no. 2, pp. 737–760, 2016.
[89] J. Yang, H. Yu, J. Yin, M. Gao, Z. Wang, and X. Zeng, “Formation and control of martensite in Ti-6Al-4V alloy produced by selective laser melting,” *Materials & Design*, vol. 108, pp. 308–318, Oct. 2016.
[90] P. Stadelmann, *JEMS-SAAS*. .
[91] M. Watanabe and D. B. Williams, “The quantitative analysis of thin specimens: a review of progress from the Cliff-Lorimer to the new ζ-factor methods,” *Journal of Microscopy*, vol. 221, no. 2, pp. 89–109, Feb. 2006.
[92] V. C. Srivastava, A. Schneider, V. Uhlenwinkel, and K. Bauckhage, “Effect of thermomechanical treatment on spray formed Cu – Ni – Si alloy,” *Materials Science and Technology*, vol. 20, no. 7, pp. 839–848, Jul. 2004.
[93] C. Watanabe, H. Hiraide, Z. Zhang, and R. Monzen, “Microstructure and Mechanical Properties of Cu-Ni-Si Alloys,” *Journal of the Society of Materials Science, Japan*, vol. 54, no. 7, pp. 717–723, 2005.
[94] J. DuPont, “Fundamentals of Weld Solidification,” in *Welding Fundamentals and Processes*, vol. 6A, ASM International, 2011, pp. 96–114.
[95] Z. Sun, X. Tan, S. B. Tor, and W. Y. Yeong, “Selective laser melting of stainless steel 316L with low porosity and high build rates,” *Materials & Design*, vol. 104, pp. 197–204, Aug. 2016.
[96] S. Semboshi, S. Sato, A. Iwase, and T. Takasugi, “Discontinuous precipitates in age-hardening CuNiSi alloys,” *Materials Characterization*, vol. 115, pp. 39–45, May 2016.
[97] T. Gladman, *The physical metallurgy of microalloyed steels*. Institute of Materials, 1997.
[98] W. J. Poole, X. Wang, D. J. Lloyd, and J. D. Embury, “The shearable–non-shearable transition in Al–Mg–Si–Cu precipitation hardening alloys:

implications on the distribution of slip, work hardening and fracture," *Philosophical Magazine*, vol. 85, no. 26–27, pp. 3113–3135, Sep. 2005.
[99] A. Kelly and S. R. Nicholson, *Strengthening methods in crystals*. Halstead Press Division, Wiley, 1972.
[100] A. Rohatgi, K. S. Vecchio, and G. T. Gray, "The influence of stacking fault energy on the mechanical behavior of Cu and Cu-Al alloys: Deformation twinning, work hardening, and dynamic recovery," *Metall and Mat Trans A*, vol. 32, no. 1, pp. 135–145, Jan. 2001.
[101] M. A. Meyers, O. Vöhringer, and V. A. Lubarda, "The onset of twinning in metals: a constitutive description," *Acta Materialia*, vol. 49, no. 19, pp. 4025–4039, Nov. 2001.
[102] C. A. Schneider, W. S. Rasband, and K. W. Eliceiri, "NIH Image to ImageJ: 25 years of image analysis," *Nature Methods*, vol. 9, no. 7, pp. 671–675, Jun. 2012.
[103] "Standard Test Methods for Tension Testing of Metallic Materials," ASTM International, 2016.
[104] G. F. V. Voort, *Metallography, Principles and Practice*. ASM International, 1984.
[105] D. Kiener, C. Motz, M. Rester, M. Jenko, and G. Dehm, "FIB damage of Cu and possible consequences for miniaturized mechanical tests," *Materials Science and Engineering: A*, vol. 459, no. 1–2, pp. 262–272, Jun. 2007.
[106] A. Genç, T. O. S. University, E. A. F. I. Inc, and T. O. S. University, "Post-FIB TEM Sample Preparation Using A Low Energy Argon Beam," *Microscopy and Microanalysis*, vol. 13, no. S02, Aug. 2007.

APPENDIX A

EXPANDED METHODS

A.1 Expanded Methods Introduction

Throughout this investigation, the experimental methods were refined to achieve optimal and reproducible results during observation and testing. Concise and standalone versions of the final methods suitable for publication are presented individually in Chapters 3 and 4 for the analyses of each particular alloy system. This appendix will primarily focus on covering the issues encountered in the design of the general methods of this body of work and discuss what was eventually determined to be the ideal procedure where challenges were encountered. As such, this section will contain images of samples that may contain artifacts, samples that may not suitable for investigation, and discussion of sub-optimal procedures for the purposes of avoiding such issues in similarly structured future investigations. Certain aspects of investigation that did not pose any substantial unique challenges, for example x-ray diffraction (XRD) and electron backscatter diffraction (EBSD), will not be discussed in great detail as the concise procedure and standard practice for those techniques are suitable for reproduction of the results. This section is in the frame of reference of the capabilities of Lehigh University's facilities at the time of this research. No particular distinction will be made between the two alloys in this appendix, as the procedures for

preparation, testing, and characterization discussed generally apply to both alloy systems.

A.2 SLM Process Parameters

Fabrication parameters are not directly addressed in this work in terms of their dynamic relationship with the finished components. The goal of this work was to understand the microstructure and mechanical properties of copper alloys fabricated via SLM. Therefore, the standard process for optimizing processing parameters to achieve maximum density was employed to fabricate samples for this investigation. After the parameter optimization, the fabrication process was fixed for all samples fabricated for further analysis (i.e. the contents of this research). SLM was completed off-site using an EOSINT M280 with a Yb-fiber laser and samples were received after optimization of the build parameters was completed independently by Tyco Electronics Corporation, a TE Connectivity company in Harrisburg, PA. The procedure for determining appropriate process parameters generally consists of printing a number of 1x1x1 cm^3 samples with varying build parameters and measuring the density via the Archimedes technique. Through a systematic investigation of the various processing variables, the ideal processing parameters are selected.

Figure 41 shoes the density versus the linear laser energy (laser power divided by scan speed) at various beam spot sizes for one of the alloys characterized in this study. Other processing variables were investigated that

are not shown in Figure 41 including scan spacing and contour scan offsets. The Archimedes measurements were compared to light optical measurements of porosity volume fraction. Five sample cross sections from the build direction approximately 10 x 3 mm^2 were analyzed in ImageJ software using the particle analyzer function.[102] The porosity measurements have low standard deviations (~0.3% of the measured values) and are in good agreement with the Archimedes measurements for samples around 98% theoretical density.

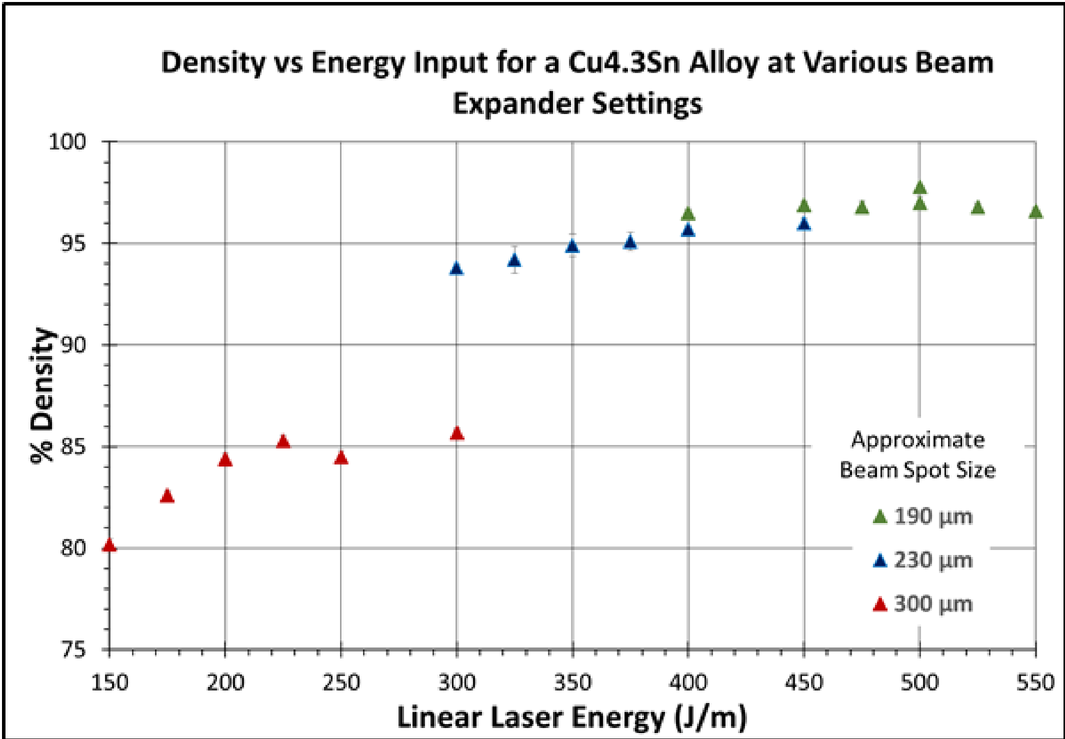

Figure 41. Density vs linear laser energy curve at various beam spot sizes. This data was utilized to select the ideal processing parameters for samples used in this study.

A.3 Heat Treatment

To avoid incorporation of oxygen into the samples during heat treatment, samples were heat treated in an inert atmosphere. Tube furnaces

generally provide the most control during heat treatment. In comparison to benchtop box furnaces, the heating rate is usually higher which allows for more precise control over temperature profiles. Additionally, the smaller furnace volume and better isolation from atmosphere results in a more stable heat treatment environment.

To control the heat treatment atmosphere, a rough vacuum pump is used to evacuate the tube furnace which has standard enclosures on each end connected to a gas-line system. The input of the tube furnace is connected to a regulator that controls the flow of a gas cylinder into the furnace; in this investigation argon was used exclusively, although any gas cylinder is compatible with the system. The backend system has check valves that can either connect the furnace to the vacuum pump, isolate the furnace (essentially closing the output end), or connect it to the exhaust hood. Prior to any heat treatment, the furnace is pressurized slightly (~1-2 psi) and all connections are tested for leaks and adjusted if necessary. Initial setup of the gas lines must be done carefully; only the furnace end-caps will be regularly removed for sample insertion, so all other connections are essentially static after initial setup. After samples are loaded into the center of the tube furnace, the purging procedure consists of six evacuation-argon backfill cycles to minimize the amount of oxygen present. During the final backfill, the furnace is isolated and allowed to reach an overpressure of about 1 psi. This is done to ensure that any small leaks in the system, usually at the furnace end caps, do

not pull in significant amounts of air from the room. Once the over-pressure is established, the output line is sent to the exhaust hood and flow regulator valves on the input and output lines must be adjusted to hold a constant overpressure during a crossflow of argon gas. This step generally only needs to be completed once per furnace setup, although if the peak temperature of the heat treatment changes significantly the flow regulators must be adjusted to find the new steady state.

Figure 42 shows a plot of temperature vs time indicating the time to reach peak temperature at maximum ramp rate for the tube furnaces used in this investigation. This preliminary step also serves to calibrate the furnace temperature; the small adjustments between 60-80 minutes serve to find the exact furnace setting for an actual internal temperature of 900°C (this step must be completed for every target temperature) as measured by a thermocouple. The maximum ramp rate achieved, and the final ramp rate that was used for all heat treatment, was 15°C per minute. The ramp rate and temperature calibration must be determined in the center of the furnace (the "hot zone"), under the gas conditions desired for final heat treatment, with a sample load (i.e. mass of samples in the hot zone) similar to actual experiments. If samples are larger or more samples must be inserted for heat treatment, the temperature fall off from the hot zone must be considered, but all samples in this investigation were small enough that this was not a factor.

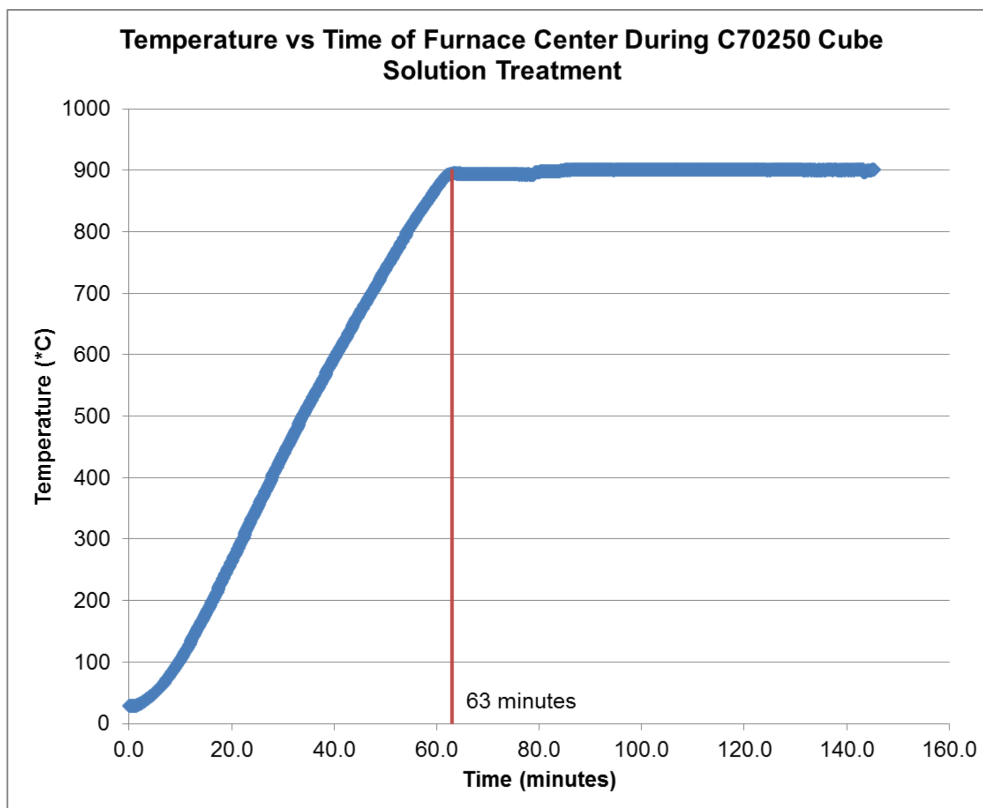

Figure 42. Temperature vs time plot showing the maximum ramp rate of the tube furnace used in this investigation during cross flow of argon gas.

All heat treatments in this investigation were done using the furnace temperature as a metric. This was deemed acceptable for this study since samples were relatively thin and copper is an excellent thermal conductor, so the samples were assumed to be at the temperature of the furnace. Preliminary comparisons between thermocouple-attached samples and isolated samples at 600°C to confirm this assumption did not show differences in temperature profile. It is possible to directly attach a thermocouple to all samples during heat treatment to have an exact temperature profile, but despite the additional information afforded by this approach it is not the ideal solution in practice for several reasons.

The furnace endcaps can typically only accommodate the incoming gas line and one thermocouple wire, so only one sample could be heat treated at a time and the throughput of samples would be dramatically reduced(for reference, 6 components were placed in the furnace for each heat treatment in Chapter 4). More importantly, inserting thermocouple wires into the furnace adds an additional location for oxygen from the air to seep into the furnace. Figure 43 shows the oxygen incorporation near the surface of a copper part heat treated at 900°C in a furnace with a thermocouple wire inserted for temperature calibration. Figure 44 however, shows a similar field of view for a sample heat treated under the same conditions with the exception that no thermocouple wire was inserted in the furnace. The amount of oxide near the surface is dramatically reduced by eliminating the additional seal for the thermocouple wire. Undoubtedly it is possible to improve the seal with the thermocouple and do all heat treatment with satisfactory atmosphere and precise information on sample temperature. However, it is generally not required if the furnace is diligently calibrated, sample dimensions are small, and heat treatment times are relatively long. If particularly short heat treatment times are required, for example if a fundamental study of early precipitation was the topic of investigation, closer monitoring of the sample temperature may be required.

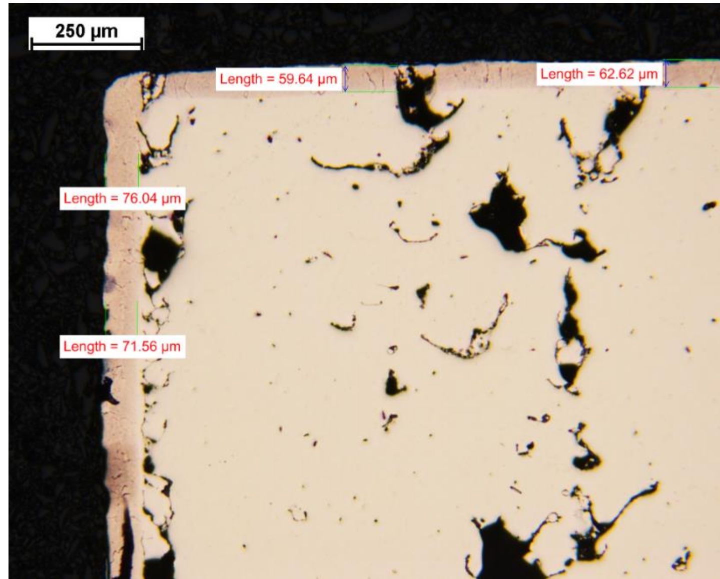

Figure 43. Oxygen incorporation near the surface of copper samples heat treated at 900°C in a tube furnace with an additional leak from thermocouple wire insertion.

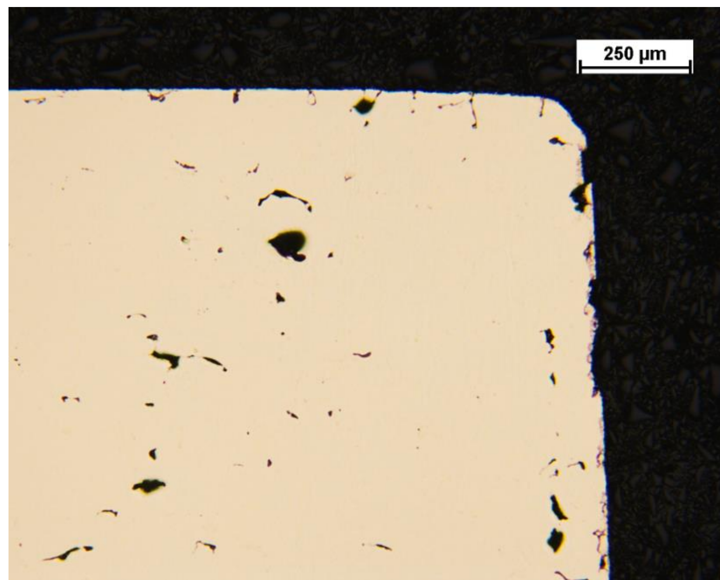

Figure 44. Micrograph of a copper sample heat treated in a furnace without a thermocouple wire inserted, no significant oxide formation is present.

A.4 Tensile Testing

Tensile testing was conducted on sub-size plate specimens per ASTM E-8 standards. Sub-size samples were utilized to maximize the number of specimens that could be printed on the SLM build plate. Some restrictions exist when utilizing sub size specimens, including the minimum overall length and the maximum thickness allowable. The minimum overall allowable length was used in this study to minimize sample size, but if possible longer is recommended per the specification to ensure axial loading. Additionally, the maximum thickness for sub-size plate samples is 6 mm. The samples in this investigation were primarily 3 mm thick, with some 1 mm thick samples for comparison, therefore no issues were encountered with this restriction. Extension rates, sometimes discussed in terms of the stressing rate and straining rate in the ASTM standard, in this study were based on method C which is a fixed percentage of the gauge length. Samples were held using mechanical wedge grips as deemed acceptable by the standard, there were no significant issues with grip slippage during testing. All data analysis to extract properties from the stress-strain curves was conducted after DIC processing per the ASTM standard methods. [103]

The engineering stress-strain curve was determined from a combination of a 30-kN load cell on the Instron load frame and digital image correlation (DIC) from Instron AVE2 optical extensometer video. The stress was calculated using the instantaneous load divided by the cross sectional area

that was measured using digital calipers for each sample. The AVE2 optical extensometers can measure the strain during the test using two macro dots at either end of the gauge length or with post-process DIC of a speckle pattern. DIC of a speckle pattern was the chosen method for this research. Macro-tracking allows for a strain rate controlled test, which is a significant advantage over speckle techniques. However, speckle patterns allow for investigation of the localized strain distribution which can be of particular interest in samples where defects or heterogeneity of the material leads to failure in a particular location. Additionally, due to the way the Instron software deals with tracking, if the macro-dot tracking fails at any point in the test, significant artifacts can develop in the stress strain curve. The load frame will switch to a fixed extension rate that is nominally the same as the current rate, eliminating the strain-rate controlled nature of the test for the duration. Thus, speckle patterning with an easily controlled and repeatable fixed extension rate was the chosen method for tensile testing to minimize variation between samples.

Figure 45 shows the two types of speckle patterns employed in this study. Both patterns are fundamentally made from misting multi-surface spray paint to produce a random speckle pattern. This is one of several recommended methods from Instron for producing a nominally homogeneous speckle pattern covering the entire sample. Two different patterning techniques were chosen based on the sample surface conditions due to the high contrast nature and optimized red-lighting of the AVE2 extensometer. Per

the instruction manual of the extensometer, light speckle patterns on dark backgrounds are preferred (typically bare metal is considered a dark background due to the imaging conditions of the camera). For samples that have been machined (milled) to final dimensions, a white speckle pattern can be directly applied to the part. The white paint remained as an array of discrete spots without coalescence, provided minimal pain was applied, that was well recognized by the DIC algorithms. An example of a machined surface pattern is shown in the bottom sample of Figure 45. However, in the as-printed condition, the speckle pattern on the top of Figure 45 was used. The high surface roughness resulting from partially melted powder particles adhering to the surface of the tensile bar in the as-printed condition caused the white paint (the speckle pattern) to spread and coalesce if it was applied directly to the bare metal. The solution was to uniformly coat the sample with a black base layer that was solid and thick enough to provide a nominally smooth surface. After the black base coat dried, the white speckling can be applied and it forms discrete dots suitable for DIC.

Figure 45. The two types of speckle patterns used for DIC strain mapping for (top) as-printed samples and (bottom) machined samples.

A.5 Metallographic Preparation

High quality metallographic preparation is the foundation for much of the characterization work in this investigation. Light optical microscopy (LOM), microhardness, X-ray diffraction (XRD), and a number of the advanced electron microscopy techniques all have the prerequisite of a good surface finish for proper analysis. The ASM Specialty Handbooks for particular alloys are excellent tools to assist in optimizing preparation procedures.[16] Ultimately, many individual refinements will likely have to be made from published preparation procedures if the consumable metallographic products are not from the same suppliers.

Copper alloys are relatively soft and during sectioning the size of the affected material must be considered. High speed abrasive cut-off wheels with Bakelite bonded silicon carbide give excellent results with minimal near-surface damage. Coolant should always be used to minimize heat buildup near the cutting surface and avoid any heat induced microstructural changes. Ideally, low force/feed rate should be used to minimize the possibility of embedding abrasive media in the sample. Shearing can be employed for thin samples, however care must be taken in either removing or excluding the large deformed/damaged zone near the sheared interface from analysis.

Samples were mounted in either Bakelite thermosetting epoxy or in cold-setting epoxy resin. Both mounting materials produce satisfactory results. Compression mounting in Bakelite is faster and results in a harder mounting

material which aids somewhat in metallographic preparation, however the process involves pressures up to 4000 psi and temperatures up to 180°C. For the alloys studied in this investigation, and indeed most metal alloys, these conditions do not pose any difficulties. For low temperature alloys or pure metals, care must be taken to avoid recrystallization or other microstructural changes during mounting.[16] Cold-setting epoxy is suitable for thin samples that may be bent during compression mounting. Cold-setting epoxy can also have the added benefit of producing clear mounts and it is moderately easier (although still difficult) to remove samples from the mount. Clear mounts enable accurate determination of the depth and orientation of the viewed cross section. Functionally, assuming the microstructure is not affected by compression mounting, both mounting methods can be used successfully and whichever is readily available may be utilized.

Grinding can be completed manually or automatically. In either case, low pressure should be used, approximately 20-30 N per sample was found to be appropriate for the small cross sections studied in this work. Silicon carbide paper with water lubrication was completed from 320 grit progressively to 600 grit. Porosity in the samples has the potential to store abrasive media that could contaminate polishing cloths or fall out and produce scratches later in the process. If this issue is encountered an intermediate ultrasonic cleaning in ethanol can be employed with the sample place on its side to clean the porosity, but this step was often omitted without repercussions.

Polishing steps must be elongated compared to harder alloys to eliminate sub-surface deformation. The typical times for polishing in this investigation was 2-3 minutes. Polishing on a napped or flat synthetic cloth with 6 μm diamond abrasive after 600 grit paper is a critical step. Even after the visible 600 grit scratches are removed, sub-surface deformation from the 600 grit scratches typically remains. Although this deformation cannot be seen in LOM, it will be readily visible in backscatter electron imaging and electron backscatter diffraction (EBSD). Diamond compound and oxide slurry polishing at 1 μm produce similar satisfactory results. Although oxide polishing can leave some staining on the surface, it is easily removed during the final polishing step and may be ignored. Diamond polishing has higher removal rates and times may be shorts, additionally it is easier to employ on automatic machines and is therefore preferred.

Final polishing should be completed with 0.05 μm colloidal silica on a cloth with a high nap. The high nap gives a better polish around the rounded pore edges. Vibratory final polishing can be employed, but extended times will result in excessive rounding of the porosity in SLM components and should be avoided. The best final polish is achieved by attack polishing (also referred to as chemical mechanical polishing) with an enhanced alkaline colloidal silica mixture. To minimize the amount of etching that occurs during final polishing, the mixture is kept at a low a concentration of 1% ammonium hydroxide, 1% hydrogen peroxide and 98% 0.05 μm colloidal silica. Final attack polishing

should be done for less than 90 seconds to minimize etching, particularly if EBSD is to be performed on the sample where the topography will minimize the quality of the obtained patterns. If short times of attack polishing give insufficient results, longer times in just colloidal silica beforehand can improve the final surface finish.

Typical copper etchants based on ammonium hydroxide and hydrogen peroxide work for SLM copper alloys, although grain boundary contrast tends to be weak. Grain boundary contrast can be improved by lowering the amount of hydrogen peroxide, but alternative etchants give better results when available. Two primary etchants were utilized for LOM observation of both alloys studied in this research. The first etchant, a tint etchant known as Klemm's I, gives excellent chemical contrast and moderate grain contrast in cross-polarized light. Klemm's I is composed of 50 ml saturated aqueous sodium thiosulfate and 1 g potassium metabisulfate Figure 46 shows a comparison of the bright field and cross-polarized contrast developed by Klemm's I for SLM C70250 (etching behavior was similar for both alloys studied). The bright field image shows the change in substructure scale near the weld line particularly well, but grain contrast is faint. Cross-polarized observation enhances grain contrast based on orientation differences. Klemm's I gives good results for characterization, however there are some practical difficulties with its use. Klemm's I cannot be stored and must be made fresh every time it is to be used. Additionally, tint etchants function by

forming a film on the surface of the alloy. Regions with different potential etch at different rates, producing contrast. Potential differences arise from grain orientation differences, grain boundaries, different phases, and chemical gradients in a single phase. Since tint etchant contrast relies on film formation and growth on the surface, the etchants are fairly time sensitive and typically must be re-polished between attempts.[104] Different etching times can produce different amounts of contrast in SLM copper alloys, which can make it difficult to have consistent image contrast for comparison across various sample conditions, particularly when chemical segregation or grain morphology is changing. Etching should be conducted via immersion and the sample should not be moved for the duration. Observations should be done immediately, as the surface will change slightly if left in open air.

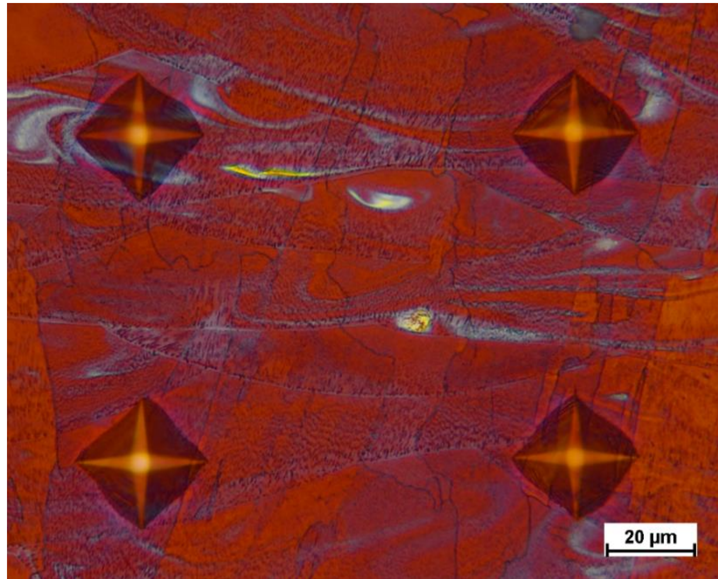

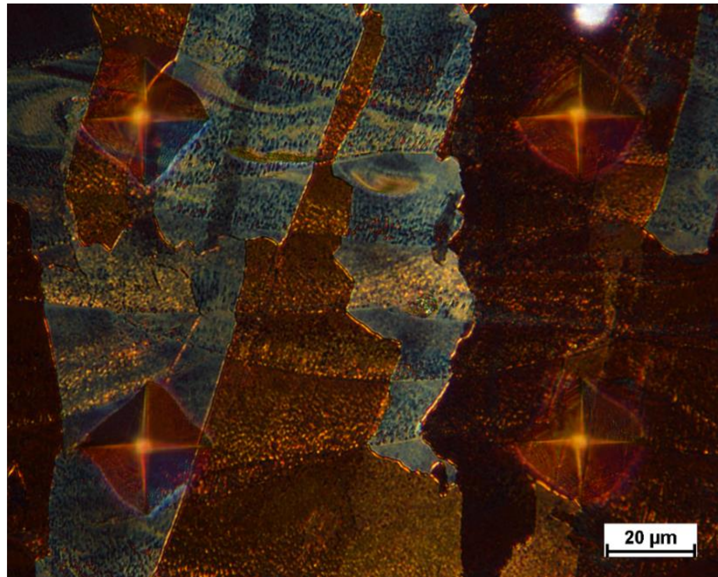

Figure 46. Comparison of LOM contrast after etching with Klemm's I for 2 minutes 15 seconds in (top) bright field and (bottom) cross-polarized light. Alloy C70250, build direction, as-printed condition.

The second etchant utilized in this experiment was a 5 g ferric nitrate, 25 ml hydrochloric acid and 70ml water solution. This solution is far more sensitive at producing contrast from potential differences across grain boundaries and twin boundaries. Figure 47 shows an LOM micrograph of the

contrast obtained from etching with the ferric nitrate solution. The microstructure is quite busy because of the excessive twinning and large amount of grain boundaries. Regardless, contrast of the twins and grain boundaries is superior and more consistent compared with etching in Klemm's I reagent. The ferric nitrate solution is a traditional chemical etchant where the reaction products are dissolved into the etchant. Some reaction products can be left on the surface after simple immersion, so swabbing with cotton soaked in the etchant is recommended to produce a more even etch across the sample surface.

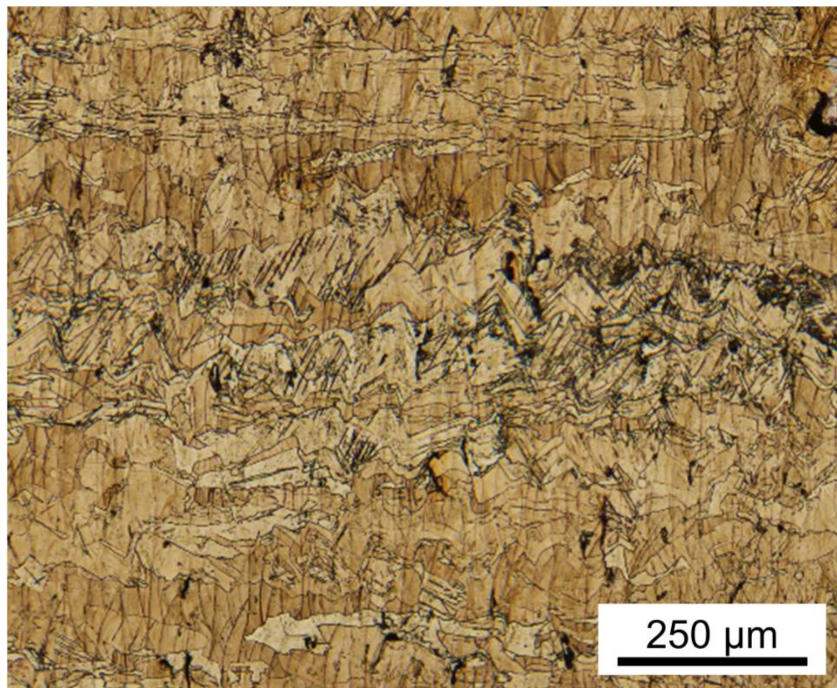

Figure 47. LOM micrograph of contrast after etching with ferric nitrate solution. Alloy C70250, peak age, strained to failure to show twinning.

A.6 Microhardness

Microhardness on SLM samples can generally be conducted using standard methodology per the ASTM E-384 16 standard.[103] This is typically done on metallographic samples that have been final polished, but samples that have also been etched may be used if identification of particular microstructural areas of interest is required. There is no significant effect of load choice within standard values, as shown by experimental measurements in Figure 48. At particularly low loads (e.g. 25 g) the deviation of the results becomes significantly larger. Low loads may be necessary to decrease indent size for quantification of small microstructural features, but they should be avoided where possible. Care should also be taken if automatic imaging and measurement systems are used. Due to the porosity present in SLM samples, a random grid of microhardness indents will typically lead to several indents landing on the exposed porosity. These measurements should be excluded from statistical analysis, as the intention of the microhardness measurements is to characterize the bulk metal, not the porosity which is addressed during density measurement. In this investigation, a spatial analysis of 100 hardness measurements on both the build cross section and the transverse cross section did not reveal any consistent changes in hardness based on measurement location.

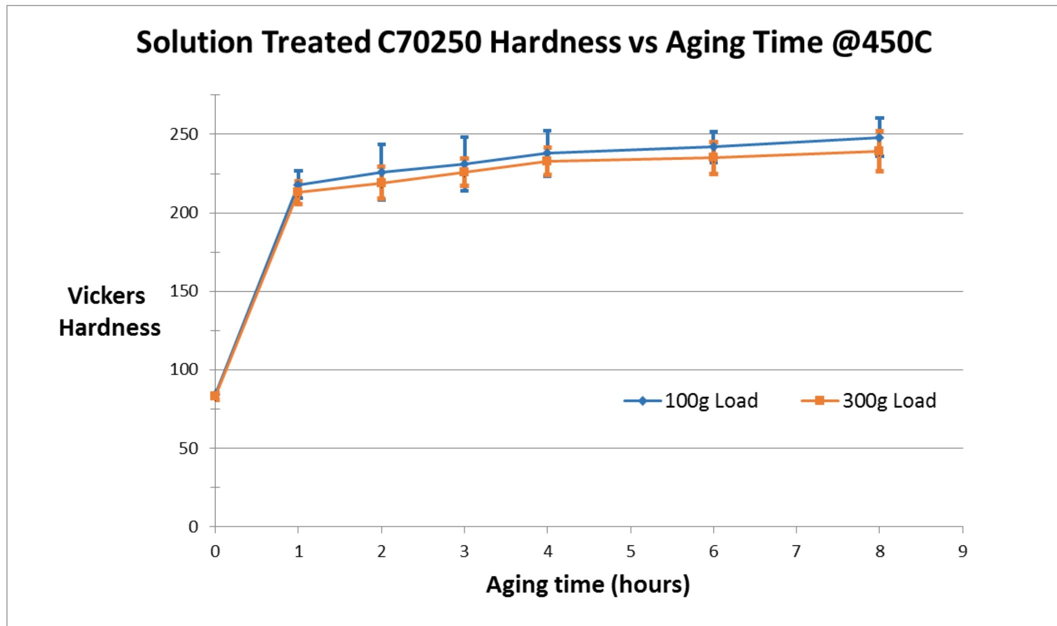

Figure 48. Comparison of microhardness measurements taken with different indentation loads. Alloy C70250, solution treated and aged.

A.7 Standard Operating Procedure for Phase ID by XRD

In general, standard practices for x-ray diffraction (XRD) was used in this investigation. No particularly unique preparation or collection steps were developed to obtain diffraction data to aid in phase identification via peak indexing. Individual operation will vary based on available facilities. However, the standard operating procedure developed for use in this investigation for the Empyrean XRD unit and software available at Lehigh University at the time of this investigation is presented here.

Applications:

- Identification of primary and secondary phases in metal alloys (confirmed to work on ~50 nm particles) including impurity particles

- May be able to detect strengthening precipitates, however in many alloys in the peak age condition they are too small to reliable get peaks

Sample Preparation: Sample surface should be polished to at least 1 μm. Thin samples are ideal and the two surfaces (polished and unpolished) should be as parallel as possible. The sample should ideally not be in a mount to reduce background; it must either be polished by hand or removed from an epoxy mount after polishing.

X-Ray Optics Setup: The Bragg-Brentano prefix module (BBHD) is used in this procedure. Attach the BBHD and use the files in the training folder on the desktop to select appropriate incident beam inserts (divergence slit, mask, etc.) and accompanying diffracted beam optics for your sample geometry. The Fixed Anti-Scatter Slit (FASS) adapter is used with the Pixcel detector for this procedure.

Alignment: Place your sample in the center of the stage, long axis aligned with the beam direction. Open Data Collector and complete the initializing and alignment steps:

- When opening and closing the doors, be sure they are firmly shut to avoid a door lock error
- Instrument -> Connect -> Chi-Phi-Z
- If prompted, select No when asked if you would like to use the previous offsets

- Double click the instrument panel and set the operating Tension to 45 and the current to 40
- Set the incident and diffracted beam optics to match what you installed for your sample geometry
- Install the Cu-Ni attenuator mask for alignment
- Measure->Manual Scan
- Scan 2θ (Range 4, Step .01, time .1). When scan is complete, right click->move mode and move the line to the maximum
- Double click the control pane and rough the Z position so your sample is roughly in line with the beam
- Scan Z (Range 5, Step .01, time .1) move the line to 50% of the maximum intensity. If there is no drop in intensity in the scan range, expand the range or change the Z value to find your sample
- Scan Ω (Range 5, Step .01, time .1) move the line to the maximum
- Repeat Z scan
- User Settings -> Fine Calibration Offsets -> Set New=0
- Remove the Cu-Ni mask and install the appropriate size for your geometry

Program: Your program setup will largely depend on the peaks you are looking for, but a good place to start is a single Gonio scan (θ-θ) from 20-100 degrees with a step of around .02 and a time per step that gives a reasonable

scan time for your intended use. If texture is an issue, Phi can be wobbled during a repetitive scan.

Shutdown: Change the instrument settings back to a tension of 45 and a current of 20, disconnect from the machine, and turn off the light inside the unit.

A.8 Electron Backscatter Diffraction

Electron backscatter diffraction (EBSD) was primarily used in this investigation to characterize grain orientation. Poor surface conditions or improper grounding in the SEM can affect interpretation of results. Figure 49 shows some of the common defects that can occur during an EBSD scan due to poor surface preparation. Overlaying the image quality in greyscale can assist in checking for defects. Scratches will only appear as poorly indexed patterns in an IPF map, but their morphology is easily distinguished when viewing the image quality. Similarly, the fiduciary hardness indents are easily observed. Scratches typically result from insufficient polishing time in the 6 μm to final polishing range or contamination being released from pores during final polishing steps. If the sample is not properly grounded, drifting can occur which is also seen as streaking in Figure 49. This can be avoided by coating the surface of the sample per standard SEM techniques (e.g. Ir, Au-Pd), however the coating should be kept as thin as possible because it obscures observation of the EBSD patterns.

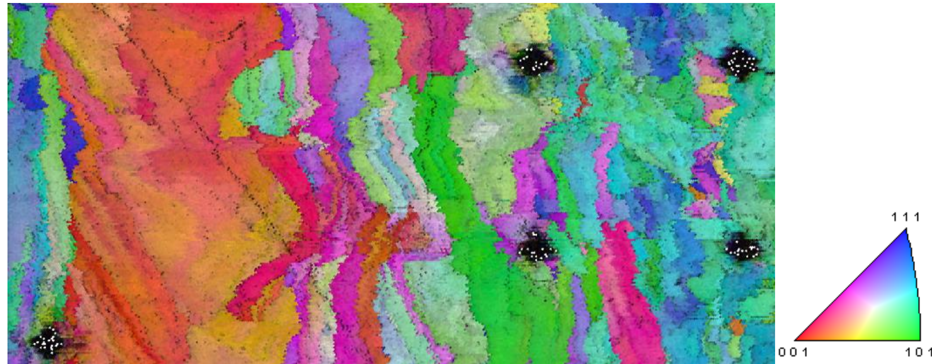

Figure 49. IPF map obtained from EBSD showing scratches and drifting. Image quality is overlaid in greyscale. Alloy C70250, as-printed.

Most defects may be filtered out of the data in the processing software, but care must be taken to avoid changing an excessive amount of data. Grain dilation is a simple technique that handles most common indexing issues well, and provided the percentage of points altered was below 10% of the total data, interpretation of results was not adversely affected. Attack polishing should be minimized if EBSD is to be performed on copper alloys, as the etching effect will decrease the quality of patterns and affect data collection. Additionally, vibratory final polishing should be avoided so ensure metallographic rounding around porosity is kept to a minimum.

EBSD was successfully conducted for SLM copper alloys at accelerating voltages from 15-20 kV with the largest aperture and a low condenser lens setting (larger spot size). Step size varies based on the features being observed, but larger step sizes allow for larger scans which can give better statistics for orientation investigations. Care must be taken to avoid "hiding" smaller features (for example sharp deformation twins) by using a step size that is too small to fully resolve the feature. Regardless, bulk

texture/preferred orientation is ideally studied by XRD and EBSD is more appropriately suited to analyzing micro-texture for example growth directions within a weld pool. Camera binning should be as high as possible to facilitate faster data collection. In the as-printed conditions, SLM copper alloys had a fair amount of lattice strain (see Chapter 3) and as a result binning had to be decreased to improve pattern quality and indexing. For ease of analysis, important sample axes (e.g. the build direction and scanning directions in SLM components) should be oriented orthogonally to the microscope axes. The data can be mathematically rotated, but many of the automatic software analyses techniques are simplified if the axes are more simply related.

A.9 Focused Ion Beam Milling and TEM Sample Preparation

Focused Ion Beam (FIB) milling is a technique that can produce high quality transmission electron microscopy (TEM) samples. The procedure involves a Ga ion beam to mill out sloped trenches on either side of a thin strip of the bulk material. The strip is then attached to a plucker needle by depositing a small layer of platinum before the strip is cut away from the bulk using to ion beam. The strip (or lamella) can then be attached to a TEM grid and sequentially thinned further until it is electron transparent, roughly less than 100 nm thick. Molybdenum grids were used in this investigation in contrast to more common copper grids to facilitate x-ray (EDS/EDAX) analysis.

Generally, copper can be ion milled with minimal difficulty. Copper readily redeposits, but this issue is easily dealt with by milling larger trenches and cutaways during sample fabrication. However, copper can be damaged during focused ion beam milling which creates artifacts that can obscure TEM observation. Figure 50 shows examples of FIB damage in pure copper which was found to vary with milling parameters. The damage is a combination of Ga containing amorphous zones and surface roughening that has been observed during Ga ion milling of other materials. Additionally, observation of the defects changes with diffraction conditions. The amount of damage depends primarily on the ion energy, milling current and incident angle (all of which should be reduced to minimize damage).[105]

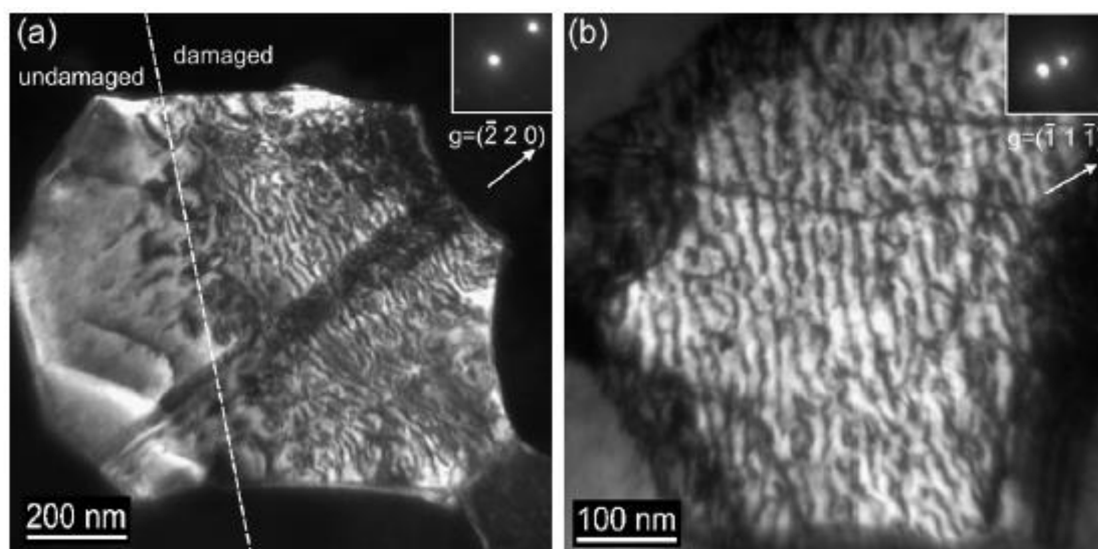

Figure 50. Examples of FIB damage observed during Ga ion milling of copper. Damaged regions were exposed to (a) 30 keV 50 pA Ga ions and (b) 5keV 100 pA Ga ions.[105]

The extent and amount of damage can be reduced by less aggressive milling parameters, but nano-milling with Ar atoms after ion milling can also improve the sample surface finish and minimize observation of damage.[106] Figure 51 shows an example TEM micrograph of FIB damage observed in this investigation. The morphology is similar to the damage observed in literature, and the milling conditions for this sample were consistent with those that produced the damage shown in Figure 50. Care must be taken when fabricating and observing samples to avoid interpreting damage as microstructural features. In this investigation, damage was significantly reduced and no longer observed after extensive low energy broad beam thinning during Ga milling and extended (~5 minutes per side of TEM sample at 900eV, 110 pA beam) nano-milling with low energy Ar atoms.

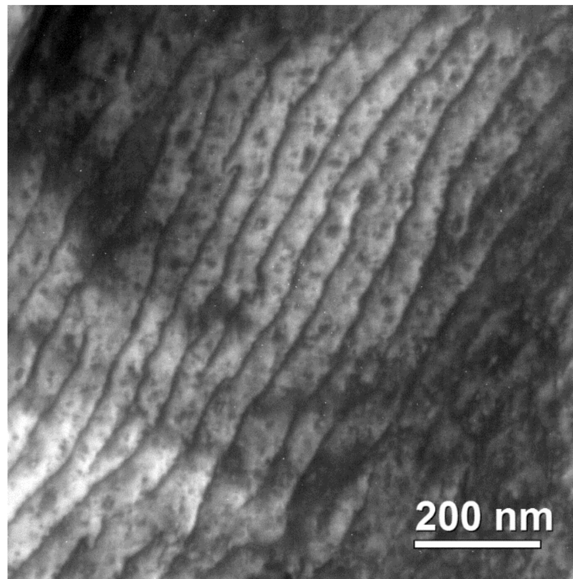

Figure 51. Example TEM micrograph showing FIB damage observed in this research. Alloy C70250, over aged.

A.10 Transmission Electron Microscopy

After the samples produced by FIB were nano-milled, they were placed in a double-tilt holder for TEM/STEM observation at 200kV. A double-tilt holder was necessary to tilt to different zone axes to achieve two-beam conditions for dislocation observation as well as to observe the precipitates in alloy C70250. Liquid nitrogen was added to the cold finger 30 minutes prior to operation, and standard alignment procedures were conducted before any image collection. Bright-field (BF), dark-field (DF) and selected area diffraction patterns (SADP) were collected on a calibrated camera and analyzed using Gatan Microscopy Suite 3. The imaging conditions are reported independently in the result and discussion sections in Chapter 3 and Chapter 4. Since the expected phases were established from literature, diffraction patterns were indexed by a combination of direct measurement of SAD patterns and comparison to simulations and literature. The angle between diffraction spots and the pattern spacing was compared to reference patterns simulated by JEMS-SAAS.[69, 93] The specific details of analysis of the precipitates and compositional variations in alloy C70250 are described in Chapter 4 as they are relevant to interpretation of the results.

VITA

Anthony Patrick Ventura was born on September 29, 1989 in Columbia, MD to Chris and Dale Ventura. He grew up in Ellicott City, MD with his older brother Dominic and graduated from Centennial High School in 2007. He obtained his B.S. in materials science & engineering at Lehigh University in 2011. Anthony stayed at Lehigh University and began his graduate studies under the guidance of Dr. Wojciech Misiolek and Dr. Sabrina Jedlicka. After two years, he earned his M.S. in materials science and engineering from his investigation of Anodic Aluminum Oxide (AAO) Membranes for Cellular Devices. Once again, he remained at Lehigh and then became a PhD candidate under Dr. Misiolek. For his doctoral degree, he studied the physical metallurgy of selective laser melted copper alloys and graduated in May 2017. After graduation, Anthony will be working as an engineer at Pratt & Whitney in East Hartford, CT performing research and development.